Angular Resolved low loss EELS
for Materials Characterization

THÈSE N^{O} 5965 (2013)

PRÉSENTÉE LE 20 DÉCEMBRE 2013
À LA FACULTÉ DES SCIENCES DE BASE
LABORATOIRE DE SPECTROMÉTRIE ET MICROSCOPIE ÉLECTRONIQUE
PROGRAMME DOCTORAL EN PHYSIQUE

ÉCOLE POLYTECHNIQUE FÉDÉRALE DE LAUSANNE

POUR L'OBTENTION DU GRADE DE DOCTEUR ÈS SCIENCES

PAR

Simon SCHNEIDER

acceptée sur proposition du jury:

Prof. M. Q. Tran, président du jury
Prof. C. Hébert, directrice de thèse
Dr R. Erni, rapporteur
Dr J.-D. Ganière, rapporteur
Dr G. Hug, rapporteur

ÉCOLE POLYTECHNIQUE
FÉDÉRALE DE LAUSANNE

Suisse
2013

Remerciements

Avant tout, je tiens à remercier ma directrice de thèse, Prof. Cécile Hébert. Elle m'a guidé à travers cinq années de travail intensif aboutissant sur ce manuscrit. Il est très agréable de travailler avec une personne qui met les relations humaines en avant. En effet, dès le premier jour, l'ambience de travail était très agréable. Bien que très occupée et souvent en voyages, Cécile prenait le temps d'analyser avec moi les problèmes qui survenaient durant mes recherches et m'aidait à trouver des solutions.

Je remercie également les membres de mon jury, Prof. Minh Quang Tran du CRPP, Dr Jean-Daniel Ganière de l'ICMP, Dr Rolf Erni de l'EMPA et Dr Gilles Hug d'ONERA pour leurs commentaires et propositions d'améliorations.

Un remerciement particulier aux personnes du CIME m'ayant étroitement accompagné durant ce travail, à savoir :

- Prof. Pierre Stadelmann pour les discussions que nous avons eues et le partage de son immense savoir sur la microscopie électronique et le programme informatique Mathematica©, ainsi que ses conseils pratiques et son soutien moral ;
- Dr Duncan Alexander pour les heures passées à mes côtés à résoudre des problèmes techniques au JEOL, les analyses de résultats obtenus, ainsi que toutes les discussions fructueuses que nous avons eues ;
- Dr Aïcha Hessler et Dr Barbora Bartova pour m'avoir initié à l'utilisation d'un microscope électronique à transmission ;
- Dr Audrius Alkauskas pour l'étroite collaboration que nous avons partagée, les explications sur l'aspect théorique de ce travail et les calculs effectués sur mes données d'argent ;
- Dr Guillaume Lucas pour son soutien lors du codage avec Digital Micrograph™ ;
- Danièle Laub et Colette Vallotton pour leurs conseils et aide concernant la préparation d'échantillons ;
- Grégoire Baroz pour le soutien informatique ;

- Annick Evéquoz, Isabelle Moinon, Chantal Roulin et Anh Eymann pour tout le travail administratif qu'elles ont effectué avec une minutie remarquable.

Un grand merci à tous les autres membres du CIME que j'ai côtoyés durant ma thèse : Dr Pierre Burdet, Dr Marco Cantoni, Dr Davide Demurtas, Dr Antonin Faes, Dr Florent Ravaux, Dr Andreas Schuler, Dr Jonas Vannod, Brian Aebersold, Amélie Bazzoni, Fabienne Bobard, Caroline Calderone, Quentin Jeangros, Emad Oveisi, Guillaume Pasche.

Un remerciement à Nachiappan "Nachi" Chidambaram du Laboratoire des Céramiques pour la préparation d'échantillons d'argent par projection sous vide.

Je voudrais également remercier les personnes suivantes, qui m'ont permis de trouver un judicieux équilibre entre le travail scientifique et un relâchement total lors d'efforts physiques ou d'autres activités récréatives :

- Tous les gens du Judo Ju-Jitsu Club Savigny et très spécialement Laurent Delessert qui m'a servi de Uke lors de mon passage de 1^er^ Dan Judo. Désolé pour toutes les frappes, clés et étranglements mal contrôlés que tu as dû subir à cet effet...
- Les membres du comité de la section Tir de la Société Vaudoise des Officiers.
- Mes frères et sœurs de couleur de la société d'étudiants Valdésia.
  Vivat, crescat, floreat in æternum !

Enfin, je ne saurais comment remercier mon épouse Olivia et ses enfants Marie-Noël et Jean-Etienne, ainsi que mes parents Roland et Anne-Catherine qui m'ont soutenu moralement durant cette longue épreuve. Mon infinie et profonde reconnaissance leur est due.

Lausanne, December 6, 2013 Simon D. Schneider

Abstract

Electron Energy Loss Spectrometry (EELS) in Transmission Electron Microscopy (TEM) is a powerful tool for the investigation of the electronic structure of materials. In the low loss regime, one can access the optical properties which are governed by the dielectric function $\varepsilon(\omega)$, which may be retrieved thanks to the so-called "loss function". The energy range covered by EELS goes from the infrared (less than 1 eV) to the hard X-rays (about 3 keV), each region having its own interest. The low loss region (0–100 eV) serves to investigate the valence electron structure and the inter-band transition behavior. Using angular resolved EELS gives further information about the dispersion behavior of the investigated material.

This work is a part of a large project aiming a closer agreement between theory and experiment in angular resolved EELS by improving the state of the art in both fields. The purpose of this work is to set up a reliable experimental technique to retrieve the momentum transfer resolved single scattering distribution at very low energy with good accuracy and resolutions. One of the main challenges was to use the newly installed JEOL 2200 FS transmission electron microscope that is equipped with an in-column Ω filter for retrieval of the loss function in diffraction energy filtered TEM.

Issues such as the angular resolution, contamination, image-coupling in diffraction mode and plural scattering have been solved. Several optical alignments and operational modes of the JEOL 2200 FS have been tested, and finally nano-beam diffraction was found to be the optimal running mode. This work provides for the first time a full 3D energy loss data cube in diffraction mode with energy and angular resolutions of 1 eV and 0.5 nm^{-1} respectively. After processing, the energy and angular relevant data span an energy loss range from 2.75 eV to 40.25 eV and the angular momentum transfer up to 12.5 nm^{-1}. Although theoretically, without CCD camera binning and the maximum available camera length of the JEOL (250 cm), a momentum transfer resolution of 0.04 nm^{-1} would have been possible, the effective angular resolution was limited by the smallest obtainable beam convergence as well as by the remaining aberrations of the microscope.

The presented technique can be reproduced on any transmission electron microscope equipped with an in-column energy filter. Furthermore, it is demonstrated that the proposed method provides working ranges in energy, spatial and angular resolutions limited only by the performance of the microscope. Previous techniques did not provide experimental results showing an energy resolution independent of the spatial and angular resolutions.

Keywords: electron energy loss spectrometry (EELS), momentum-dependence, inelastic scattering, diffraction, nano-beam, energy filtered transmission electron microscopy (EFTEM), dielectric function.

Résumé

La spectrométrie de perte d'énergie des électrons (acronyme anglais EELS) en Microscopie Electronique en Transmission (MET) est un puissant outil pour analyser la structure électronique des matériaux. Dans le régime des faibles pertes, il est possible d'accéder aux propriétés optiques qui sont régies par la fonction diélectrique $\varepsilon(\omega)$, cette dernière pouvant être retrouvée grâce à la fonction de perte d'énergie (loss function). La plage d'énergies couverte par l'EELS va de l'infrarouge (moins de 1 eV) aux rayons X lointains (environ 3 keV), chaque région ayant son propre intérêt. La région des faibles pertes (0–100 eV) sert à étudier la structure des électrons de valence et le comportement des transitions inter-bandes. Employer l'EELS résolu en angle permet d'obtenir des informations supplémentaires sur le comportement dispersif du matériau analysé.

Ce travail fait partie d'un projet plus vaste ayant pour but d'améliorer la concordance entre théorie et expérimentation en EELS résolu en angle en améliorant l'état actuel dans les deux domaines. Le but de ce travail est d'établir une méthode expérimentale sûre pour retrouver la diffusion simple résolue en transfert de quantité de mouvements et la fonction diélectrique à très basse énergie, avec une bonne précision et une bonne résolution. Un défi majeur était d'utiliser le microscope électronique à transmission JEOL 2200 FS nouvellement installé, équipé d'un filtre Ω dans la colonne pour retrouver la fonction des pertes en mode diffraction filtrée en énergie.

Plusieurs problèmes tels que la résolution angulaire, la contamination, le couplage image-diffraction et les pertes multiples ont été résolus. Plusieurs alignements optiques et modes de fonctionnement du JEOL 2200 FS ont été testés, pour finalement déterminer que la diffraction en illumination nano-beam est le mode opératoire optimal. Ce travail fournit pour la première fois un ensemble de données 3D complet de pertes d'énergies en mode diffraction avec des résolutions respectivement de 1 eV en énergie et de 0.5 nm^{-1} en angle. Après le traitement, les données pertinentes s'étendent sur une plage d'énergies de 2.75 eV à 40.25 eV et un transfert de quantité de mouvement jusqu'à 12.5 nm^{-1}. Si théoriquement, sans binning de la CCD et avec la longueur de caméra maximale du JEOL (250 cm), une résolution angulaire de 0.04 nm^{-1} pourrait être atteinte, cette dernière a été limitée par la plus faible convergence angulaire que l'on peut obtenir, ainsi que par les aberrations restantes du microscope.

La technique présentée peut être reproduite sur n'importe quel microscope électronique à transmission équipée d'un filtre dans la colonne. De plus, il est démontré que la méthode proposée permet des résolutions en énergie, angulaires et spatiales ne dépendant que des capacités du microscope, contrairement aux techniques précédemment proposées.

Mots-clé : spectrométrie de perte d’énergie en angle (EELS), dépendance de la quantité de mouvement transmise, diffusion inélastique, diffraction, nano-beam, microscopie électronique en transmission filtrée en énergie (EFTEM), fonction diélectrique.

Zusammenfassung

Elektronenenergieverlustspektrometrie (englisches Akronym EELS) in Transmissionselektronenmikroskopie (TEM) ist ein kraftvolles Werkzeug um die elektronische Struktur von Materien zu untersuchen. Im geringen Verlustbereich kann man auf die optischen Eigenschaften zugreifen, welche von der Dielektrizitätsfunktion $\varepsilon(\omega)$ bestimmt werden, jene durch die sogenannte Verlustfunktion ausfindig gemacht werden kann. Der durch EELS abgedeckte Energiebereich geht vom Infrarot (weniger als 1 eV Verlust) bis zu den harten Röntgenstrahlen (circa 3 keV), jede Region ihr eigenes Interessen besitzend. Die geringe Verlustregion (0–100 eV) dient zur Untersuchung der Valenzelektronenstruktur und des Interbandübergangverhaltens. Die Verwändung von winkelaufgelöstem EELS ergibt zusätzliche Information über das Streuverhalten des untersuchten Materials.

Diese Arbeit ist Teil eines breiten Projekts, dessen Ziel es ist, die Übereinstimmung zwischen Theorie und Experiment in winkelaufgelöstem EELS zu nähern, indem der Stand der Technik in beiden Bereichen verbessert wird. Das Ziel dieser Arbeit ist eine sichere experimentale Methode zu erstellen, welche es erlaubt, die impulsübertragungsaufgelöste Einzelstreuverteilung und die Dielektrizitätsfunktion im tiefen Energievelustbereich mit guter Präzision sowie guter Auflösungen wiederzuerlangen. Eine der wichtigsten Herausforderungen war es, das neu installierte, mit einem in der Kolonne integriertem Ω Filter ausgestatteten Transmissionselektronenmikroskop JEOL 2200 FS zu gebrauchen, um die Verlustfunktion in energiegefilterter Beugung zu erarbeiten.

Verschiedene Probleme wie Winkelauflösung, Kontamination, Bild-Kopplung im Beugungssmodus sowie Mehrfachstreuung sing gelöst worden. Mehrere optische Anordnungen und Betriebsarten des JEOL 2200 FS wurden getestet, um schliesslich Beugung mit Nanobeambeleuchtung als optimaler Betriebsmodus zu bestimmen. Diese Arbeit erzeugt zum ersten Mal einen vollständigen 3D-Energieverlustdatensatz in Beugungsmodus mit Energie- und Winkelauflösung von 1 eV bzw. 0.5 nm^{-1}. Nach der Datenverarbeitung umfassen die energie- und winkelrelevanten Daten einen Energieverlustbereich von 2.75 eV bis 40.25 eV und eine Impulsübertragung bis zu 12.5 nm^{-1}. Obwohl theoretisch ohne Binning der CCD-Kamera und der maximal verfügbaren Kameralänge des JEOL (250 cm) eine Impulsübertragungsauflösung von 0.04 nm^{-1} möglich wäre, wurde die effektive Winkelauflösung durch die kleinste erhältliche Strahlkonvergenz sowie durch die verbleibenden Aberrationen des Mikroskops begrenzt.

Das vorgestellte Verfahren kann auf jedem mit einem in der Kolonne integrierten Filter ausgestattetem Transmissionselektronenmikroskop wiedergeben werden. Weiterhin wird gezeigt, dass das vorgeschlagene Verfahren Arbeitsbereiche in Energie-, Raum- und Winkelauflösung ermöglicht, die nur durch die Leistung des Mikroskops begrenzt sind. Früher angewendete Verfahren haben keine experimentellen Ergebnisse gezeigt, die eine von den Raum- und Winkelauflösungen unabhängige Energieauflösung zeigt.

Schlüsselwörter: Elektronenenergieverlustspektrometrie (EELS), Impulsabhängigkeit, inelastische Streuung, Nano-beam, energiegefilterte Transmissionselektronenmikroskopie (EFTEM), Dielektrizitätsfunktion.

Contents

List of acronyms

AREELS	Angular Resolved Electron Energy Loss Spectrometry
BFP	Back Focal Plane
BZ	Brillouin Zone
CCD	Charge Coupled Device
CIME	Centre Interdisciplinaire de Microscopie Electronique
CL	Camera Length
CL	Condenser Lens
CLA	Condenser Lens Aperture
CM	Condenser Mini lens
CMOS	Complementary Metal–Oxide Semiconductor
CPU	Central Processing Unit
DC	Direct Current
DM	DigitalMicrograph™
DOS	Density Of States
DQE	Detection Quantum Efficiency
EDM	Electrical Discharge Machining
ELNES	Energy Loss Near Edge Structures
EELS	Electron Energy Loss Spectrometry
EFTEM	Energy Filtered Transmission Electron Microscopy
EFNBED	Energy Filtered Nano-Beam Electron Diffraction
ENTA	ENTrance Aperture
EP	ElectroPolishing
EPFL	Ecole Polytechnique Fédérale de Lausanne
fcc	Face Centered Cubic
FEG	Field Emission Gun
FFT	Fast Fourier Transform
FIB	Focused Ion Beam
FL	Filter Lens
FWHM	Full Width at Half Maximum
GGA	Generalized Gradient Approximation
GIF	Gatan Imaging Filter

continuation on next page

HAD	Hollow Anode Discharge
HCA	High Contrast Aperture
HT	High Tension
IBT	Ion Beam Thinning
IL	Intermediate Lens
IP	Imaging Plate
JEM	JEOL Electron Microscope
JEOL	Japan Electron Optics Laboratory Ldt.
KKA	Kramers-Kronig Analysis
LFE	Local Field Effects
LSME	Laboratoire de Spectrométrie et Microscopie Electronique
MANDOLINE	Magnetic Aberration-free Noticeably Dispersive Omega-Like INhomogeneous Energy
NBD	Nano-Beam Diffraction
OL	Objective Lens
OLA	Objective Lens Aperture
OM	Objective Mini lens
PCA	Principal Component Analysis
PEELS	Parallel Electron Energy Loss Spectrometer
PIPS	Precision Ion Polishing System™
PL	Projector Lens
q-EELS	angular resolved EELS
REELS	Reflection EELS
RPA	Random Phase Approximation
SAA	Selecting Area Aperture
SAED	Selected Area Electron Diffraction
SCCM	Standard Cubic Centimeter per Minute
SEM	Scanning Electron Microscope
SESAM	Sub-Electron-volt-Sub-Angstrom Microscope
SMT	Semiconductor Manufacturing Technology
STEM	Scanning Transmission Electron Microscopy
TDDFT	Time Dependent Density Functional Theory
TEM	Transmission Electron Microscopy or Microscope
VG	Vacuum Generators
ZL	Zero Loss
ZLP	Zero Loss Peak

List of symbols

Greek symbols

α	convergence angle of the incident beam
β	semi-angle of collection
ΔE	energy loss
δE	energy selecting slit width
$\varepsilon(\omega)$	complex dielectric function
$\boldsymbol{\varepsilon}(\omega, \boldsymbol{q})$	complex dielectric tensor
$\varepsilon_1(\omega)$	real part of the complex dielectric function
$\varepsilon_2(\omega)$	imaginary part of the complex dielectric function
θ	scattering angle
θ_B	Bragg scattering angle
θ_E	characteristic angle
λ	wavelength
σ	cross section
χ	density response function
Ω	solid angle
ω	excitation frequency

Latin symbols

C_s	spherical aberration coefficient
d	distance
d_{hkl}	distance between lattice planes (hkl)
E	energy
E_0	nominal electron beam energy
e^-	electron
FL	Filter lens energy shift
$\boldsymbol{G}$	reciprocal lattice vector
I	intensity
$\boldsymbol{k}$, $\boldsymbol{k}'$	wave vector
k	wave number
n_a	number of atoms per unit volume
P	probability
$\boldsymbol{q}$, q	angular momentum transfer
v	absolute velocity of an electron
x, y, z	cartesian coordinates

Other symbols

(hkl)	lattice plane (Miller indices)
hkl	diffraction spot (Miller indices)
$[UVW]$	zone axis (Miller indices)
$\Im(z)$	imaginary part of the complex number z
d	derivative
∂	partial derivative
$\propto$	proportional to
$\neq$	not equal
$\approx$	approximatively equal
$\varnothing$	diameter

1 Introduction

Electron Energy Loss Spectrometry (EELS) analyses the energy lost by transmitted electrons when they interact with a specimen. It is a powerful method for characterizing optical and electromagnetic properties of materials [1]. The dielectric tensor $\boldsymbol{\varepsilon}$, which can be determined experimentally with the loss function $\Im\left(-1/\boldsymbol{\varepsilon}(\omega, \boldsymbol{q})\right)$ allows access to these properties. EELS measures energy losses ranging from the infrared (less than 1 eV) to the hard X-ray (2–3000 eV) regions, each loss region having its own interest [2]. Contrary to optical absorption spectrometry, EELS can measure energy losses with a finite momentum transfer $\boldsymbol{q} \neq \boldsymbol{0}$, thus giving access to an additional dimension of the loss function. This is interesting, since it allows the investigation of the dispersive behavior of materials.

1.1 Historical development of EELS

The first electron energy loss spectrum experiment with a transmission electron microscope was performed in 1941 by Ruthemann [3]. He noticed and confirmed in 1942 that the structure in the spectrum corresponds to the binding energies of the shell electrons to their nucleus [4]. From then on, it was clear that EELS in Transmission Electron Microscopy (TEM) was a strong method for chemical analysis of thin specimens, thus worth being investigated and developed. The first EELS detection device was developed by Hillier and Baker in 1944 [5]. The very first experimental results dealing with angular resolved EELS could be the optical properties of Ag and Cu in 1962 [6] and, with a transmission electron microscope, the dispersion of surface plasmons of Al and Mg by Kloss and Raether in 1973 [7]. Later, other groups contributed to developing the method [8–10].

Immediately after the development of the first transmission electron microscope by Ernst Ruska in 1931 [11], it was remarked that due to the chromatic aberration of the lenses, the inelastically scattered electrons were blurring the image or diffraction pattern. To alleviate this problem, Boersch designed in 1953 the first energy filter blocking all inelastically scattered electrons having suffered an energy loss larger than 4 eV (Boersch called it "highpass filter" since electrons with high energy are allowed) [12]. This filter was improved by Beaufils in

1959 [13]. At the same time, Hennequin expanded the idea of filtering electrons by proposing a bandpass filter, aimed not to improve the image quality, but to perform chemical analysis (Diplôme d'études supérieures, Paris, 1960). Such a filter was realized by Watanabe and Uyeda [14], using a Möllenstedt biprism (an electrostatic lens used for electron holography). This system suffered from several optical drawbacks (small field of view, astigmatism, chromatic aberration and the necessity to move the intermediate and the final image simultaneously to analyze a large energy loss range). In 1962, Castaing and Henry proposed a new solution to observe the energy loss spectrum of electrons using the dispersive properties of a magnetic prism, the famous Castaing-Henry filter [15].

The popularity of the Castaing-Henry filter increased rapidly after its implementation in a commercial TEM (Zeiss 902) in 1974 and boosted the design of different spectrometers and imaging filters, as well as several techniques like energy filtered imaging [16] or energy filtered diffraction [17]. In 1988, Reimer, Fromm and Rennekamp gave a complete description of the possibilities offered by a Castaing-Henry filter, mentioning EELS and angular resolved EELS in image and diffraction mode [18]. Reimer and Rennekamp also explained how to analyse the angular resolved EELS map (also called Bethe surface) [19]. In order to select a given energy loss range, they used a homemade slit formed by a quartz fiber and evaporated copper inserted after the Back Focal Plane (BFP) of the first projector lens, before the filter entrance. Using this setting, they reached a dispersion resolution of 0.1 mm/eV in the 0–500 eV energy range and an energy filtering resolution of about 1 eV, allowing them to experimentally verify the plasmon dispersion relation. They did not apply this development to high energy resolution and analysis in the very low loss region. In parallel, Batson and Silcox presented the most widely used technique for plural scattering removal in angular resolved data [20]. In these years, not only the low loss region was investigated, but also some works were done in the core loss region, *e.g.* by Leapman investigating the anisotropy of graphite [21].

In 1987, Schattschneider *et al.* proposed an original method for plural scattering removal in angular resolved EELS spectra [22]. However, this method was based on Bessel functions, and was thus extremely CPU-time-consuming and therefore inappropriate for routine analysis at this time. In 1992, Su and Schattschneider proposed a new fast deconvolution method based on a combination of Fourier and discrete Hankel transforms. However, this method was only practical for deconvolving spectra of amorphous or polycrystalline specimen, as they had to abandon one axis of angular information for the benefit of fast energy deconvolution [23].

At the end of the eighties, the interest in investigating the angular resolved low loss region (0–100 eV) in TEM vanished due to its difficult theoretical description. Therefore, the techniques developed in the earlier decades were not improved further, though some papers on angular resolved EELS may be sparsely found [24, 25]. Batson *et al.* performed measurements on several materials, but never published the data [26].

Recently, the development of microscopes with monochromated sources allowing an energy resolution of less than 0.2 eV, as well as the improvement of theoretical understanding and of computational techniques [27–29] has revived the interest in (angular resolved) low energy loss spectrometry [30–35].

Nowadays, two main methods for acquiring angular resolved EELS spectra are known. The older one, used since the beginning of angular resolved EELS acquisitions and well described by Curtis and Silcox [36], consists of recording the focused dispersive image of the electron distribution along an entrance slit with photographic plates. The spectrum image formed in this way is directly related to the energy-loss probability function. However, the angular resolution was obtained at the expense of the energy resolution, which was in the range 1–1.5 eV. Furthermore, this method suffered from alignment problems (finding the optimal parameters of the analyzer or aligning the quadrupole before the spectrometer entrance). This first method vanished with the rise of the second one in the mid-nineties, which was proposed as a result of the development of new EELS acquisition devices such as the Gatan 666 PEELS or the GIF [1]. It consists in projecting a diffraction pattern with known incident and scattering angles on the spectrometer. The desired angular information is selected by a small objective lens aperture. This method may be modified by shifting the diffraction pattern before the entrance slit of the acquisition device instead of using an objective lens aperture to select the desired angular information. The main limitation of this method is the image-coupling in diffraction mode in the crossover of the spectrometer that induces a broadening of the spectral information, thus drastically affecting the energy resolution. A further issue is the very limited area of the diffraction pattern accessed at one time.

1.2 Motivation

The aim of this project is to set up a reliable experimental technique to retrieve the momentum transfer resolved single scattering distribution and dielectric function at very low energy losses with good angular and energy resolutions, and to compare the experimental results with *ab initio* calculations within the time dependent density functional theory and Bethe-Salpeter equation.

The presented experimental technique is based on angular resolved EELS. Indeed, an appropriate data treatment using a Kramers-Kronig analysis (KKA) as sketched in Figure 1.1 in principle allows the retrieval of the dielectric tensor $\boldsymbol{\varepsilon}(\omega, \boldsymbol{q})$ from an EELS spectrum. The advantage of this technique over others is that with a fair spatial resolution (220 nm), a good energy resolution (1 eV) as well as a very good angular resolution (0.5 nm^{-1}) may be achieved.

However, a number of difficulties complicate the task of retrieving the dielectric function from EELS measurements, the most significant being multiple scattering, the presence of the zero loss peak, the resolution of the spectrometer, its aberrations that interfere with the scattering angle and the fact that the orientation of the momentum transfer changes with energy loss.

The angular information is mandatory to obtain the values of $\boldsymbol{\varepsilon}$ for $\boldsymbol{q} \neq \boldsymbol{0}$. The link between the EELS spectrum and the single scattering distribution was first derived by Ritchie in 1957

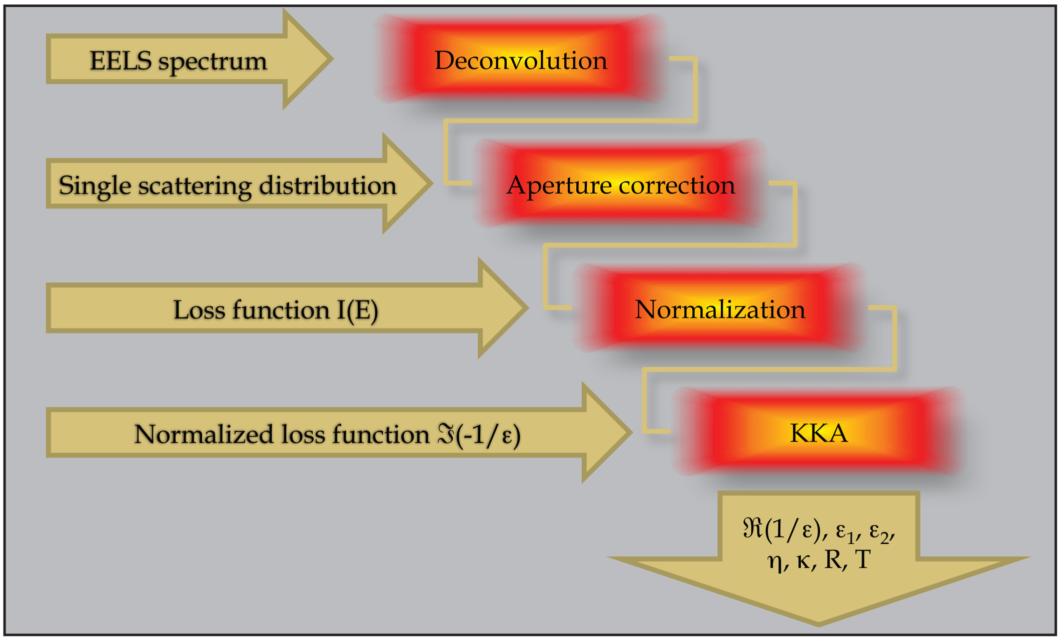

Figure 1.1: Sketch of the data treatment necessary to retrieve the dielectric tensor experimentally from an EELS spectrum.

and is given by [1, 37]:

$$\frac{\mathrm{d}^2\sigma}{\mathrm{d}\omega\mathrm{d}\Omega} \approx \frac{1}{\pi^2 a_0 m_0 v^2 n_a}\left(\frac{1}{\theta^2+\theta_E^2}\right)\Im\left[\frac{-1}{\boldsymbol{\varepsilon}(\omega,\boldsymbol{q})}\right] \tag{1.1}$$

where the surface and relativistic effects are neglected. Taking the case of metallic specimens of average thickness, these effects may be omitted since surface effects are insignificant and relativistic effects such as the Čerenkov radiation do not exist.

Nevertheless, even with the simplified equation (1.1), the Kramers-Kronig analysis is still extremely complicated as it requires a data set from 0 to ∞ in energy, and relies on the use of Fourier transforms. It is therefore sensitive to inaccuracies in the data at low energy, to extrapolations at high energy, and to noise. Consequently, it is preferred to retrieve the normalised momentum dependent loss function $\Im\left(-1/\boldsymbol{\varepsilon}(E,\boldsymbol{q})\right)$ and to compare it to the normalised momentum dependent loss function obtained via *ab initio* calculations. Since these calculations are model-based, experimental results are needed to verify their accuracy.

For this work, silver has been used as a test case. Silver is a noble metal which has the highest electrical and thermal conductivity of all metals as well as the lowest contact resistance. It is thus well suited to plasmonic applications [38], and consequently, a description of the angular resolved loss function is of strong interest. However, the band structure of silver (Figure 1.2) is quite complicated and many different calculations have been proposed to retrieve its dielectric tensor. Experimental investigations on this material are still in progress, this thesis being part of the body of theses studies.

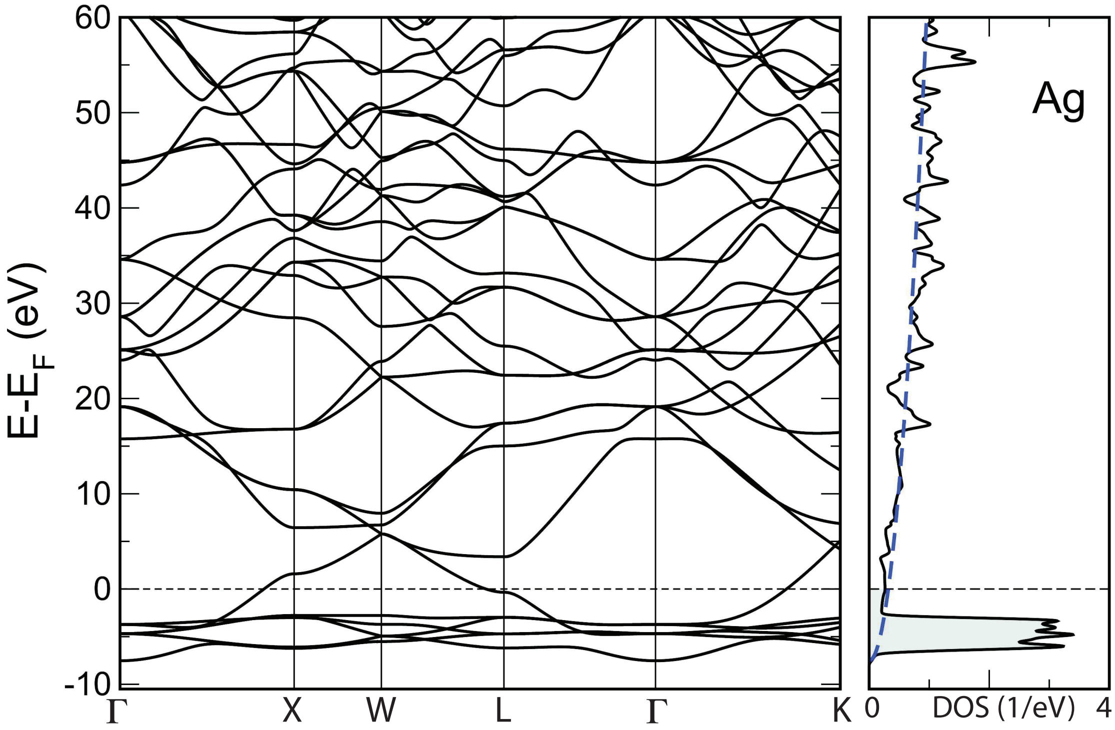

Figure 1.2: Band structure of silver and density of states. The Fermi level is indicated by the dashed line.

1.3 Structure of the manuscript

This manuscript is divided into seven chapters and six appendix sections:

Chapter 2 gives a short overview of the transmission electron microscope and a more detailed description of the instrument used for this work (JEOL 2200 FS).

Chapter 3 summarizes the preparation of the silver samples for TEM observations. The most important steps of the preparation procedure are detailed in Appendix A.

Chapter 4 describes the theory related to this work, in particular scattering, EELS and angular resolved EELS, as well as energy filtered TEM. The back-ground of the theoretical calculations is explained and the dynamics and resolutions defined.

Chapters 5 and 6 show the experimental results obtained and provide details on the method developed in this work. The angular resolved low loss EELS retrieval is explained step by step in chapter 5 and the results obtained with silver samples are presented. They are compared to already published results in chapter 6. All the routines used for the experimental data analysis may be found in Appendix D.

Chapter 7 provides a summary of the whole project and gives an outlook for further possible improvements of the developed method.

Additional information is provided in four appendices. Appendix B gives a comment on notations when working in diffraction mode and Appendix C gives the JEOL alignment routine used within this work with details of the settings of the lenses. Appendix E is an implementation using Mathematica$^{©}$ of the Kröger formula. In contrast to that of Ritchie, the formula takes into account both relativistic and surface effects under a normal incident beam. Appendix F consists of two tables, which give respectively the physical constants and the units employed in this work.

This project has been financed by the Swiss National Science Foundation (SNSF) under number 200021-120308 and performed in the Laboratoire de Spectrométrie et Microscopie Electronique (LSME) and the Centre Interdisciplinaire de Microscopie Electronique (CIME) at EPFL.

2 Instrumentation

2.1 The Transmission Electron Microscope (TEM)

As its name suggests, a Transmission Electron Microscope (TEM) allows to investigate matter by projecting an electron beam on a sample and imaging the transmitted beam. Using electrons instead of photons allows to investigate matter down to the atomic scale. Indeed, the wavelength of visible light is around $\lambda \approx 500$ nm whereas the electrons can have much shorter wavelengths when being accelerated at high energies (*e.g.* a high tension of 200 kV accelerates electrons to a wavelength equivalent to $\lambda = 2.51$ pm). However, the Abbe formula, used for the estimation of the resolution of light microscopes is not fulfilled due to the aberrations of the magnetic lenses, which can only partially be corrected. These aberrations limit the spatial resolution of a transmission electron microscope to about 1 Å (although a recent high-order aberration corrected microscope reached a spatial resolution of 50 pm [39].

It is possible to enrich the possibilities of the microscope by adding various detection devices such as for example X-ray analyzers or in- or post-column spectrometers which can analyze the energy lost by the electron beam. Furthermore, the different possible running modes of the microscope make the transmission electron microscope a powerful tool for material investigation.

Since the electrons needs to travel across the whole microscope column (about 3 m in length), a high vacuum is necessary. A vacuum of $2 \cdot 10^{-5}$ Pa is achieved with a system of turbomolecular, diffusion and vane pumps. An ion pump is used in the gun, where an extremely high vacuum is needed ($\sim 10^{-8}$ Pa).

Once the electrons are accelerated in the gun, they flow through a first set of lenses (the condenser lens system) to form a probe. This probe is finally enlarged/focused with the objective pre-field lens and acts as illumination of the specimen (usually a disc of 2.3 mm or 3 mm in diameter). After passing through the specimen, the electron beam is projected on a phosphorescent screen or an acquisition device (section 2.3).

2.1.1 Image and diffraction mode

Image mode is the most common way of operating. Acting as a "simple" microscope, the TEM magnifies a part of the specimen, allowing atomic resolution. It is thus possible to determine the atomic arrangement and defects in the specimen. The beam path of this operating mode is shown on the left hand side of Figure 2.1.

Diffraction mode is the best way to analyze the crystallographic structure of specimens. Indeed, a correct interpretation of the diffraction pattern determines the crystallographic structure and its defects (if present) [40].

As shown on the right hand side of Figure 2.1, the diffraction pattern of a specimen is easily accessible by changing the strength of the intermediate lens and subsequently the projector lens system.

In the same way than in image mode, the size of a diffraction pattern can be increased. However, it is not measured in term of "magnification", but in "camera length" (CL) (see section 4.1 for explanation). In a TEM, the distances between the specimen and the projection screen (or entrance of the acquisition device) is not physically changed, but modified by changing the focus of the lenses in the projector lens system.

The post-specimen crossover in Figure 2.1 is an important place in the beam path. Indeed, in image mode it pictures a demagnified diffraction pattern and in diffraction mode a demagnified image of the specimen. The higher the magnification/camera length, the smaller the conjugated crossover. This relates to the conservation of the brightness.

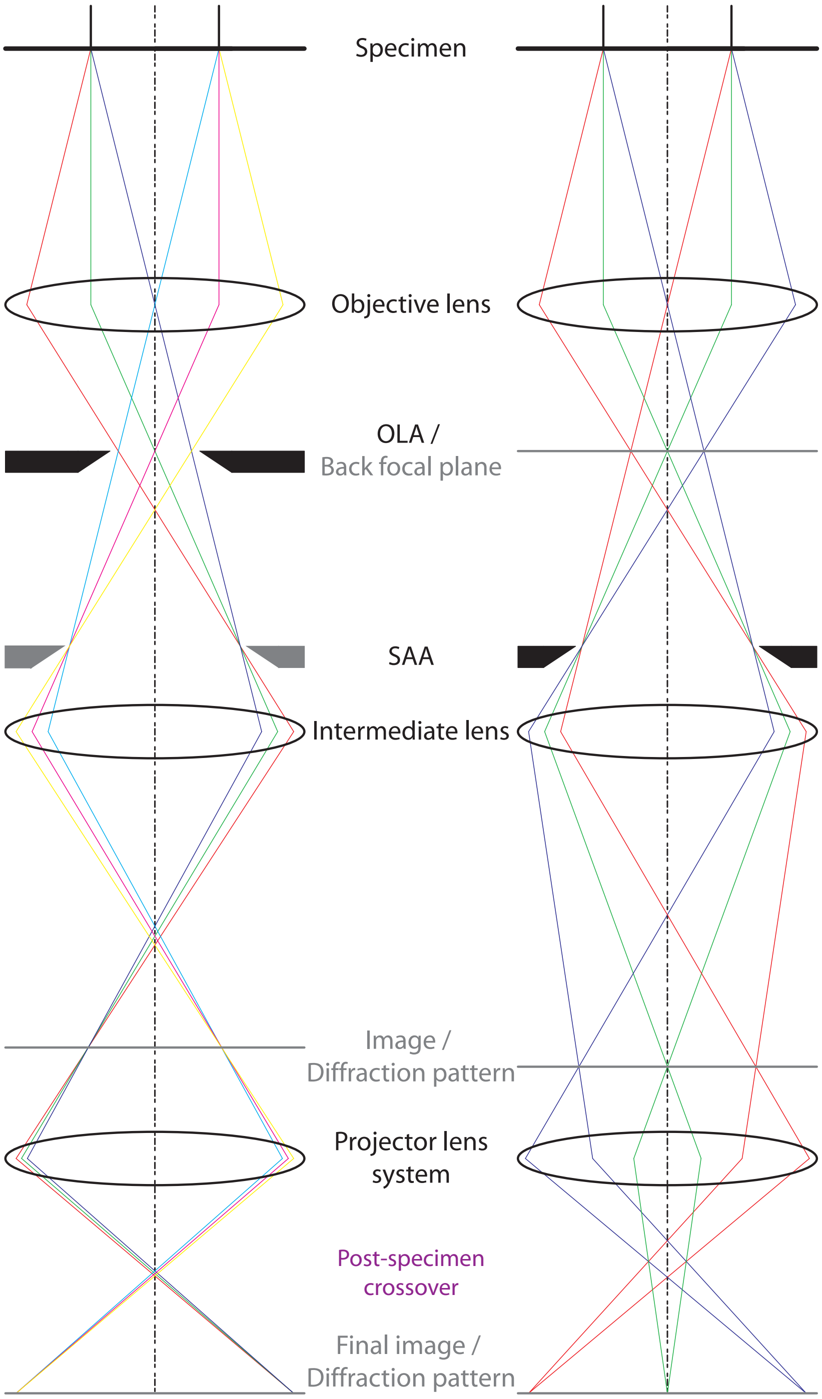

Figure 2.1: Electron beam path when the microscope is operated in standard image (left hand) and diffraction (right hand) mode. Features annotated in gray locate all real image formation and diffraction pattern positions in the column respectively.

2.2 Specificities of the JEOL 2200 FS

The JEOL 2200 FS installed at CIME (Figure 2.2) has following specificities: a Schottky FEG with 80–200 kV HT range, a Cryo pole piece with C_s of 2.2 mm, 0.27 nm point and 0.14 nm lattice imaging resolution. According to the manufacturer, the best energy resolution possible is about 0.8 eV. The microscope is equipped with an in-column Ω filter with an intrinsic dispersion of 1.2 μm/eV at 200 keV, a Gatan UltraScan™ 1000 CCD camera and an imaging plates or film chamber (http://cime.epfl.ch/jeol-2200fs). A Gatan MonoCL3 using the XiClone software (http://www.gatan.com/sem/xiclone.php) has been adapted to the TEM column. A cut-away view of the column with all lenses and apertures is shown in Figure 2.3.

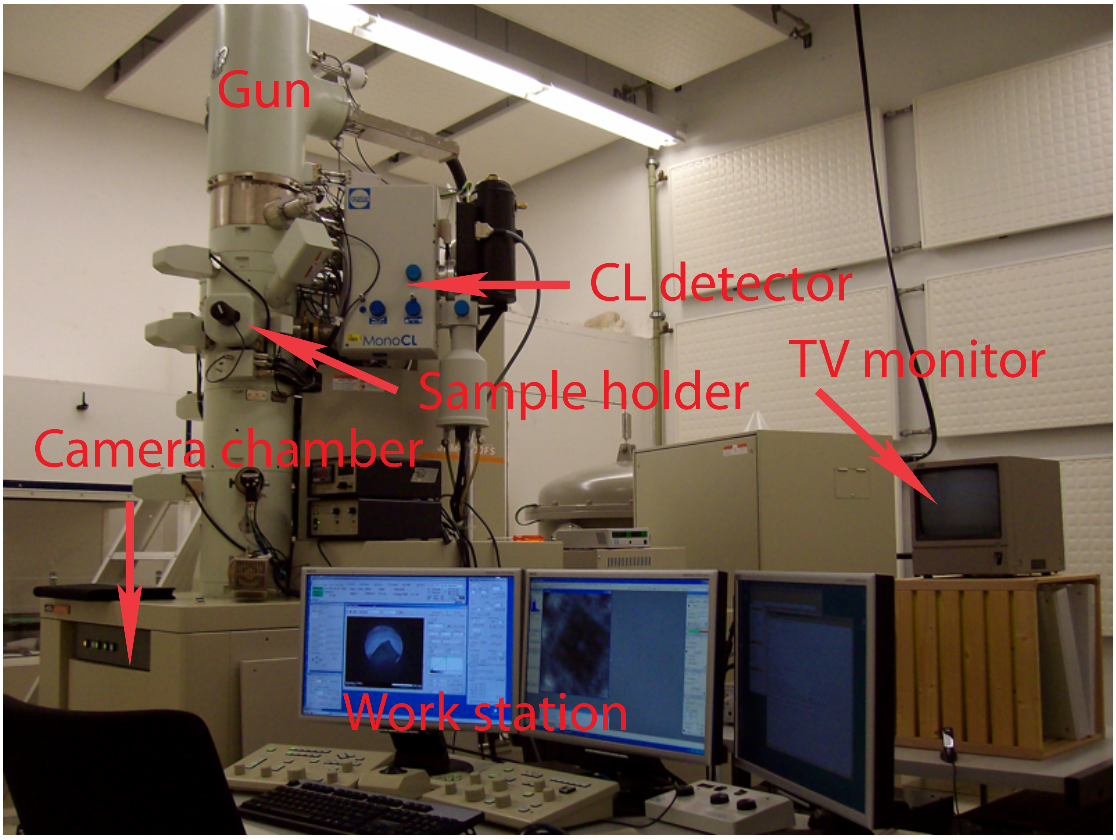

Figure 2.2: Image of the JEOL 2200 FS installed at CIME.

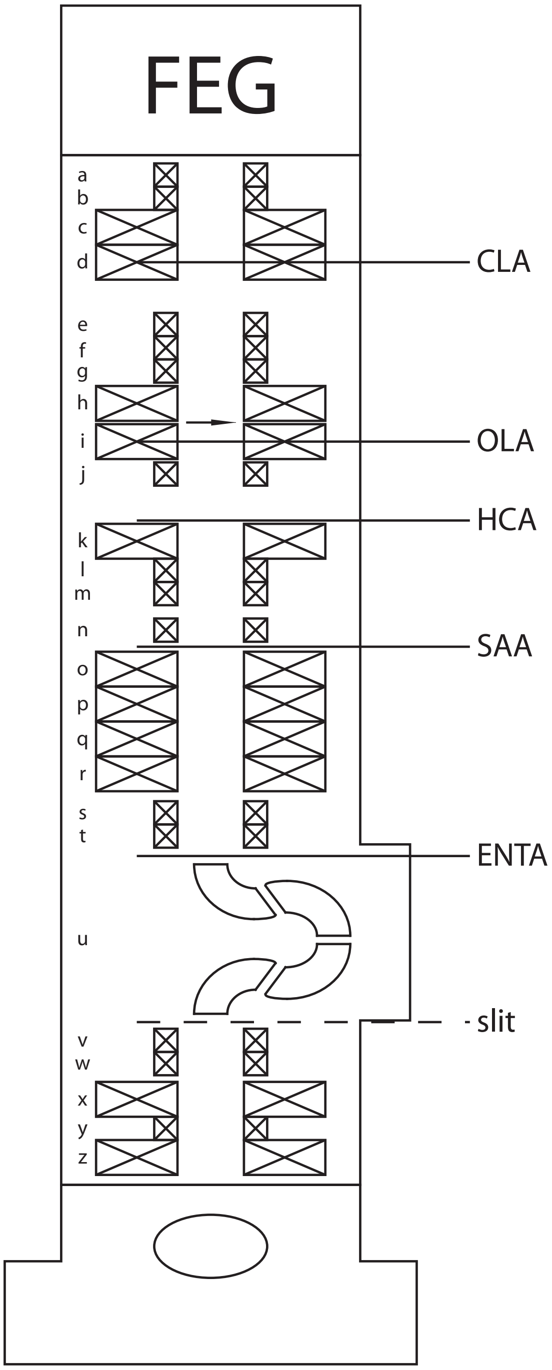

a: GUN-A1	Gun 1st deflector coil
b: GUN-A2	Gun 2nd deflector coil
c: CL1	1st condenser lens
d: CL2	2nd condenser lens
e: CL-STIG	CL stigmator coil
f: CL-A1	CL 1st deflector coil
g: CL-A2	CL 2nd deflector coil
h: CM	Condenser minilens
i: OL	Objective lens
j: OL-STIG	OL stigmator coil
k: OM	Objective minilens
l: IS1	1st image shift coil
m: IS2	2nd image shift coil
n: IL-STIG	IL stigmator coil
o: IL1	1st intermediate lens
p: IL2	2nd intermediate lens
q: IL3	3rd intermediate lens
r: IL4	4th intermediate lens
s: FL-STIG1	Filter lens 1st stigmator coil
t: FL-A1	Filter lens 1st deflector coil
u: FL	Filter lens
v: FL-A2	Filter lens 2nd deflector coil
w: FL-STIG2	Filter lens 2nd stigmator coil
x: PL1	1st projector lens
y: PL-A	IL deflector coil
z: PL2	2nd projector lens

Figure 2.3: Cut-away view of the JEOL 2200 FS, showing all the lenses and apertures. The specimen is represented by an arrow. Source: instruction handbook of the JEM-2200FS.

2.2.1 The Field Emission Gun (FEG)

There are two main classes of electron sources (so-called "guns") for TEM: thermionic and field emission guns. The main difference between these two kind of guns is the way the electron beam is generated. Where a tungsten wire or a crystal (LaB_6 or CeB_6) is heated to emit electrons for a thermionic gun, an electric field pulls the electrons out of the tip (single-crystal tungsten (W) for a cold FEG or Zirconium oxide (ZrO) coated <100> tungsten maintained at a high temperature around 1700K for a Schottky FEG). The principle of a Schottky FEG is to enhance a thermionic source by lowering the emission barrier with a strong electric field.

The JEOL 2200 FS used for this work is equipped with a Schottky FEG. The main advantage of the FEG over a thermionic source is the much higher brightness (up to tree orders of magnitude), the higher coherence, a narrower energy distribution, the possibility to create a much smaller electron beam in diameter, and from a technical point of view, the lifetime (5 times higher than a LaB_6). Contrary to the cold FEG, the Schottky FEG has a symmetrical energy distribution. Table 2.1 shows the main characteristics of the different electron sources mentioned (source: [40]).

Table 2.1: Characteristics of the principal electron sources.

	Units	Tungsten	LaB_6	Schottky FEG	Cold FEG
Operating temperature	K	2700	1700	1700	300
Current density (at 100 kV)	$A{\cdot}m^{-2}$	5	10^2	10^5	10^6
Gun crossover size	nm	$> 10^5$	10^4	15	3
Brightness (at 100 kV)	$A{\cdot}m^{-2}{\cdot}sr^{-1}$	10^{10}	$5 \cdot 10^{11}$	$5 \cdot 10^{12}$	10^{13}
Energy spread (at 100 kV)	eV	3	1.5	0.7	0.3
Lifetime	hr	100	1000	> 5000	> 5000

The most important characteristics for this work are the brightness and the energy spread. The characteristics of the JEOL 2200 FS at CIME are 0.8 eV energy resolution (zero loss FWHM) and a brightness of $4 \cdot 10^{12}$ $A{\cdot}m^{-2}{\cdot}sr^{-1}$ at 200 keV according to the manufacturer.

2.2.2 The in-column Ω filter

As shown in Figure 2.3, the Ω filter is placed in the TEM column just before the projector lenses. Its name comes from the Ω-like shape the electron beam travels while flowing through the prisms, as shown in Figure 2.4.

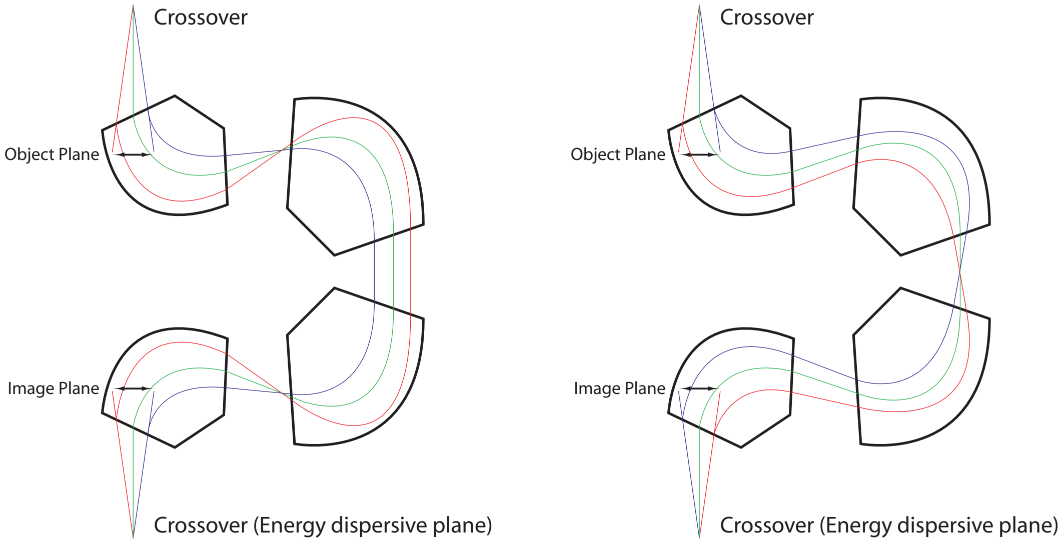

(a) Beam path in x plane

(b) Beam path in y plane

Figure 2.4: Beam path through the Ω filter in the x plane and the y plane, perpendicular and parallel to the magnetic field of the filter lens respectively. Source: instruction handbook of the JEM-2200FS.

The first in-column filter has been developed by Castaing and Henry in 1962 [15] (Figure 2.5a). However, the necessity of an electrostatic mirror limits the usability of this kind of filter to beam energies of 100 kV maximum. Therefore, a new Ω shaped filter design made uniquely of magnetic lenses has been introduced by Senoussi *et al.* in 1971 [41]. The first test on an Ω filter has been performed in Toulouse by Zanchi *et al.* [42]. Since then, different Ω filters have been designed and improved [43–46]. In the mid-eighties, Perez *et al.* simulated another in-column filter design known under "α filter" [47], which however has never been built. A further design where the entrance and exit beam cross twice within the filter and the aberration correction calculated has been published by Uhlemann and Rose [48]. The filter has recently been manufactured and used in the SESAM project [49] under the acronym MANDOLINE (Figure 2.5b).

There are two possible operation modes for an in-column filter: as a spectrometer or as an energy filter (Figure 2.6). In the first case, the whole energy spectrum can be projected on one of the different acquisition devices.

The second operation mode is possible by inserting a slit in the energy-dispersive plane at the exit of the filter, as shown in Figure 2.7. The width and the horizontal position of the slit

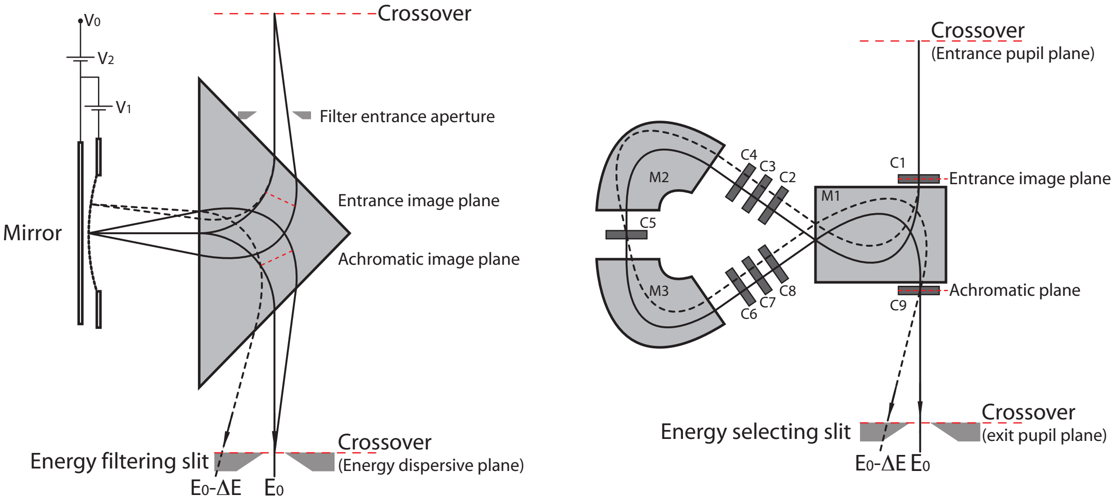

(a) Castaing-Henry filter

(b) MANDOLINE filter

Figure 2.5: Beam path in the Castaing-Henry filter (a) and in the MANDOLINE filter(b). The solid line corresponds to the beam without energy loss and the dashed line corresponds to the path of electrons which underwent an energy loss ΔE. The red dashed lines indicate special planes in the filter. In (b), M1 is a homogenous magnet, M2 and M3 two symmetrically arranged inhomogeneous magnets and C1–C9 are aberration correction sextupoles.

are variable, allowing the selection of a central energy position and an energy range around it. This way of doing is then called Energy Filtered Transmission Electron Microscopy (EFTEM) and is explained further in section 4.4.

As the JEOL 2200 FS has a complete projecting lens system before the filter (the intermediate lens system), it can produce either a diffraction pattern or an image as the entrance object of the filter. Thus, the JEOL 2200 FS can be operated in four different modes: image/spectrum, diffraction/spectrum, image/EFTEM and diffraction/EFTEM. Some confusion may arise from the fact that the EFTEM mode is often called image mode as opposed to spectrum mode. In the spectrum modes, the energy-dispersive plane of the filter is taken as object for the projector lens system, whereas the exit pupil plane is used in EFTEM modes. The link between the exit pupil plane and the energy-dispersive plane is shown in Figure 2.8. It is to notice that the exit pupil plane shown in this figure is virtually reconstructed by back-projection from the slit plane, as the real exit pupil plane is distorted on the beam path within the last magnet of the filter. From the beam path, it is clear that a diffraction pattern is formed in the energy-dispersive plane when an image is in the exit pupil plane and vice-versa. Since the entrance pupil and the exit pupil are conjugated, as well as the entrance crossover is conjugated with the exit crossover of the filter (the energy-dispersive plane), an image is formed in this last plane in diffraction EFTEM mode. This is the so-called "image coupling in diffraction mode".

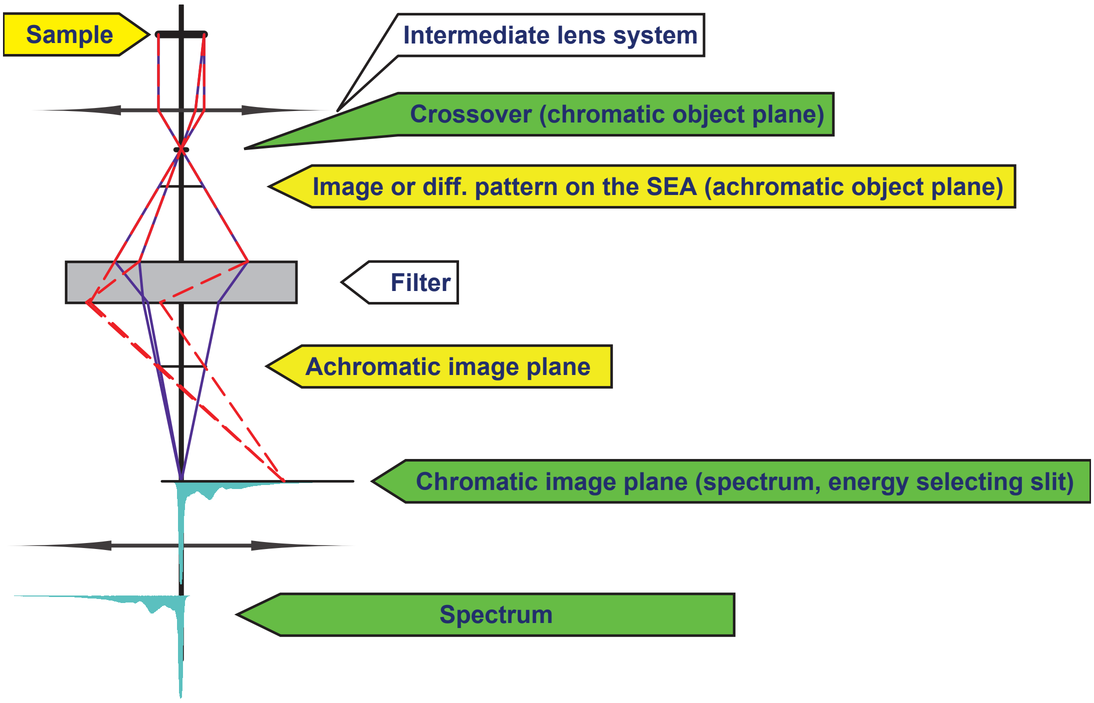

(a) Filter as a spectrometer

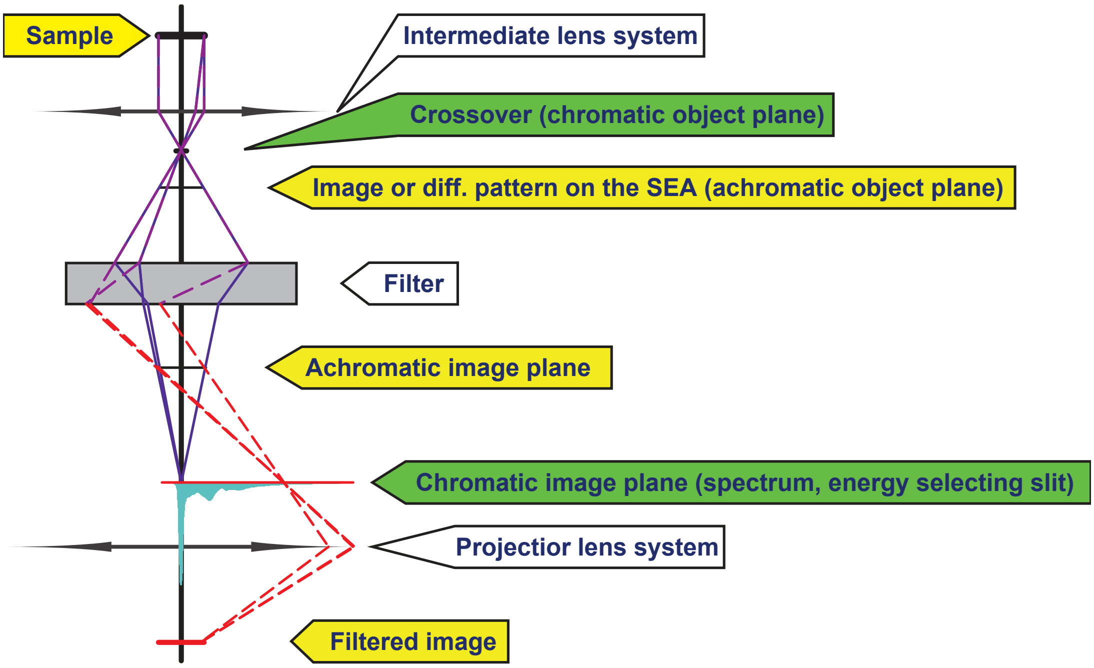

(b) Filter as an energy filter

Figure 2.6: Operation modes of an energy filter, either as a spectrometer (a) or as an energy filter (b). In both cases, the entrance object of the filter is the object imaged in the crossover after the illumination lens system. The projector lens system is tuned to project either the whole spectrum from the chromatic image plane or the filtered image from the achromatic plane depending on the operation mode of the filter. The planes of same colors are conjugated.

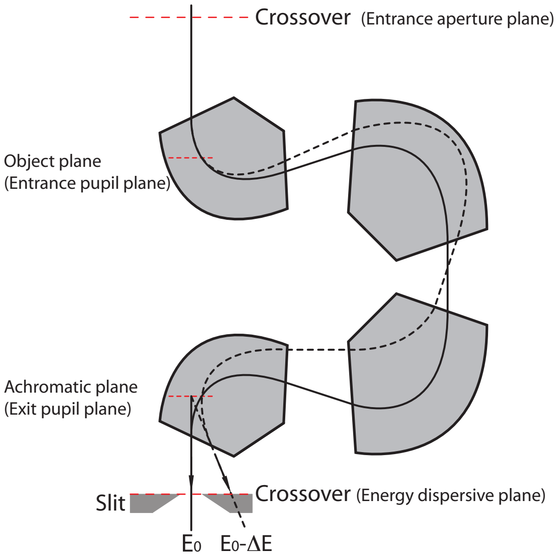

Figure 2.7: Ray path in the specific case of the JEOL Ω filter. The red dashed lines correspond to the special planes in the filter: the entrance and exit crossovers and pupils. Image source: instruction handbook of the JEM-2200FS.

The geometry of the Ω filter is not trivial. Indeed, at least tree conditions have to be fulfilled to avoid aperture and distortion aberrations and to get an achromatic image on the exit pupil plane [46, 50]:

1. the geometry of the filter must be central plane symmetry;
2. the central trajectory at the slit plane must be parallel to that at the entrance aperture plane;
3. two pairs, the entrance aperture plane and the slit plane, and the entrance pupil plane and the exit pupil plane must be symmetric about the central plane.

Thanks to the central symmetry, almost half of the second rank aberrations vanish. Curving the inner pole-piece surface of the magnet or curving the entrance and exit faces of the pole-piece generates a sextupole filed [51], thus no additional magnets are needed for further second rank aberrations correction. The Ω filter is manufactured in such a way that the remaining aberrations which cannot be completely corrected are minimised. One of the most important remaining aberration is the non-isochromaticity, which is treated in section 5.1.1.

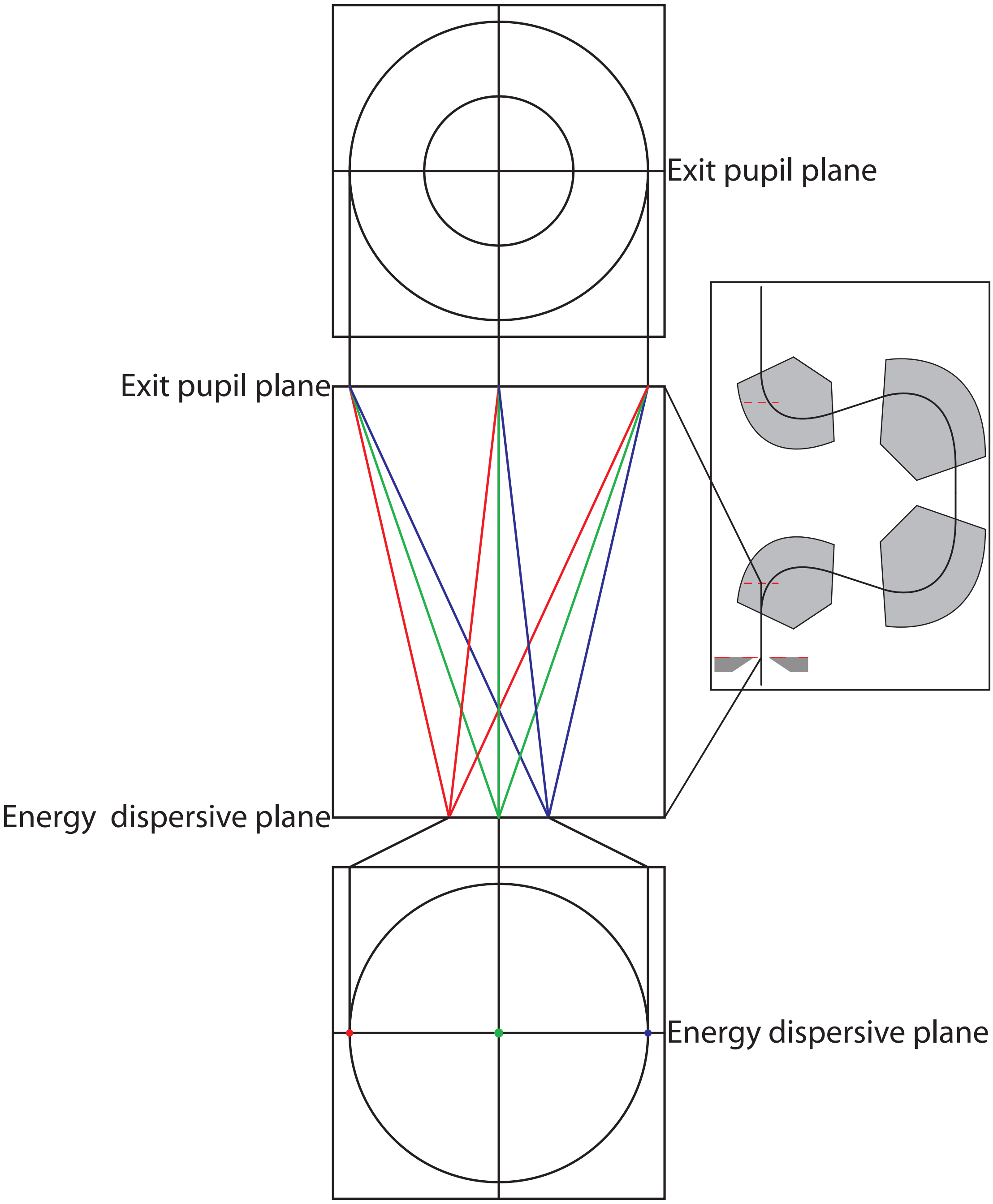

Figure 2.8: Link between the exit pupil plane and the energy-dispersive plane. A diffraction pattern is formed in the energy-dispersive plane when an image is in the exit pupil plane and vice-versa.

2.2.3 Nano-Beam Diffraction (NBD)

Preliminary remark: even if JEOL uses the acronym NBD as "Narrow Beam Diffraction" (instruction handbook of the JEM-2200FS), the possibility of creating a probe in the nm scale (down to 1.0 nm), induces people to call this mode "Nano-Beam". This last name or the acronym will be used in this work.

The NBD mode is a particular sample illumination mode possible with the JEOL transmission electron microscopes. The standard use of this illumination mode is thought to have nano-scale probe for conventional diffraction, allowing to generate a diffraction pattern from a very small area. However, and this is what is used for this work, it is possible in this mode to set up a parallel illumination in the range of 50–500 nm diameter depending on the selected Condenser Lens Aperture (CLA) [52] without a selecting area aperture. Figure 2.9 shows the illumination of the specimen in TEM parallel illumination mode with a selecting area aperture inserted (left hand side) and in NBD parallel illumination mode (right hand side). The Selecting Area Aperture (SAA), back-projected on the specimen, induces a virtual aperture that limits the illuminated area. However, since the area covered by the parallel incident beam is much larger than the size of that virtual aperture, the intensity of the beam after the SAA is weak. In NBD mode, the size of the illuminated area when the illumination is parallel depends only on the size of the condenser lens aperture. The full intensity of the incident beam is concentrated on the illuminated area and thus the total intensity after the specimen much brighter than in TEM SAA mode.

Therefore: the main advantage of the NBD illumination mode is the possibility to have a parallel beam on a small illuminated area and with high intensity.

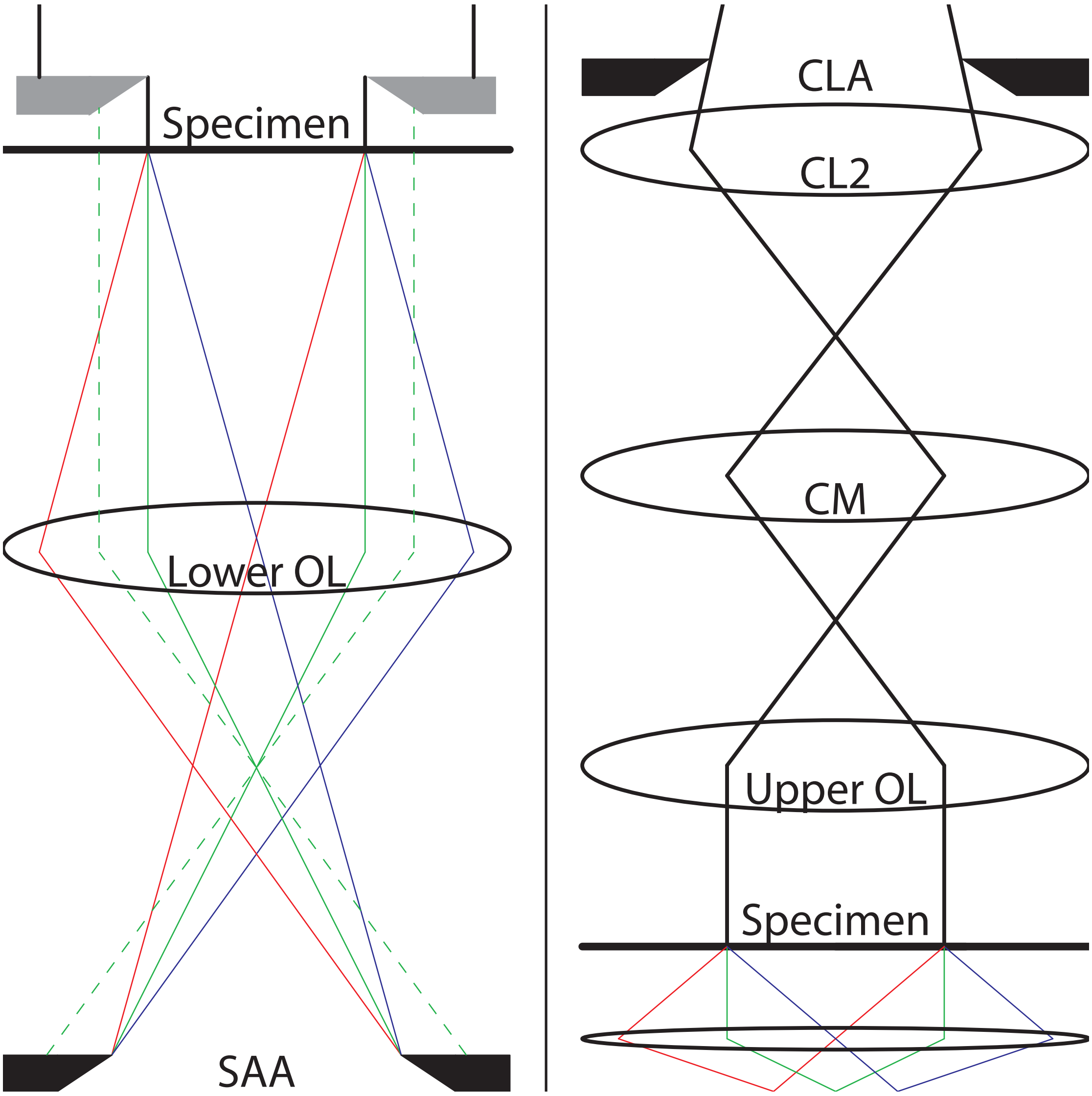

Figure 2.9: Beam path for parallel illumination in TEM SAA (left hand side) and in NBD mode (right hand side).

2.3 Acquisition devices

Since the beginning of TEM, a phosphorescent screen has been used to detect the high-energy electron beam. In the JEOL 2200 FS, a camera is pointed toward the screen and sends the image to a computer. Snapshots can then be taken.

Lifting up the phosphorescent screen gives the possibility to access a Gatan UltraScan™ 1000 CCD camera. This is a 2k × 2k pixel device for a total detection area of 28.7 × 28.7 mm with a pixel size of 14 μm. The maximal amount of counts before saturation is 64'000, giving a dynamic range of 16 bits. The read-out speed is 4.0 Mpx/sec and the read-out noise lower than 30 CCD electrons.

Retracting the CCD camera makes the way free to the camera chamber, where photographic films or Imaging Plates (IP) can be inserted. Since the development of the negative films is quite complicated and the film itself is "one way use", this technique is not really used any more. On the other hand, imaging plates are still used. Indeed, they have several advantages: they can be re-used up to 1000 times according to the manufacturer (http://www.ditabis.de/imagingplatescanner_micron.html), the scan is automated resulting in high-resolution digital images, the detection area is much larger than for a CCD camera (81 × 100 mm) with the same pixel size of 14 μm, the dynamic range is linear over 6 orders of magnitude [53] and the maximum electron dose per pixel is much higher allowing longer acquisition times (a performed test leads to the conclusion that the IP saturates at about 4 times longer exposure time than the CCD camera). IP's are particularly interesting in diffraction mode since the device cannot be damaged by high electron dose.

The acquisition principle is as follow: an electron from the beam reacts with the active layer of the IP, which is a photostimulable phosphor layer with highly dispersed, doted (BaF(Br,I):Eu^{2+}) crystals. The incident electron generates several electron-hole pairs in the active layer, which then are trapped by the Fluor centers of the crystalline structure [54]. The generation of multiple electron-hole pairs induces a primary signal amplification of a factor 10^2–10^3.

The read-out is performed in a scanner, which stimulates the populated F-centers of the IP with a laser at about 630 nm wavelength so that the electron-hole pairs can recombine, radiating isotropically from the surface of the IP at a wavelength of 390 nm (the luminescent signal). This signal is then collected by an elliptical mirror system and reflected to a photomultiplier and finally converted into a digital signal.

One of the major disadvantage of imaging plates is the loss of Detection Quantum Efficiency (DQE) at higher dose. Indeed, for an electron dose higher than 0.5 $e^-/\mu m^2$, the DQE of 0.8–0.9 decreases rapidly down to 0.2 due to a noise signal depending on the IP inhomogeneities, the photomultiplier, the electronic devices and contribution of the Poisson distribution of the laser beam, even with a high-DQE imaging plate scanner [55]. Recently, the lowering of the characteristic noise of the IP by correction of the geometric distortion could improve the DQE to almost 0.5 even for electron doses as high as 10 $e^-/\mu m^2$ [56].

3 Silver sample preparation

The samples used in the present work are all pure silver (except if explicitly mentioned). The requirements for the presented technique are a homogenous thickness of 30–50 nm over an area of at least 250 nm in diameter, and there should be no contamination even with very large exposure times on the same area.

Several different chemical or mechanical sample preparation techniques are presented in this chapter, even if the resulting specimen is not good enough for this work, because almost no free accessible literature exists for silver TEM sample preparation.

3.1 Raw silver sample description

The sample used for mechanical and chemical preparation is 99.999% pure silver bought at *Alfa Aeser* (http://www.alfa-chemcat.com/). The bars have a length of 25 mm and 7 mm diameter (reference number 11473). Figure 3.1 shows the edge and the bottom respectively from one of the bars, which has been chemically etched with nitric acid to reveal the grains. This bar has been used to create two carrots of 3 mm diameter, which have finally been processed by Electrical Discharge Machining (EDM) to 100 μm thin slices in a first time, 200, 300 and 400 μm in a second time because 100 μm slices had tendency to bend while cutting, inducing dislocations. The sample preparation web page http://temsamprep.in2p3.fr gives different preparation techniques for silver:

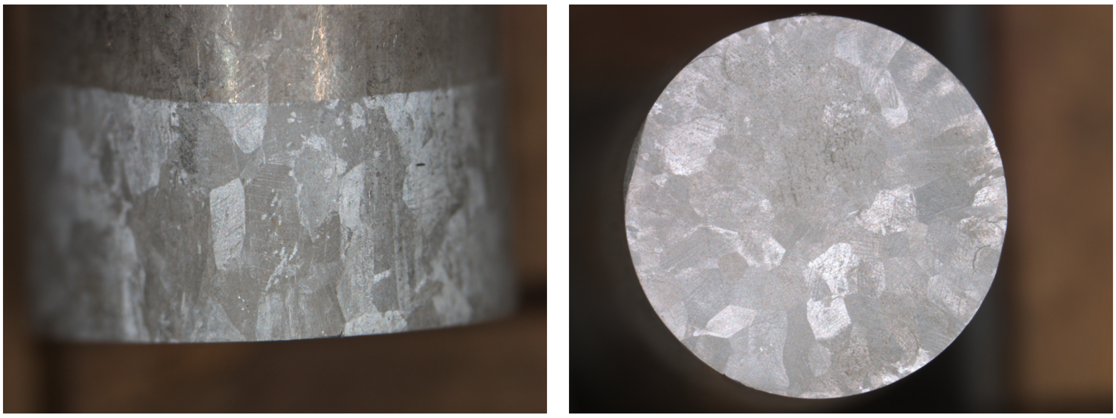

(a) Bulk silver: edge

(b) Bulk silver: bottom

Figure 3.1: Optical microscope analysis of the surface of a piece of bulk silver. The grain size seems to be about 1 mm and the surface quite rough. This roughness is probably due to the slab preparation with EDM.

1. twin jet electrolytic thinning;
2. full bath electrolytic thinning;
3. twin jet chemical thinning;
4. full bath chemical thinning;
5. ion beam thinning;
6. focused ion beam thinning;
7. extractive replicas;

from which techniques 1, 5 and 6 have been used. The results of different attempts are presented hereafter, and the tables with the technical data can be found in Appendix A.

3.2 Mechanical thinning

3.2.1 Ion Beam Thinning (IBT)

The very first sample has been prepared using a Fischione 1010 Ion Mill instrument on a 100 μm slab. A tension of 5 keV and 6 mA of current have been used with an attack angle of 6° on the cooled down sample. This treatment applied for a total of 7 hours created three little holes with thick edges. The same sample has been put again into the milling device with 5 mA at 2.5 keV and an attack angle of 4° for 1.75 hours, followed by 1.5 hour at 3 keV and 3 hours at 500 eV. A resulting edge is shown in Figure 3.2. This method has been abandoned after this first attempt because it is extremely time consuming with a very poor result (thick specimen, defects).

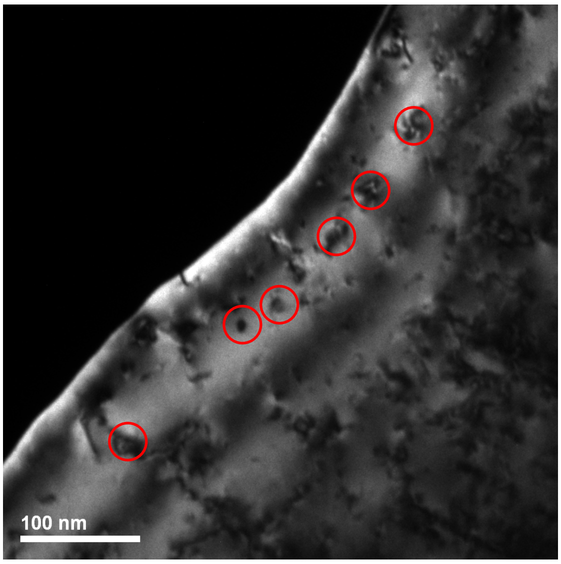

Figure 3.2: Result after a total IBT of 13.25 hours with different milling conditions. This dark field image at 38 kx magnification reveals a thick edge full of dislocations (red circles).

3.2.2 Focused Ion Beam (FIB) thinning

The FIB is an extremely useful tool for sample preparation. Indeed, it allows a very precise TEM sample preparation (depending on the considered material for sample preparation, a precision of 100–200 nm in thickness is guaranteed; every thickness below is a lottery since the measurements are no more accurate) and in the same time, a SEM surface analysis can be performed. This has been done on a 300 μm silver slab described at the beginning of this section, revealing the size of some grains at almost 3.5 μm, but most of them being much smaller with a size about 200 nm (Figure 3.3a). The analysis also reveals a quite rough surface (Figure 3.3b). The surface roughness, showing some porosity (the black dots, well visible also in Figure 3.4b), is most probably due to the slab preparation by EDM.

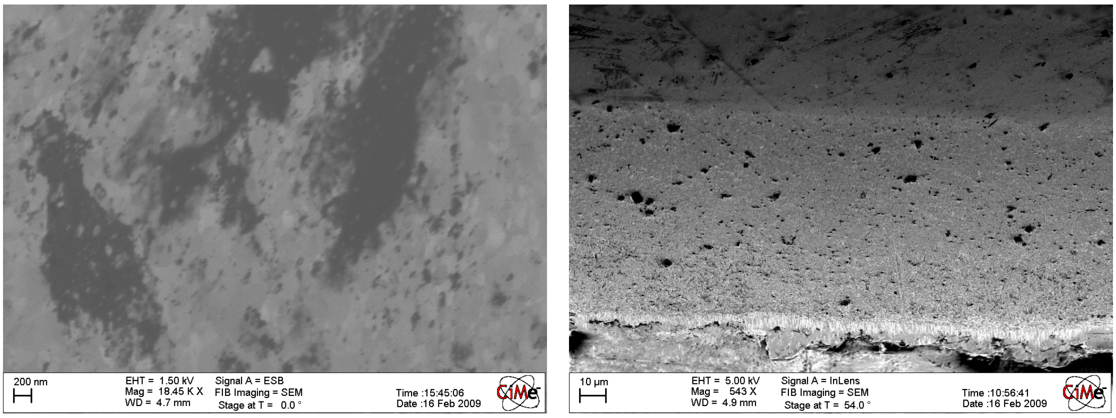

(a) SEM analysis: grain size

(b) SEM analysis: surface roughness

Figure 3.3: FIB SEM analysis of the surface of a piece of bulk silver. The grain size seems to be about 1 μm and the surface quite rough. This roughness is probably due to the slab preparation with EDM.

The TEM sample has been prepared by the "FIB H-bar" technique, well described in [57, 58] and many others. It consists in milling a thin lamella out of the bulk material, lift it out and stick it on a special TEM FIB lamella holder (*e.g.* an Omniprobe® Lift-Out grid, http://www.tedpella.com/Omniprobe_html/FIB-Omni.htm). Figure 3.4 shows the H-bar sample just before the lift-out.

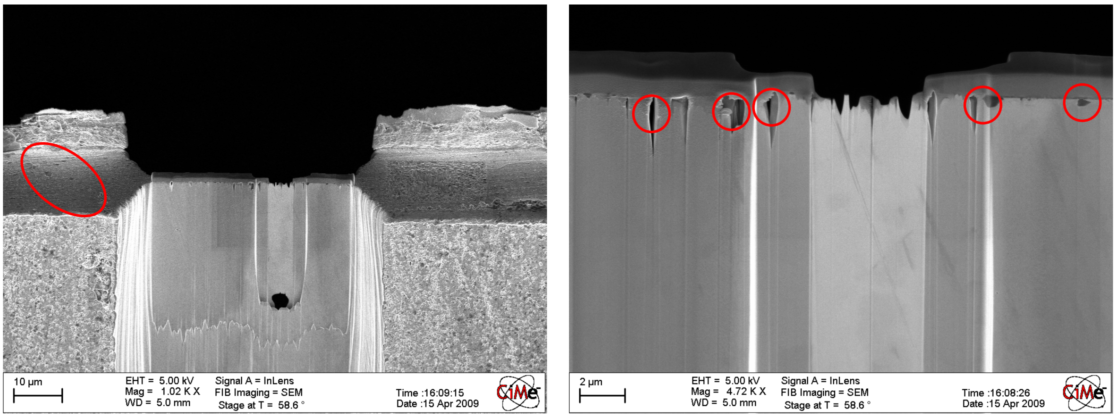

(a) FIB H-bar cut

(b) FIB H-bar: closer look at the thin zone

Figure 3.4: FIB H-bar cut just before the lift-out. A closer look at the thin zone reveals a surface porosity (red circles).

When the FIB lamella is put into a TEM, it reveals the thin H-bar zone, as shown in Figure 3.5a. Going to higher magnification (Figure 3.5b), single grains with 200 nm length can be discovered. As expected for a ion sample preparation, plenty of dislocations can be observed. For this last reason, this sample preparation method has been discarded from the current work.

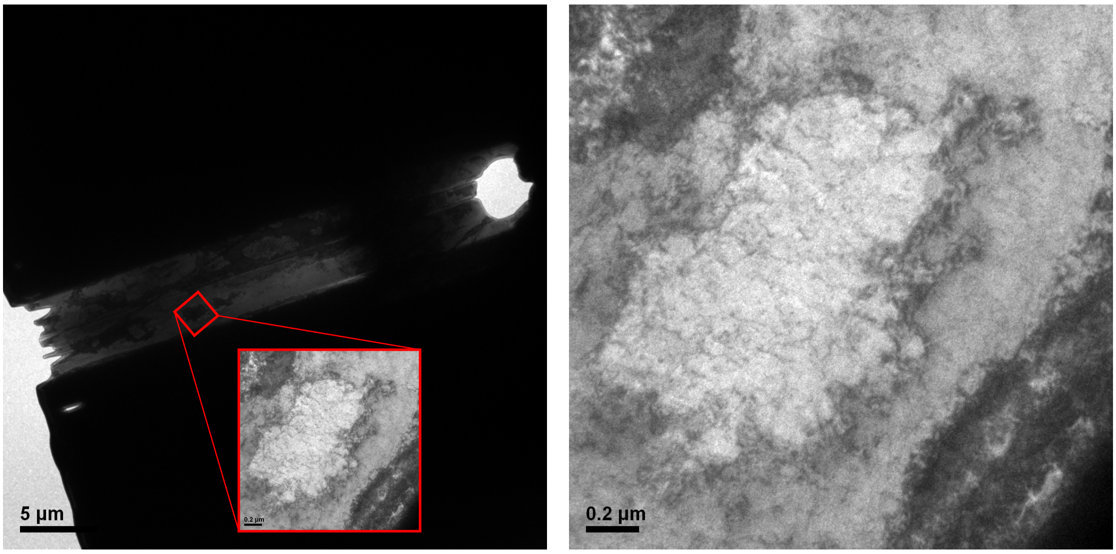

(a) TEM view from the H-bar cut (b) Single grain in the thin zone of the FIB lamella

Figure 3.5: TEM view of the FIB lamella. A closer look at a single grain reveals the expected dislocations induced by the ion thinning sample preparation method.

3.3 Electrochemical thinning

Electrochemical thinning is a widely used preparation method, which has the great advantage to keep the crystalline structure of the sample unchanged, *i.e.* without introducing dislocations. Several attempts have been performed by twin jet polishing using a Struers TenuPol-5, and discarded for reasons explained hereafter.

3.3.1 Twin jet polishing with phosphoric acid

The first electropolishing attempt has been performed with a phosphoric acid solution, proposed by Struers GmbH. The composition of the electrolyte is:

- 400 ml H_3PO_4@65% (phosphoric acid);
- 380 ml C_2H_6O (ethanol);
- 200 ml H_2O (distilled water).

A typical sample resulting from this process is shown in Figure 3.6: the sample is almost destroyed, and the amount left is black and rough. These samples have not been put into a TEM since it is obvious that they are not suitable for a proper analysis. The result of all polishing attempts with phosphoric acid can be found in the annex, Tables A.1 and A.2.

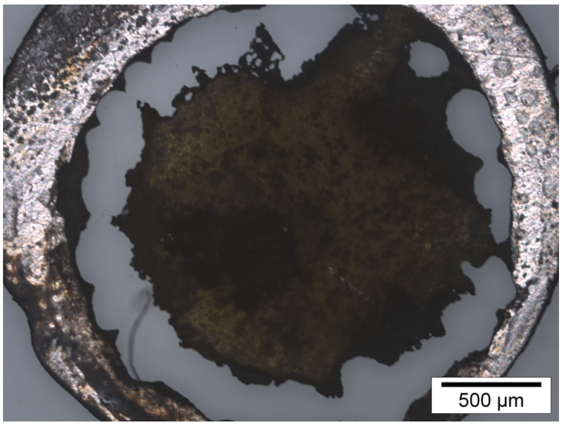

Figure 3.6: Result from a twin jet polishing process with a phosphoric acid electrolyte. The sample is almost destroyed and the rest is unusable.

3.3.2 Twin jet polishing with perchloric acid

It seems obvious that the phosphoric acid solution suggested by Struers GmbH does not work for the purpose of this project on the silver slabs, so another solution proposed by Cockayne *et al.* [59] has been tried. The idea is to start jet polishing with nitric acid and finish thinning with a perchloric acid bath. These mixtures are composed as follows (prepared one day before use):

- nitric acid mixture:
  - 150 ml HNO_3@65% (nitric acid);
  - 850 ml H_2O (distilled water);
- perchloric acid mixture:
  - 10 ml $HClO_4$@60% (perchloric acid);
  - 900 ml CH_3OH (methanol);
  - 90 ml $C_3H_5(OH)_3$ (glycerol).

The resulting samples are shown in Figure 3.7. Obviously, the nitric acid solution is too corrosive for the silver, so it has been left out on the second day (see Table A.3 and A.4 for full analysis). Under the light microscope, this last solution seems to be the right one, but putting the sample in a TEM shows (Figure 3.8) that the sample is not thin enough, especially the need for thin homogenous regions of at least 250 nm with equal thickness are not fulfilled.

Having a closer look at Figure 3.7b, one can notice little scratches in the thinned area, which appear systematically when only perchloric acid is used as electrolyte. The question raised if they are just an optical illusion. They are not, as next section will show.

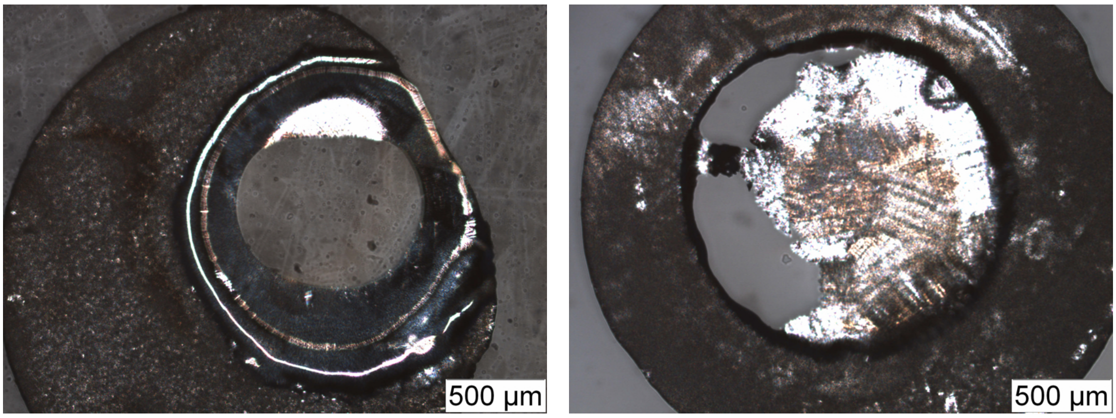

(a) Combination of nitric and phosphoric acid

(b) Second attempt with phosphoric acid only

Figure 3.7: Silver preparation using nitric and perchloric acid as electrolyte. (a) is the result using Cockayne *et al.* method and (b) results from using only the perchloric acid solution as electrolyte.

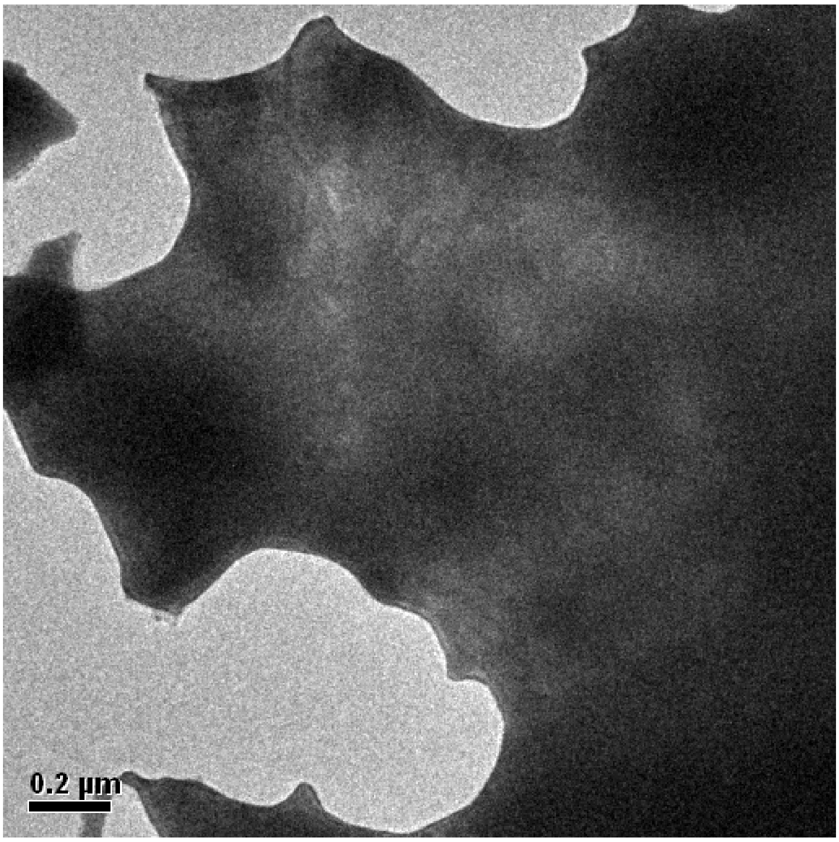

Figure 3.8: TEM analysis of a perchloric acid twin jet polished silver sample. The sample is rather thick and not homogeneously flat.

3.3.3 Twin jet polishing with sulfuric acid

The perchloric acid electrolyte is not performing enough, so another technique has been applied: a method proposed by Lyles *et al.* [60], and used by prof. Sigle[1] and his team for surface plasmon analysis [61]. The electrolyte is based on sulfuric and acetic acid mixed with thiourea and has to be mixed in this special order:

- 115 ml CH_3COOH (glacial acetic acid);
- 86 ml H_2SO_4 (concentrated sulfuric acid);
- 700 ml CH_3OH (anhydrous methyl alcohol);
- 154 g NH_2CSNH_2 (thiourea).

Representative results of this technique are shown in Figure 3.9. Again, and this is recurrent also with sulfuric acid prepared slabs, these scratches mentioned before are visible (Figure 3.9b). They seem to be grain oriented, and there is no explanation of the happening. A suggestion may be preferential attack, but if it is, the reasons are not clear.

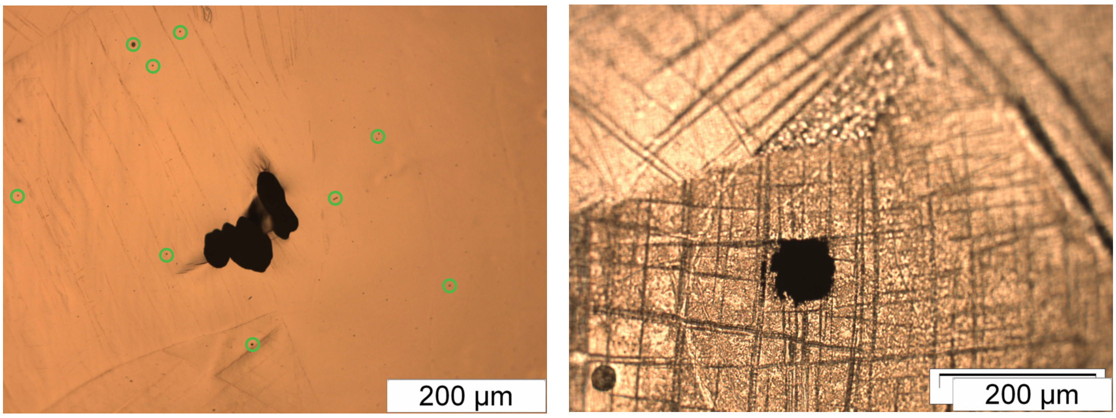

(a) Sulfuric acid prepared slab

(b) Sulfuric acid prepared slab with well visible scratches

Figure 3.9: Silver preparation using a sulfuric acid solution as electrolyte. Scratches are slightly visible in (a) and strongly evident in (b). The green circles in (a) show some contamination.

Using the sulfuric acid method has another drawback: since thiourea is a powder, if the mix is not perfect, some residue may remain on the sample as contamination, as shown by the green circles in Figure 3.9a. A closer look at this same sample in a TEM (Figure 3.10) shows dislocations, probably due to the slice preparation by EDM.

A summary of the sulfuric acid technique used by Lyles *et al.* , Sigle *et al.* and this work can be found in Table A.6.

---

[1] Prof. Wilfried Sigle, Max Planck Institute for Metals Research, Stuttgart.

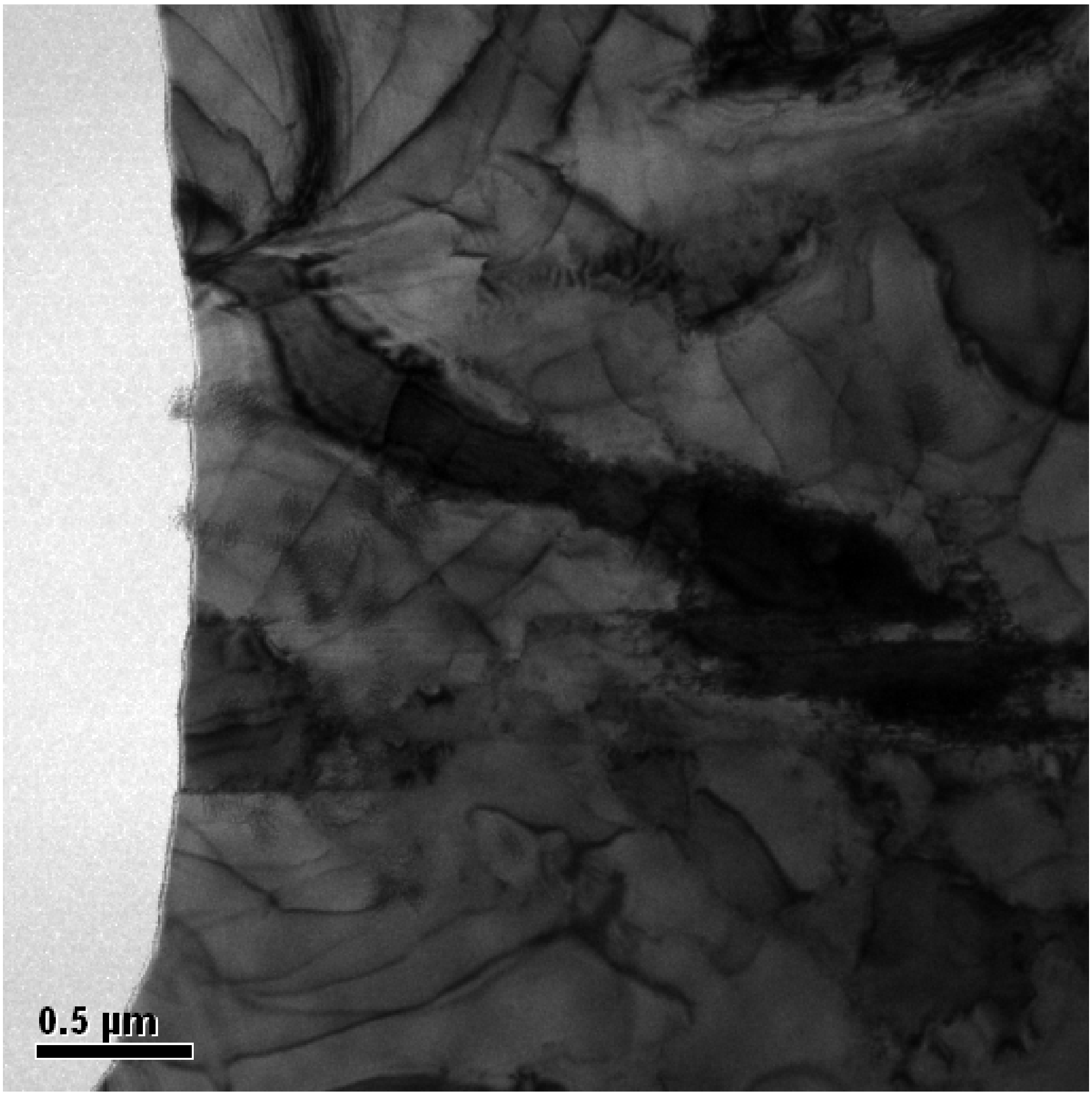

Figure 3.10: TEM analysis of a sulfuric acid solution prepared silver slab. The dislocations probably come from the EDM cut of the silver carrot.

3.4 Sputtering

All these attempts to create usable monocrystalline samples failed, thus a try with polycrystalline sample prepared by sputtering has been performed. This turned into a success.

Sputtering was performed with a NORDIKO 2000 (Nordiko Ltd, Havants, Hants, UK) magnetron sputtering machine. 99.99% pure Ag target (from Kurt J. Lesker) was used for depositing the film. 50 W (380 volt) DC power was applied on the target to start the deposition with 20 sccm Ar flow in the chamber; pressure was maintained at 5 mTorr. Deposition rate was observed to be 50 nm/min. The substrate was freshly (111) cleaved NaCl single crystal (usually called rock salt) clamped on a 4 inches Si wafer. The sputtered film can then be easily released by putting the substrate into distilled water and fishing the film with a copper grid after the salt dissolved. This method has first been proposed by Layton and Campbell [62].

The resulting sample is a 50 nm (measured with the log-ratio method described in [1]) thin polycrystalline film with around 50 nm grain size (Figure 3.11). It was observed that locally, most of the grains are [001] oriented, showing that the sputtering conditions are such as the film growing is almost epitaxial. The storage of the sample can be done in a medium vacuum (about $5 \cdot 10^{-2}$ Torr), ideally desiccated.

Furthermore, the specimen prepared with this method are those that show the smallest contamination.

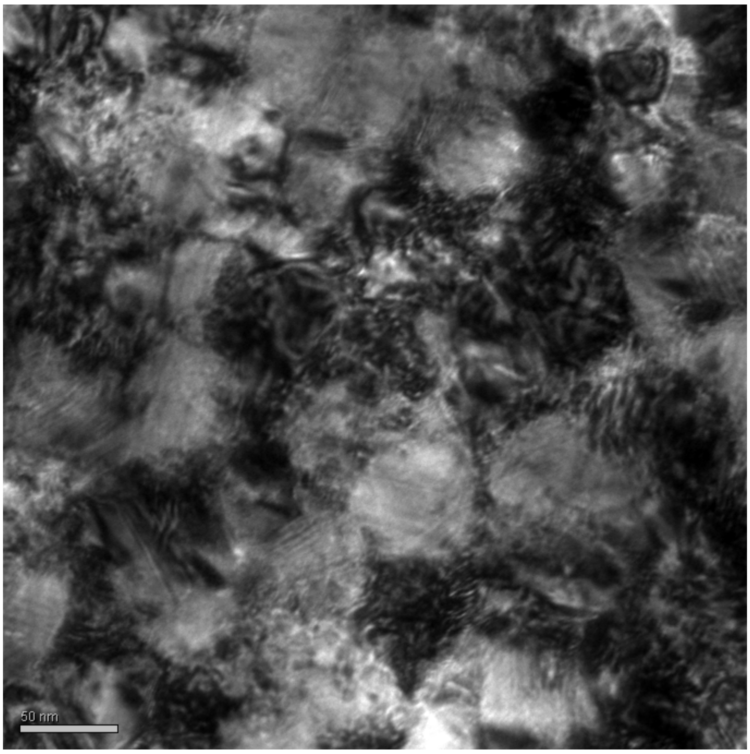

Figure 3.11: TEM image of a silver film prepared with the sputtering method.

4 Theory

4.1 Electron scattering

When an electron beam is directed toward a specimen, different interactions are possible. A non-exhaustive list of phenomena encountered in electron microscopy is shown in Figure 4.1. TEM imaging usually makes use of the forward scattered electrons (after the specimen) and the direct beam. Nevertheless, using additional detection devices, it is also possible to detect the backscattered, secondary and Auger electrons, the X-rays (X-ray detector) and the visible light (cathodoluminescence). These later topics are not treated in this work.

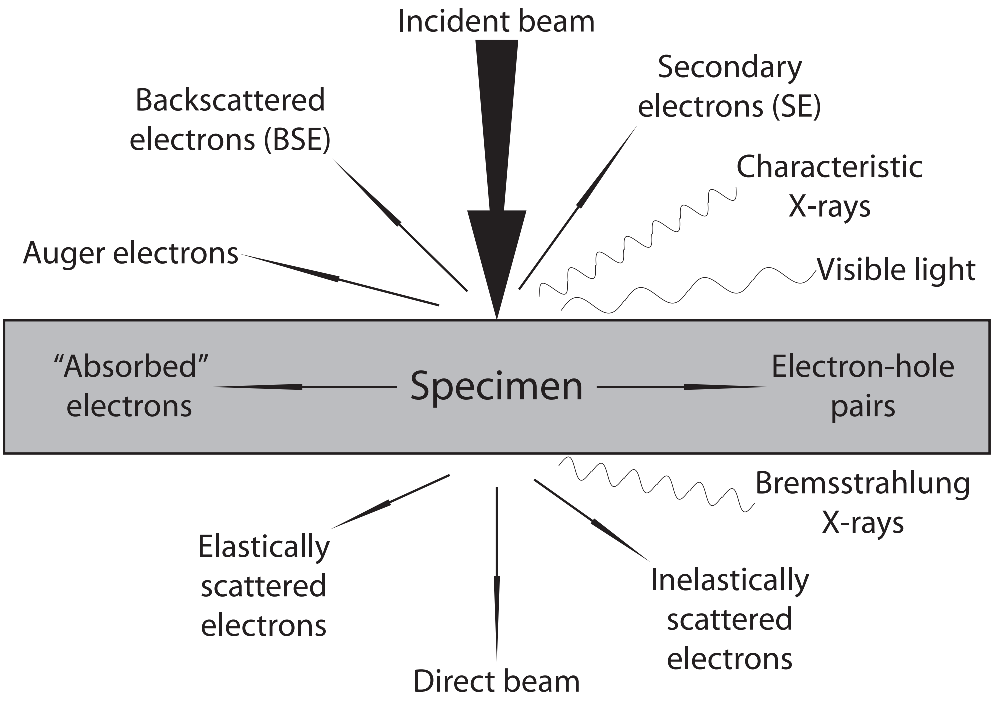

Figure 4.1: Possible interactions of the electron beam with a specimen.

Electron scattering is driven by Coulomb interaction: the incoming electron (from the incident beam) may interact with an electron or an ion of the specimen, elastically or inelastically. The probability of interaction is proportional to the scattering cross-section σ, which varies with the kind of interaction, the energy of the beam, the scattering angle and the incidence direction if the specimen is anisotropic. The scattering cross section depends strongly on the scattering angle, allowing to access angular information. This is given by the differential cross section $\frac{d\sigma}{d\Omega}$, where Ω is a solid angle, as shown in Figure 4.2.

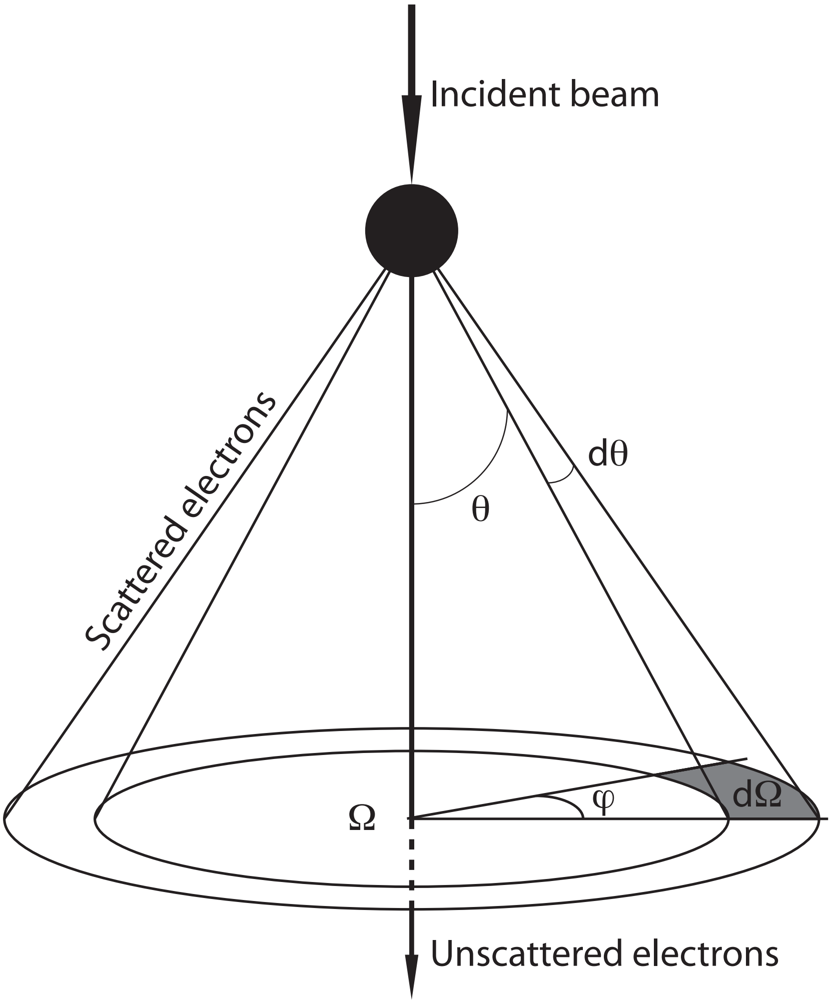

Figure 4.2: Electron scattering by a single atom. The electrons are scattered at an angle θ within a solid angle $d\Omega$.

Elastic scattering is basically a deviation of the incident electron. The deviation angle is determined by the atomic number Z of the scattering atom, the acceleration voltage of incident electron and the impact parameter. Constructive interferences will produce the bright spots of a diffraction pattern (an example of pattern being shown in Figure 4.3).

Inelastic scattering happens when the incident electron looses energy while interacting with the specimen. A momentum transfer happen between the electron and the specimen. The momentum transfer from the incident electron depends on the energy loss and thus on the interaction with the specimen, which can be plasmon excitation, inter-band or core-loss interaction and on the scattering angle. These interactions, analyzed in their energy distribution, lead to the so-called "EELS spectrum", an example being shown later in Figure 4.6.

This distinction between elastic and inelastic scattering arise from the fact that the system considered for the interaction is made of the probe electron and the specimen. Strictly speaking, the phonon losses (collective oscillation of the atoms of the specimen) are inelastic. However, since their energy loss is about some meV, which makes them undetectable by EELS, they are often called "quasi-elastic".

The whole theory about diffraction is well described *e.g.* in Williams and Carter's "Transmission Electron Microscopy" [40], so only the information about diffraction which is relevant for this work is mentioned hereafter.

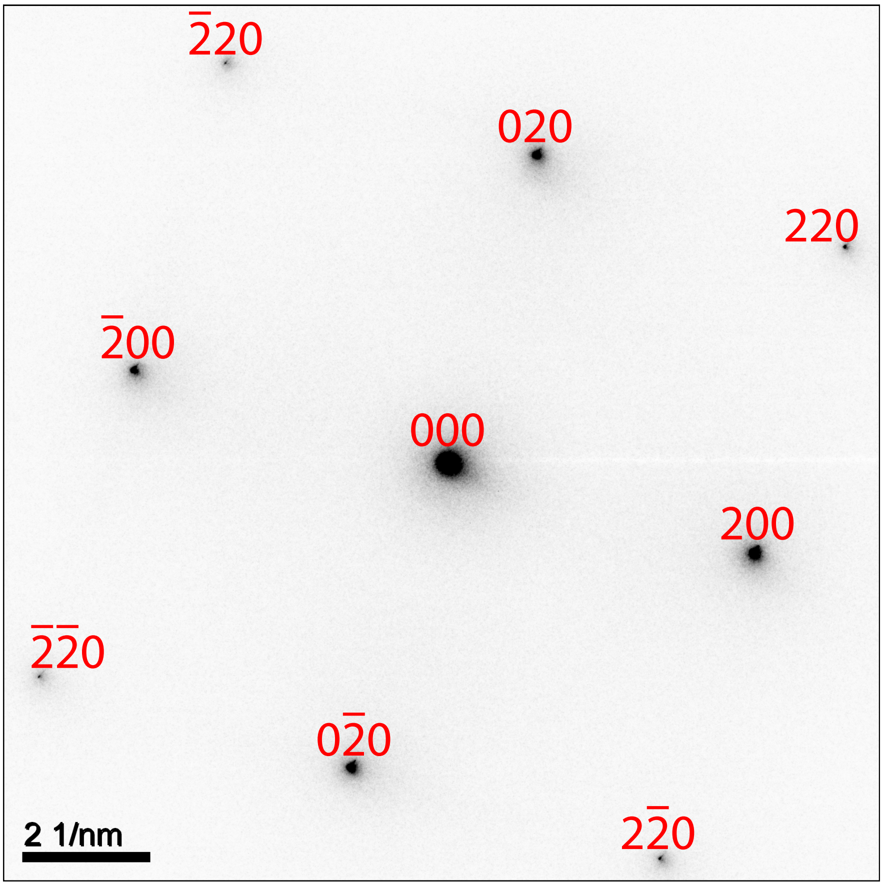

Figure 4.3: Silicon [001] diffraction pattern, camera length 60 cm. Gray scale is inverted for better contrast.

A diffraction pattern is characterized by a series of bright spots on a much less intense background which form a geometric figure – the pattern. It gives direct access to the crystallographic structure of the specimen.

The diffraction pattern is formed in the Back Focal Plane (BFP) of the objective lens. It corresponds to the intersection of the Ewald sphere with the reciprocal lattice. Thus, the reciprocal space is directly accessible. The "distances" in this space are measured in inverted length (in this work, with units of nm^{-1}), although other notations are possible (Appendix B).

The spots – which are Airy disks [40] – arise when the condition for constructive interference, namely the Bragg conditions given by

$$\lambda = 2d_{hkl}\sin\theta_B \tag{4.1}$$

are fulfilled. Here, θ_B is the so-called Bragg angle of scattering, λ the wave length and d_{hkl} distance between lattice planes of the specimen. The spots are identified with help of the so-called Miller indices [40]. The convention in crystallography is that the diffraction spot from a specific (hkl) plan is denoted hkl, where the 000 spot is the transmitted beam. The zone axis, noted $[UVW]$, is the direction of the incident beam and is perpendicular to the normal of all (hkl) planes of the zero order Laue zone.

As mentioned in section 2.1.1, the "magnification" of the pattern depends on the selected Camera Length (CL): the higher the CL, the larger the projected diffraction pattern.

Due to the geometric setup (Figure 4.4), the relation

$$\frac{R}{L} = \tan 2\theta_B \approx 2\theta_B \tag{4.2}$$

holds, where R is the measured distance on the screen, L the camera length and $2\theta_B$ the angle between the transmitted and a diffracted spot. The approximation $\tan 2\theta \approx 2\theta$ is possible since angles are not larger than 100 mrad in a TEM [1]. Using the Bragg equation (4.1), the relation between R, L, the reflecting plane distance d_{hkl} and the wavelength becomes:

$$Rd_{hkl} = \lambda L \tag{4.3}$$

Thus, knowing the acceleration voltage of the beam and the camera length, it is easily possible to retrieve the reflecting plane distance d_{hkl} of the specimen by measuring the distance of a diffraction spot with respect to the transmitted beam. And knowing the crystalline structure of the materials (thus d_{hkl}) allows to precisely calibrate an arbitrary scattering angle θ at which an EELS measurement is done.

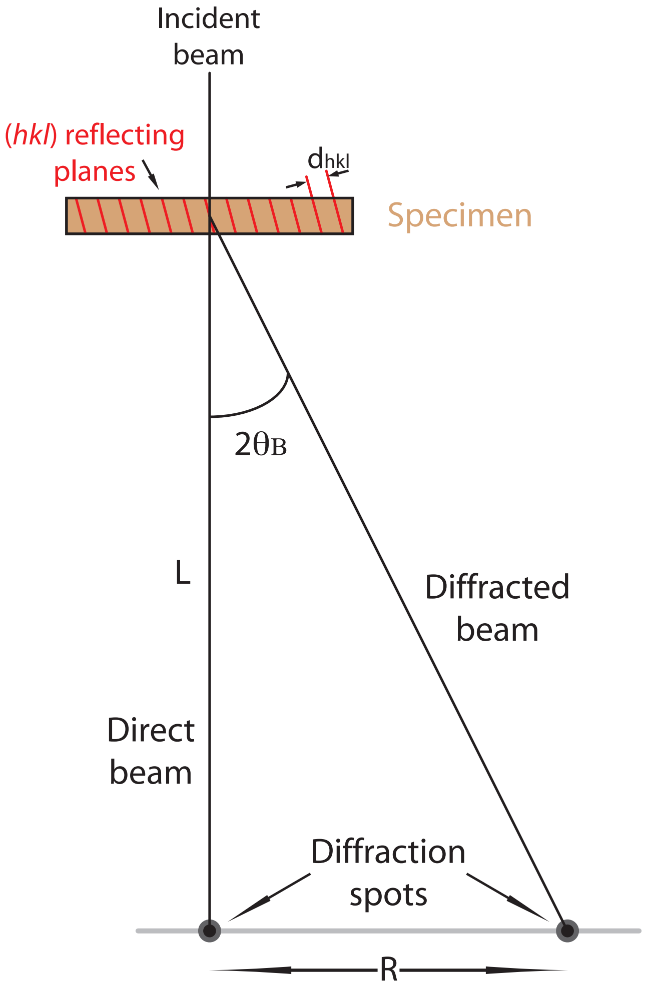

Figure 4.4: The camera length L is defined as the virtual distance between the specimen and the projection screen (or entrance of the acquisition device). The transmitted and diffracted spots are separated by $R \approx 2L\theta_B$. In TEM, L is changed by varying the excitation of the projector lens system.

4.2 Electron Energy Loss Spectrometry (EELS)

A comprehensive description of EELS can be found *e.g.* in Egerton's "*Electron Energy Loss Spectroscopy in the Electron Microscope*" [1].

As the acronym suggests, an EELS spectrum shows the number of electrons which have lost a certain amount of energy while interacting with the specimen, as sketched in Figure 4.5. An example of EELS spectrum is shown in Figure 4.6. The major features visible in such a spectrum are:

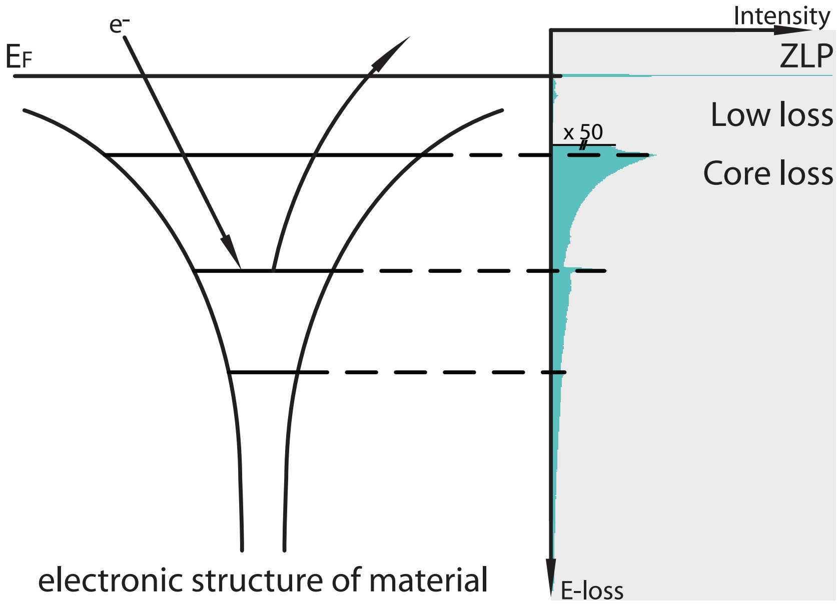

Figure 4.5: Schematic representation of the origin of the EELS spectrum when electrons interact with matter.

The Zero-Loss Peak (ZLP). For thin TEM lamella, this is the most intense peak. It corresponds to the electrons which have not lost energy, meaning that they have only undergone elastic scattering. It's shape may be approximated by a gaussian because of the finite energy resolution of the instruments. The ZLP allows to precisely set the zero of the EELS spectrum, and its Full Width at Half Maximum (FWHM) gives the energy resolution of the spectrum. The broadening of the ZLP comes from the intrinsic energy width of the emission, the instability of the high tension and the instabilities of the lenses that cause the ZLP to move, as well as the projector lens aberrations and the image/diffraction coupling in the spectrometer.

Several small peaks. They correspond to plasmon excitation (collective oscillations of the free electron gas), inter-band transitions and transitions from the valence band to an unoccupied state in the transition band (see Figure 4.5). The region where they occur is called the "low-loss region", since the amount of energy lost is about some tenth of eV. These inter-band transitions and plasmon features allow to characterize the specimen (*e.g.* [63]).

Sharp or smooth edges. These edges correspond to electrons which interact with core shell electrons of the atoms of the specimen. These edges arise at the energies of the binding energy of the core electrons to their nucleus, thus allowing a chemical analysis of the specimen. A deeper analysis of these features even allow an analysis of the electronic structure, which is one of the research topics of ELNES (Energy Loss Near Edge Structures). The theory of ELNES may be found in *e.g.* [64] whereas possible applications are shown in [1].

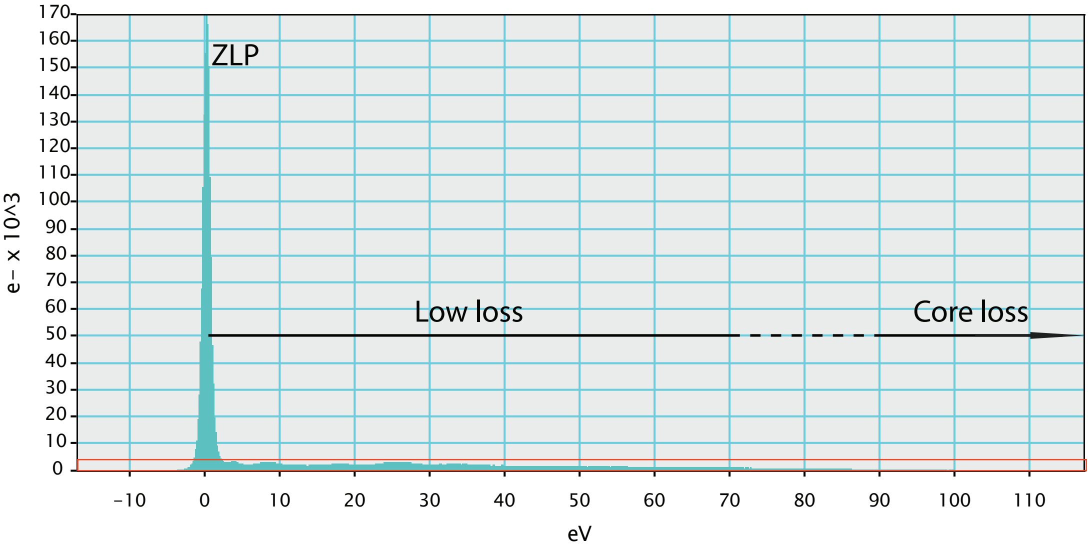

(a) Unscaled EELS spectrum

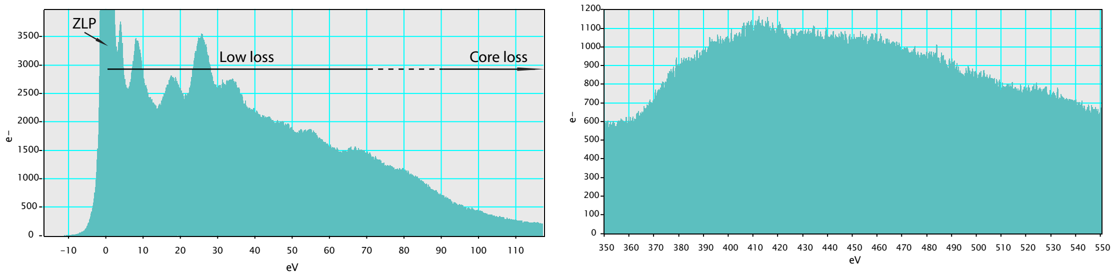

(b) EELS spectrum: low loss

(c) EELS spectrum: core loss

Figure 4.6: Example of an EELS spectrum. (a) shows an unscaled spectrum of silver with the full height of the ZLP. In thin specimens, the zero loss peak is over 100 times more intense than plasmons or edges. (b) zooms into the red rectangle of (a), showing the low loss region and its features. (c) shows the Pd M_{45} edge at 335 eV.

4.3 Angular resolved EELS

Angular resolved EELS is a special technique of EELS where not only the energy loss is taken into consideration, but also the scattering angle of the electrons. Indeed, taking into account the scattering angle, it is possible to retrieve the double differential scattering probability, described by Ritchie in 1957 [1,37] without relativistic or surface effects:

$$\frac{\partial^2 P}{\partial\omega\partial\Omega}(\omega,\boldsymbol{q}) \propto \frac{e^2}{\pi^2\hbar v^2}\Im\left(\frac{1}{\varepsilon(\omega,\boldsymbol{q})}\right) \tag{4.4}$$

which is proportional to the imaginary part of the inverse dielectric function ε, where ω is the excitation frequency and $\boldsymbol{q}$ the momentum transfer. Using a Kramers-Kronig Analysis (KKA), it is thus in theory possible to obtain the dielectric function of a sample on a practical way. Ignoring a scaling parameter gives the relation

$$P(\omega,\boldsymbol{q}) \propto \Im\left(-\frac{1}{\varepsilon(\omega,\boldsymbol{q})}\right)\frac{1}{\theta^2+\theta_E^2} \tag{4.5}$$

where P is the loss probability, θ the scattering angle and θ_E the characteristic angle for the energy loss ΔE, related to the excitation frequency ω by $\Delta E = \hbar\omega$. This characteristic angle is directly linked to the energy loss since $k\theta_E$ corresponds to the shortening of the scattered wave vector $\boldsymbol{k}'$, where $\boldsymbol{k}$ is the wave vector of the incident beam (Figure 4.7). It is given by $\theta_E = \frac{\Delta E}{2m_0\gamma v}$ where m_0 is the rest mass of the electron, v the absolute speed of the electrons in the beam and γ the relativistic factor $\gamma = \frac{1}{\sqrt{1+\frac{v^2}{c^2}}}$. It may be approximated by the energy loss over twice the energy of the incident beam $\theta_E \approx \frac{\Delta E}{2E_0}$.

The scattering angle is linked to the momentum transfer $\boldsymbol{q}$ by

$$q^2 = k^2(\theta^2+\theta_E^2) \tag{4.6}$$

This relation is possible since θ is extremely small so the small angle approximation holds.

Note: the expression "angular" comes from the link between the scattering angle and the perpendicular component of the momentum transfer $q_\perp$, as shown in Figure 4.7. Angular resolved EELS is commonly abbreviated q-EELS, but may also (rarely) be found as AREELS (*e.g.* [19]).

The advantage of EELS over optical measurements is that in EELS, the momentum transfer $\boldsymbol{q}$ and the energy loss ΔE may be tuned independently, while in optical absorption, they are linked, limiting this technique to very small q (often taken as 0).

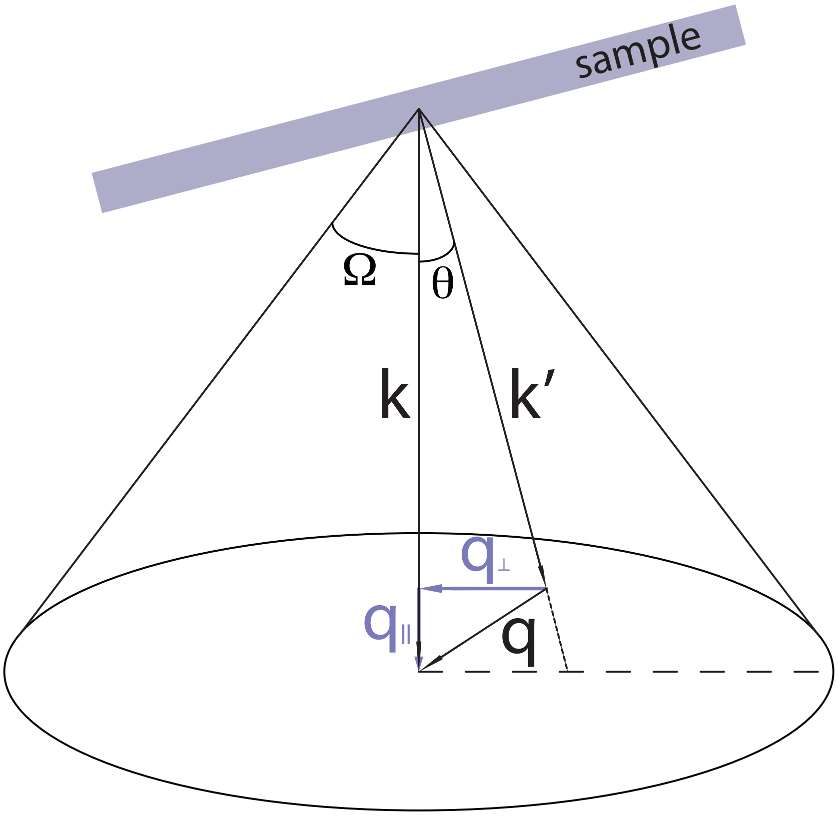

Figure 4.7: Schematic draw of angular resolved EELS. Given an angle θ and $q_{\parallel}$, it is possible to retrieve the momentum transfer $q_{\perp}$, since the wave number of the incident beam k is known.

4.4 Energy Filtered TEM (EFTEM)

The acronym EFTEM stands for Energy Filtered Transmission Electron Microscopy and describes a TEM acquisition method. It is only possible to do EFTEM if an energy filter is available in the TEM column (explained in section 2.2.2) or after the TEM column (such as GIFs [65]). The method has first been proposed by Jeanguillaume and Colliex [66], and consists in acquiring a single image or a set of images/diffraction pattern of the same region of interest, where each image/pattern, in this context called "slice", is taken at a different energy loss. These slices are then put together in order to form a 3D data cube called "EFTEM stack", as sketched in Figure 4.8. EELS spectra can then be produced by analyzing the data cube in the energy direction. A particular application of this technique is plasmon analysis. Indeed, if a sharp plasmon resonance energy is selected, the positions of the specimen that experience this loss "lights up" in the image [67].

It is obvious that the stack shown in Figure 4.8 is an ideal case. Due to high voltage instabilities in the gun, spatial drift of the specimen, remaining non-isochromaticity and other effects, the data cube is distorted and cannot be used just by stacking the slices one over the other, but has to be re-aligned. Schaffer *et al.* propose a way to do this data processing [68].

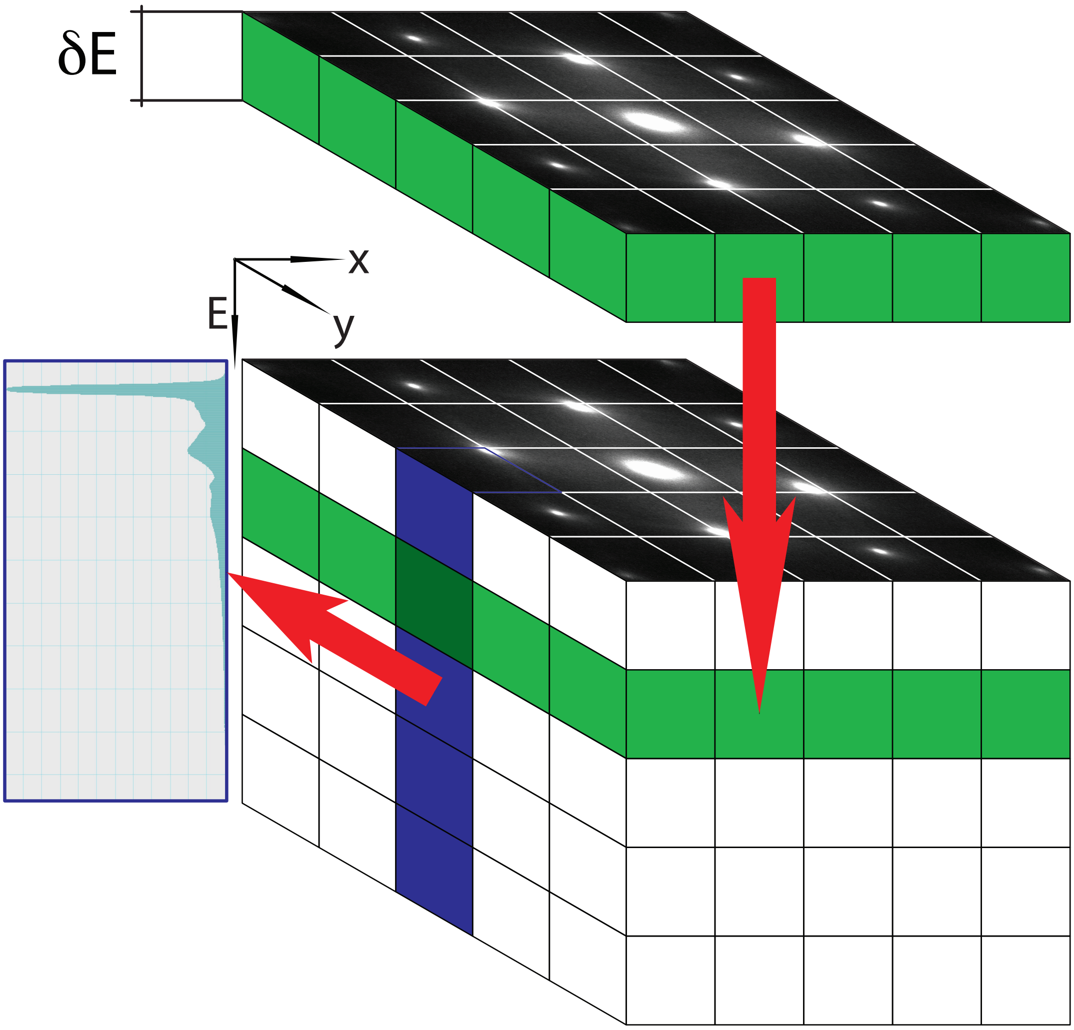

Figure 4.8: Combination of filtered slices (green) to an EFTEM stack and possible extraction of an EELS spectrum (blue). The resolution of the spectrum is modulated by the shift of the energy selecting slit, the slit width δE and the intrinsic resolution of the instrument.

The advantage of this technique is the very good spatial resolution in each slice (the spatial resolution of the EFTEM data cube), given by the spatial (x, y) resolution of the microscope. If a diffraction pattern is acquired, the technique allows very good angular resolution. The drawback is a limited resolution in energy that transfers to the extracted EELS spectra. The energy resolution is given by the shift of the energy selecting slit after the filter as well as the slit width δE and the intrinsic resolution of the instrument. Nevertheless, the best energy resolution reachable with EFTEM nowadays is about 0.1–0.2 eV [69] when using a monochromated microscope and a specially designed filter.

EFTEM was originally developed as a technique for chemical analysis. Therefore, it is mainly used in image mode, using core losses. In this work, EFTEM is used in diffraction mode. Figure 4.9 illustrates the relationship between $\boldsymbol{q}$, θ and θ_E as given in equation (4.6) in an EFTEM stack acquired in diffraction. From a geometric consideration, and knowing that θ is extremely small (maximum 100 mrad) so the small angle approximation $\sin\theta \approx \theta$ holds, the perpendicular component of the momentum transfer is given by $q_\perp = k\theta$ and the parallel component is linked to the energy loss by $q_\parallel = k\theta_E$.

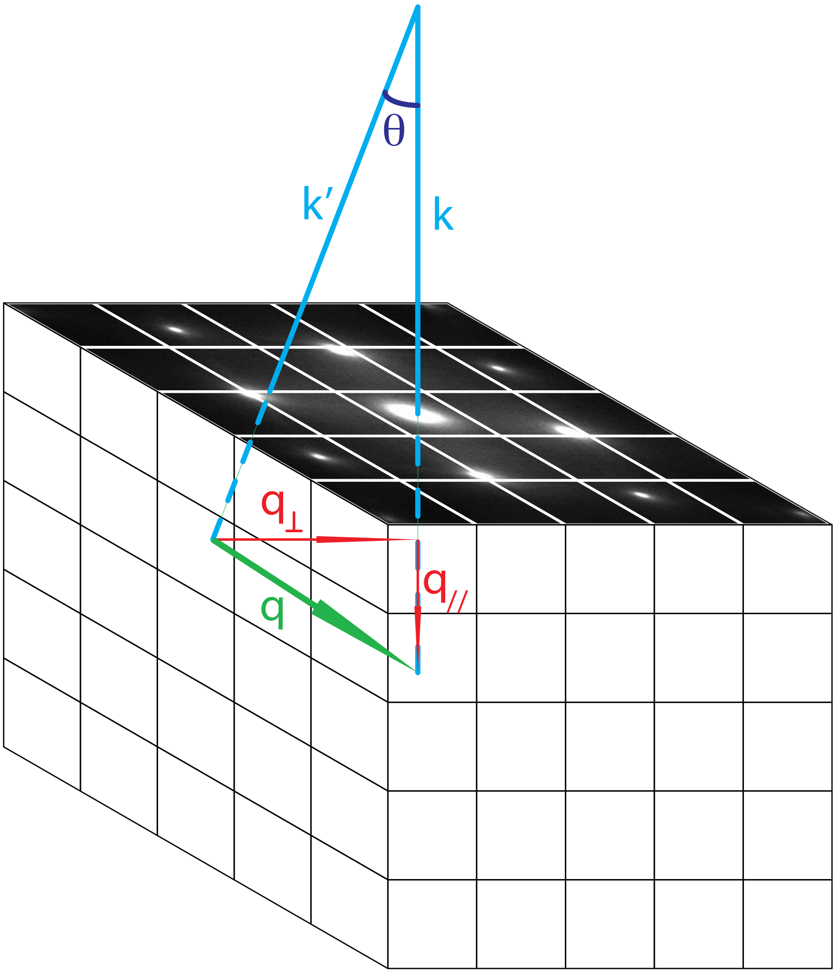

Figure 4.9: Visualization of the relationship between $\boldsymbol{q}$, $q_\perp = k\theta$ and $q_\parallel = k\theta_E$ as given in equation (4.6). The total momentum transfer $\boldsymbol{q}$ (green) is in relation with the angular momentum $q_\perp$ and the energy loss momentum $q_\parallel$ (both in red) by the Pythagoras theorem and $q_\perp$ is determined by the incident beam wave number k (cyan) and the scattering angle θ (in blue, defined as the angle between the incident and the diffracted beam $\boldsymbol{k}$ and $\boldsymbol{k}'$ respectively).

4.5 Theoretical computation

The single scattering distribution (which may be determined experimentally via the momentum transfer resolved energy loss function) allows in principle to retrieve the real and imaginary part (ε_1 and ε_2 respectively) of the dielectric function $\varepsilon(\omega)$ via a Kramers-Kronig Analysis (KKA) [1]. However, this retrieval is impossible when relativistic or surface effects come into play. On the other hand, if the band structure of the analysed material is known (which is the case for the noble bulk metal silver), it is possible to perform *ab initio* calculations of the loss function. By doing so, the accuracy of the calculation model may be verified by comparison with experimental results. This comparison is made in chapter 6.

The imaginary part of the dielectric function $\Im\left[-\frac{1}{\varepsilon(\omega,\boldsymbol{Q})}\right]$ is linked to the dynamic structure factor $s(\omega,\boldsymbol{Q})$ via

$$s(\omega,\boldsymbol{Q}) = \frac{2}{v(\boldsymbol{Q})}\Im\left[-\frac{1}{\varepsilon(\omega,\boldsymbol{Q})}\right] \tag{4.7}$$

where $\boldsymbol{Q}$ is the momentum transfer and $v(\boldsymbol{Q}) = \frac{4\pi}{Q^2}$ is the Fourier transform of the Coulomb interaction.

Since the quantum-mechanical electron density fluctuations of the physical system described by the dynamic structure factor [70] is directly related to the macroscopic density response function χ_M by

$$s(\omega,\boldsymbol{Q}) = -2\,\Im\left(\chi_\mathrm{M}(\omega,\boldsymbol{Q})\right) \tag{4.8}$$

the main quantity that needs to be calculated is χ_M. This macroscopic quantity is related to its microscopic counterpart $\chi_{\boldsymbol{G},\boldsymbol{G}'}(\omega,\boldsymbol{q})$ via [71]

$$\chi_\mathrm{M}(\omega,\boldsymbol{Q}) = \chi_{\boldsymbol{G},\boldsymbol{G}}(\omega,\boldsymbol{q}) \tag{4.9}$$

where $\boldsymbol{G}$ is the reciprocal lattice vector, and $\boldsymbol{Q} = \boldsymbol{q}+\boldsymbol{G}$, so that $\boldsymbol{q}$ is confined to the first Brillouin zone. Within the linear-response formulation of the Time-Dependent Density Functional Theory (TDDFT) [72, 73], the microscopic density-response function χ of the interacting many-electron system is related to the density-response function χ^0 of the corresponding non-interacting Kohn-Sham system through the Dyson equation, which is, symbolically:

$$\chi = \chi^0 + \chi^0(v + f_\mathrm{XC})\chi \tag{4.10}$$

where f_XC is the exchange-correlation kernel that accounts for all many-body effects, and χ^0 is given as

$$\chi^0_{\boldsymbol{G},\boldsymbol{G}'}(\omega,\boldsymbol{q}) = \frac{2}{\Omega_0}\sum_{\boldsymbol{k}}^{\mathrm{BZ}}\sum_{n,n'}\frac{f_{n,\boldsymbol{k}} - f_{n',\boldsymbol{k}+\boldsymbol{q}}}{\varepsilon_{n,\boldsymbol{k}} - \varepsilon_{n',\boldsymbol{k}+\boldsymbol{q}} + \omega + i\eta} \times \langle\psi_{n,\boldsymbol{k}}|e^{-i(\boldsymbol{q}+\boldsymbol{G})\cdot\boldsymbol{r}}|\psi_{n',\boldsymbol{k}+\boldsymbol{q}}\rangle\langle\psi_{n',\boldsymbol{k}+\boldsymbol{q}}|e^{i(\boldsymbol{q}+\boldsymbol{G}')\cdot\boldsymbol{r}}|\psi_{n,\boldsymbol{k}}\rangle \tag{4.11}$$

Here, $\psi_{n,\boldsymbol{k}}$, $E_{n,\boldsymbol{k}}$, $f_{n,\boldsymbol{k}}$ are single-particle wave functions, their eigenvalues, and occupation numbers, respectively; Ω_0 is the volume of the unit cell. While the approach is formally exact, approximations are needed in practice [73]. In this work, two different simple approximations are used. Setting f_{XC} to 0 yields the Random-Phase Approximation (RPA), in which only the classical Coulomb field of the induced charge density is accounted for when calculating χ. The second approximation is the Adiabatic Local Density Approximation (ALDA or TDLDA), in which f_{XC} is given by [73]

$$f^{\mathrm{TDLDA}}_{\mathrm{XC}}(\boldsymbol{r}t,\boldsymbol{r}'t') = \delta(t-t')\delta(\boldsymbol{r}_1-\boldsymbol{r}_2)\left.\frac{dV^{\mathrm{LDA}}_{\mathrm{XC}}(n)}{dn}\right|_{n=n(\boldsymbol{r},t)} \tag{4.12}$$

The TDLDA kernel is local in space and time. Thus, its Fourier transform in time is frequency-independent, and the transform in real space, $f^{\mathrm{TFLDA}}_{\boldsymbol{G},\boldsymbol{G}'}(\boldsymbol{q})$, depends only on $\boldsymbol{q}$ and $\boldsymbol{G}-\boldsymbol{G}'$.

An important concept in studying response functions is that of crystal local fields. Taking the RPA as an example, one obtains from equation (4.10):

$$\chi = \left(1-\chi^0 v\right)^{-1}\chi^0 \tag{4.13}$$

The calculation of χ therefore involves the inversion of the matrix $1-\chi^0 v$ for each value of $\boldsymbol{q}$ and ω. Calculations are numerically involved as one needs to include a sufficient set of reciprocal lattice vectors for the representation of microscopic quantities, so that the final result is converged. Neglecting all off-diagonal elements, or crystal local fields, is equivalent to dealing with scalar functions rather than matrices. This is equivalent to the assumption that the screening charge is independent of the position of the test charge inside the unit cell. The comparison of response functions calculated with or without the inclusion of local fields shows to what extent this assumption is realistic in a given material. Figure 4.10 shows the computation of the loss function of silver in both cases with and without Local Filed Effects (LFE). The difference of the two cases is evident and leads to the conclusion that the LFE cannot be neglected above 30 eV for the calculation of the loss function of silver.

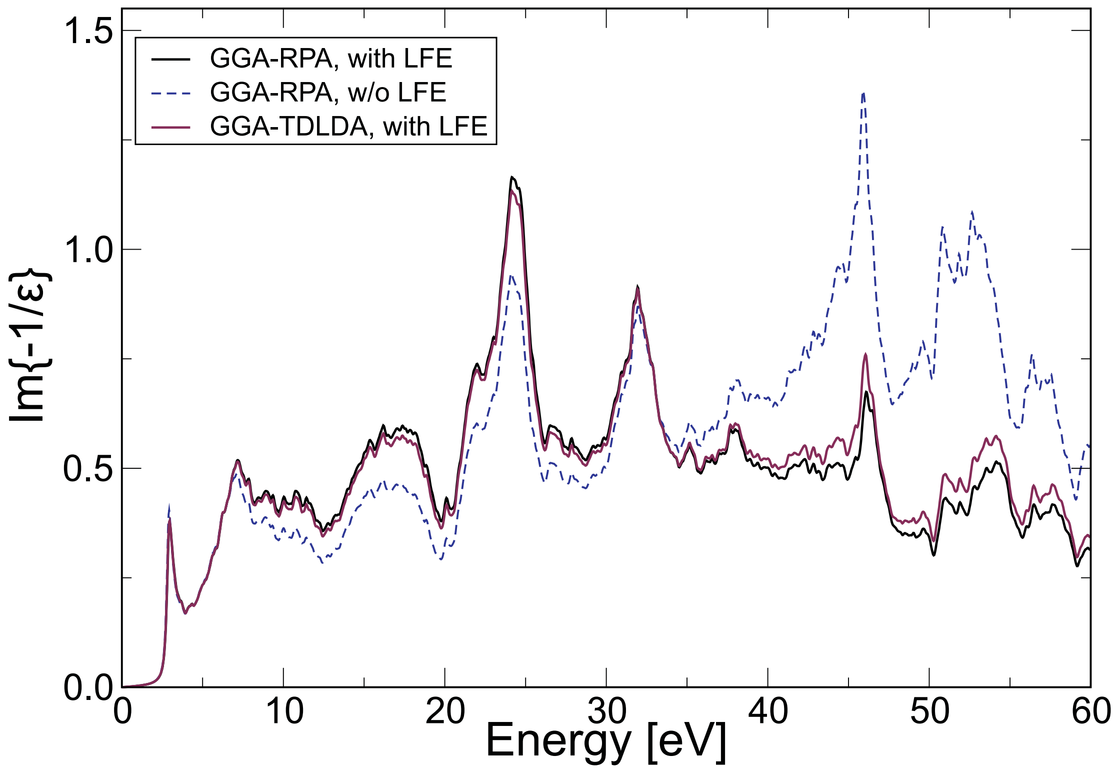

Figure 4.10: Loss function of silver calculated with (solid lines) and without (dashed line) consideration of the local field effects. The difference is evident and leads to the conclusion that LFE are necessary for this computation.

4.6 Dynamics

The dynamic range refers to the capacity of an acquisition device to detect very strong and very weak signals in the same image. It is defined as the ratio of the maximum number of electrons needed to saturate a pixel, divided by the intrinsic read noise.

According to the manufacturer, the Gatan camera installed on the JEOL has a full 16 bits dynamic range. However, the data acquired in the frame of this work and presented in chapter 6 need a dynamic range of almost 20 bits. This value has been determined as sketched in Figure 4.11 on an experimental stack: an integration box of 0.1 $\mathrm{nm}^{-1} \times 0.1\ \mathrm{nm}^{-1} \times 3$ eV is created over the transmitted beam at $\boldsymbol{q} = \mathbf{0}$ and at a place where the signal is weak at $\boldsymbol{q} \neq \mathbf{0}$ of the EFTEM data cube respectively. The ratio of the integrated intensities within the two boxes gives the dynamic range. In practice, the two spectra on the right hand side of Figure 4.11 are extracted from the EFTEM data cube via an integration surface of 0.1 $\mathrm{nm}^{-1} \times 0.1\ \mathrm{nm}^{-1}$ over the full energy range. The integration window of 3 eV is selected afterwards on the spectra: on the ZLP in the $\boldsymbol{q} = \mathbf{0}$ spectrum and on a place with weak energy loss for the $\boldsymbol{q} \neq \mathbf{0}$ spectrum.

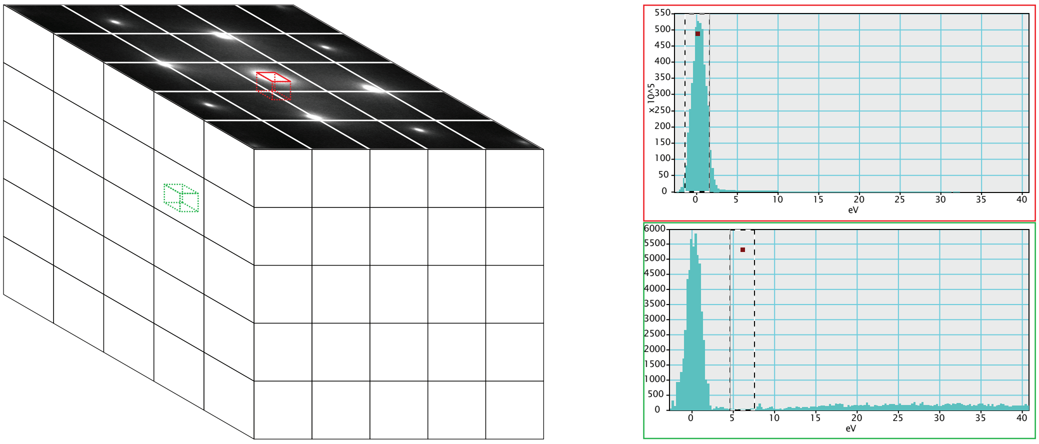

Figure 4.11: Determination of the dynamic range needed: the red integration box corresponds to the brightest part of the EFTEM stack, and the green integration box is at a place with weak energy loss. The ratio of the integration value of the two boxes gives an estimation of the requested dynamic. The picture on the right hand side shows the spectra integrated over a surface of $0.1 \times 0.1\ \mathrm{nm}^{-1}$ along the energy axis on the transmitted beam (upper panel; $\boldsymbol{q} = \mathbf{0}$) and on a place with weak signal at $\boldsymbol{q} \neq \mathbf{0}$ in the diffraction pattern (lower panel) respectively. The integration window of 3 eV is represented in each spectrum.

4.7 Resolutions

While doing angular resolved EELS, three resolutions determine the quality of the data [74]:

- spatial resolution;
- angular resolution;
- energy resolution.

Commonly, spatial resolution describes the capacity of an image-forming device (*e.g.* a microscope, a camera, a telescope) to distinguish small details of an object. However, in the context of angular resolved EELS, the spatial resolution is given by the size of the illuminated area, which is the size of the probe on the specimen. In the frame of this work, the illumination has to be parallel and the illuminated area as small as possible. A compromise to fulfill as much as possible those two contradictory requirements was found in the use of the NBD mode.

The angular resolution determines the smallest perpendicular angular momentum transfer $\boldsymbol{q}_\perp$ detectable. This momentum transfer is directly measurable in a diffraction pattern, which makes the diffraction mode convenient for angular resolved EELS measurements. The sharpness of the details in the diffraction pattern are driven by the camera length, the binning during the acquisition and the parallelism of the incident beam. Ideally, the diffraction spots are point sources. However, a remaining beam convergence (the incident beam on the specimen is never perfectly parallel), as well as the spherical and chromatic aberrations of the lenses [40] induce a broadening, making the diffraction spots appear as disks. The experimental angular resolution is given by the angular FWHM of the transmitted beam at 0 eV energy loss.

The energy resolution determines how faint details in the EELS spectra will be detected. In EFTEM, the energy resolution is given by the convolution of the size of the crossover before the filter entrance with the width δE of the energy selecting slit. Experimentally, the energy resolution is defined as the FWHM of the ZLP of the transmitted beam ($\boldsymbol{q} = \boldsymbol{0}$).

The theoretically best possible resolutions on the JEOL 2200 FS at CIME are given in Table 4.1.

Table 4.1: Theoretical best resolutions of the JEOL at CIME

Resolution	**value**	**condition**	**issue**
Spatial	50 nm	CLA4	S/N ratio
Angular	4 μrad	CL = 250 cm @ bin1	orientation, oversampling
Energy	0.8 eV	optimal alignment	intrinsic limit

The main issues working at these resolutions are the following:

Spatial resolution In the frame of this work, a spatial resolution of 50 nm is only achieved by using a CLA4 in NBD mode. Since the CLA4 is tiny (10 μm in diameter according to JEOL), only a small part of the source current is used, and the signal to noise ratio is lowered to a point of non-usability of the microscope. Therefore, CLA3 with a diameter of 40 μm was used, giving a lateral resolution about 220 nm.

Angular resolution 250 cm is the highest possible camera length of the microscope. However, if it is used to image the transmitted beam, the diffraction spots are out of the field of view and the orientation is therefore lost. Furthermore, due to the intrinsic limit of the angular resolution, one may just be oversampling. Since the first diffraction spots are in the field of view at a camera length of 80 cm (or lower), this setting is used in the present work.

Energy resolution Using an energy selecting slit width smaller than $\delta E = 0.5$ eV may give rise to edge effects and other aberrations. Furthermore, such a small slit width do not improve the accuracy of the information since the Schottky FEG limits the intrinsic energy resolution of the microscope to 0.8 eV. To improve this value, a monochromator would be mandatory.

5 Energy Filtered Nano-Beam Electron Diffraction (EFNBED)

The data acquisition technique presented in this work is called Energy Filtered Nano-Beam Electron Diffraction (acronym EFNBED), since it combines energy filtered diffraction (diffraction EFTEM) with the nano-beam illumination mode. EFTEM is provided by the in-column Ω filter and allows the acquisition of a whole data set from which the angular resolved EELS information can be extracted. The NBD mode is used for parallel illumination on a small area with much higher intensity than the TEM or SAED mode.

5.1 Microscope alignment

First of all, it is necessary to align the microscope in order to get a parallel illumination in the nano-beam mode, which is not the standard operation. Indeed, parallel illumination is mandatory to guarantee the angular resolution, which would otherwise be blurred by convolution with the convergence angle. At this point, it is important to mention that a perfect parallel illumination on the specimen is *ipso facto* impossible, since the electrons of the beam follow a helical trajectory relative to the optical axis [75, 76] (one should thus write "almost parallel illumination", with quote marks).

To manage a parallel illumination in nano-beam diffraction mode, the microscope is first aligned in TEM mode with parallel illumination. An alignment procedure may be found in Appendix C. Once the microscope is aligned in TEM mode, it is put in NBD mode and the desired CLA inserted. At this step, the bright tilt has to be corrected again, since the behavior of the condenser lenses is changed in NBD mode. To get a parallel illumination, the diffraction spots have to be made as small as possible in diffraction mode by changing the probe size. Here, the following assumption is made: if the diffraction spots are the smallest in TEM mode and the diffraction focus is not modified, then the previous alignment is kept and the projector lens system images the back focal plane of the objective lens. Thus, the diffraction spots should be the smallest with the same diffraction focus when the illumination is parallel also in NBD mode for the same reason. A practical way to verify the parallelism of the illumination is to change the focus of the objective lens: if the size of the illuminated area on the screen does not change, one can be sure that the illumination is "parallel". Then focusing the diffraction pattern with the intermediate lenses (IL) will image the BFP of the objective lens.

At this point, it is important to mention that the spectrum alignment is done with a FL energy offset of 5 eV for the EFNBED method. Indeed, the EFTEM acquisition routine in DigitalMicrograph does not allow to start at negative energy values. Aligning the spectrum at 5 eV and starting the EFTEM acquisition at 0 eV gives access to the negative tail of the ZLP, which will be important for the Batson correction. There are two possibilities to generate an energy offset: either with the acceleration voltage of the gun (HT) or with the excitation of the filter lens (FL). The last one is preferred for this work since it lets the specimen illumination by the condenser lens unchanged. This is also the reason why this energy shift method is used in STEM-EELS mode.

5.1.1 Major alignment issues using an Ω filter

Image-coupled diffraction pattern

As mentioned in section 2.2.2 and sketched in Figure 5.1, the spectrum of a diffraction pattern is image-coupled, and inversely the spectrum of an image is diffraction-coupled.

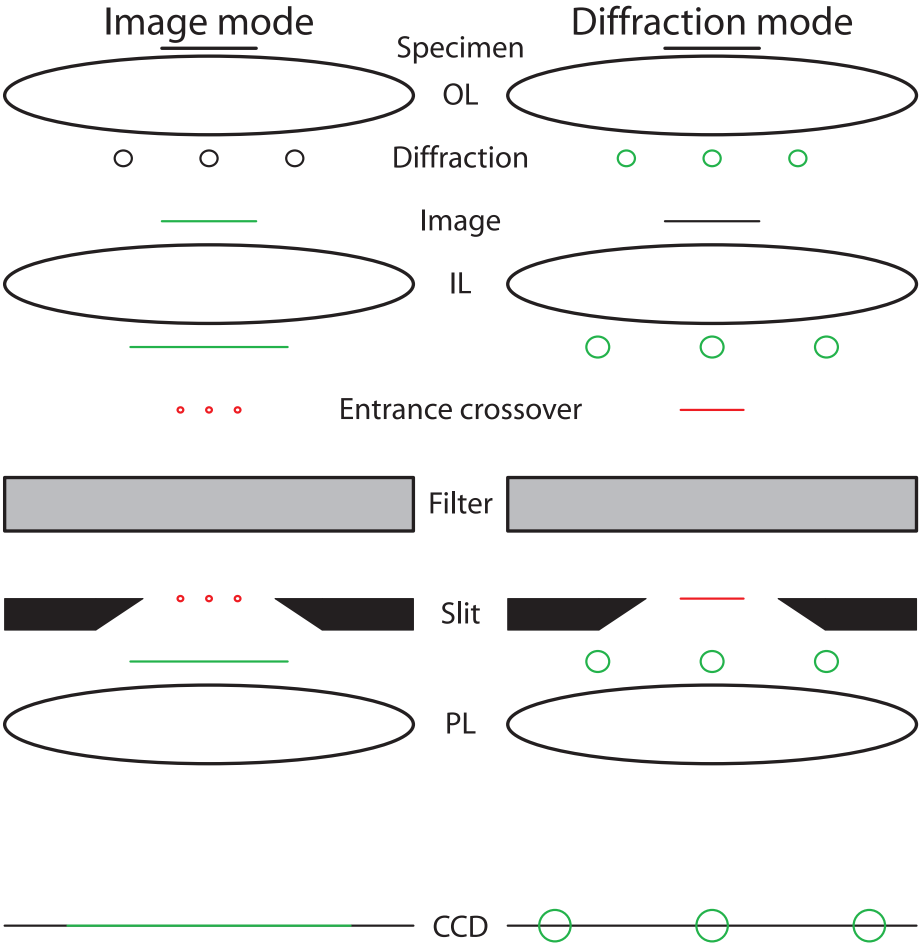

Figure 5.1: Coupling in image and diffraction mode: an inverse relation. In image mode (left hand side), a diffraction pattern is coupled with the spectrum at the energy slit and in diffraction mode (right hand side), an image is coupled with the spectrum at the energy slit. Since small magnifications/CL are used in EFTEM, large CL/magnification occur at the entrance window and the slit respectively.

Since the two crossovers before and after the filter are conjugated, the energy spectrum in the crossover after the Ω filter is convoluted with the object in the crossover before the filter. Thus, if the feature is close to a Dirac function (*e.g.* a diffraction spot, which is an Airy disk), the energy-loss spectrum will be convoluted with this sharp function, leading to the spectrum itself with almost the nominal resolution of the system. However, if the feature in the pre-filter crossover is a large image (not a point source), then the spectrum will be convoluted with that image and consequently broadened. To demonstrate this broadening, an example of a diffraction EELS spectrum taken with different selecting area apertures is shown in Figure 5.2.

This image-coupling is the main reason why it has been chosen to use the NBD mode for this work, although advantage of the NBD is taken to have high brightness. Figure 5.3 shows the absolute resolution and the relative resolution with respect to the SAA respectively for the TEM diffraction mode with the JEOL 2200 FS at CIME.

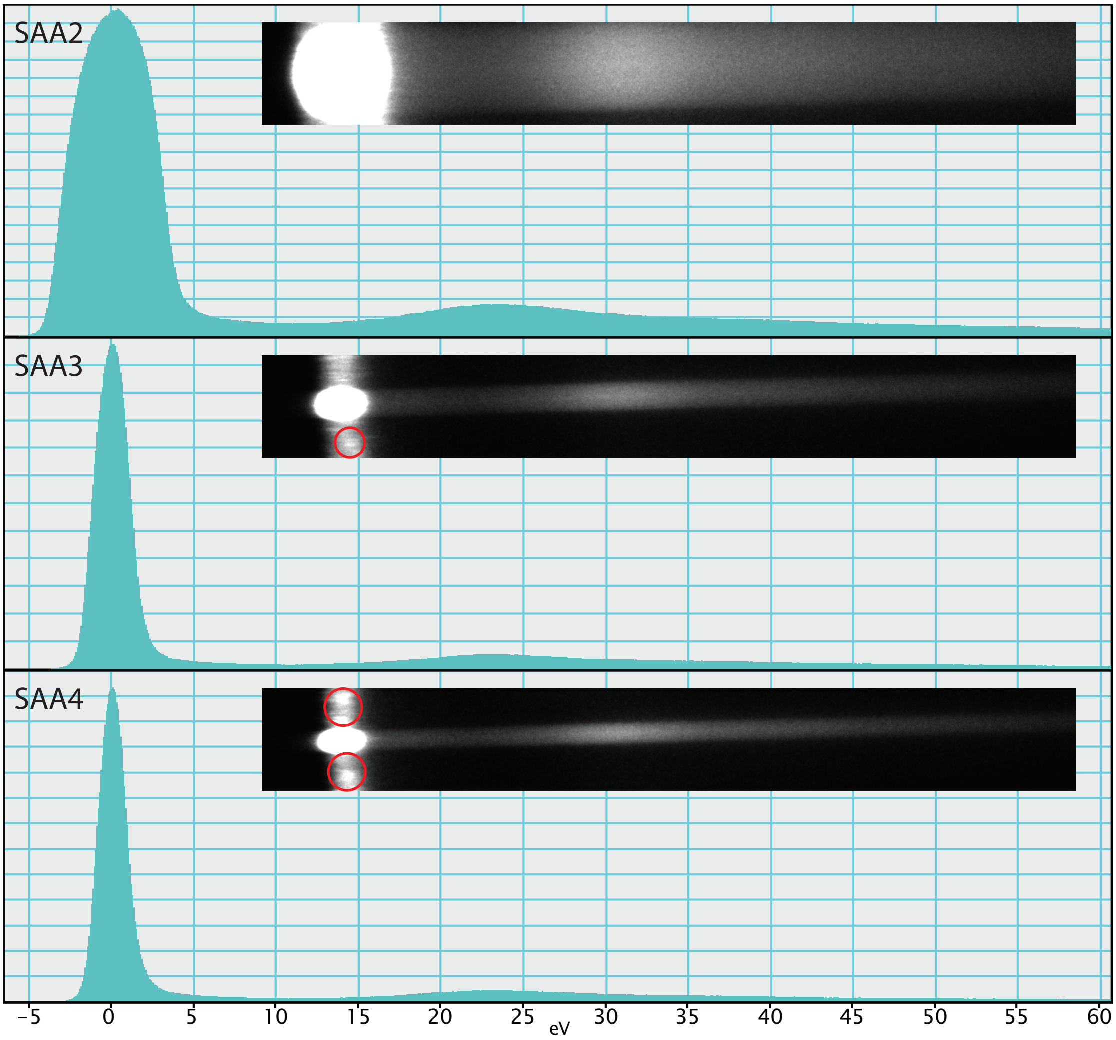

Figure 5.2: Example of image-coupling in diffraction EELS spectra using different selecting area apertures. The larger the aperture, the worse the resolution of the spectrum. The insets show the 2D spectrum in each case. The bright spot in the insets correspond to the convolution of the ZLP with the selecting area aperture. The bright features marked by the red circles are contribution from the diffraction rings of the polycrystalline NiO$_x$. SAA4 has a size of 225 nm, SAA3 a size of 360 nm and SAA2 a size of 800 nm back-projected on the specimen.

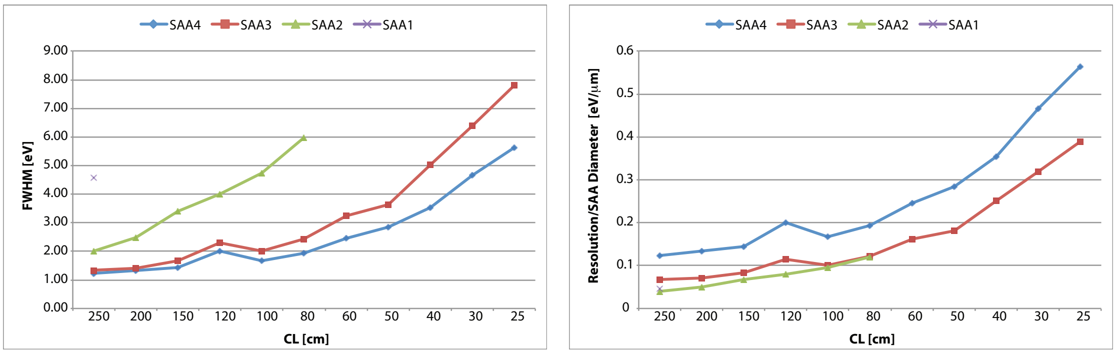

(a) Absolute resolution

(b) Relative resolution

Figure 5.3: Absolute resolution (a) and Relative resolution with respect to the selected SAA (b) of the JEOL 2200 FS at CIME in TEM diffraction mode, depending on the chosen camera length. The surprising behavior at 120 cm camera length is a factory misalignment. It has been corrected after this acquisition and certified satisfactory by JEOL.

Isochromaticity

Isochromatic stands for "of same color", meaning in the context of electron microscopy "of same energy". Non-isochromaticity is defined as the difference between the selected energy at the center of an image and that at outer regions [50]. Correcting the non-isochromaticity to a high level would need several sextupoles, which would drastically complicate the alignment of the Ω filter. Thus, a remaining non-isochromaticity is to be taken into account, even with an optimal filter alignment. In diffraction mode, this remaining non-isochromaticity may lie in a range as large as 1–20 eV, depending on the conditions of the intermediate lens system and the projector lens system.

In practice, non-isochromaticity is easily detected in image mode when the image in the filed of view changes in non-concentric circle shape if an energy-selecting slit is entered and slightly moved. This circles must be understood as follow: the "vacuum spectrum", namely the spectrum when there is no specimen and no other aperture than the CLA, shows like two nested cones joined at their top (Figure 5.4). The outer cone is wrapped with the "Zero Loss" plane and the inner cone is just a caustic that disappear when the object of the Ω filter is reduced (*e.g.* with an SAA as shown in Figure 5.5a or an ENTA aperture), or with a smaller illuminated region. In the normal case, an SAA slit is always inserted to remove the caustic, in order to get the EELS signal from the specimen. In diffraction mode, the behavior is not so easy to see. Indeed, instead of a nice ring, only the places where Bragg spots exist are visible, as shown later in Figure 5.7.

By changing the isochromaticity, which affects the $IL1$–4 lenses depending on the running mode of the microscope (see Table C.1 for detailed behavior), the position of the entrance crossover for the filter is modified, thus changing the shape of the cone at the hight of the slit, as shown in Figure 5.6. Figure 5.6b shows very well the distortion incurred by the zero loss cone (and accordingly the whole spectrum) when isochromaticity is not optimally aligned. Using a slit in this case selects different energies at the top and the bottom of the spectrum, leading to an energy shift in the EFTEM stack. Isochromaticity can only be adjusted when an energy slit is inserted, as demonstrated hereafter.

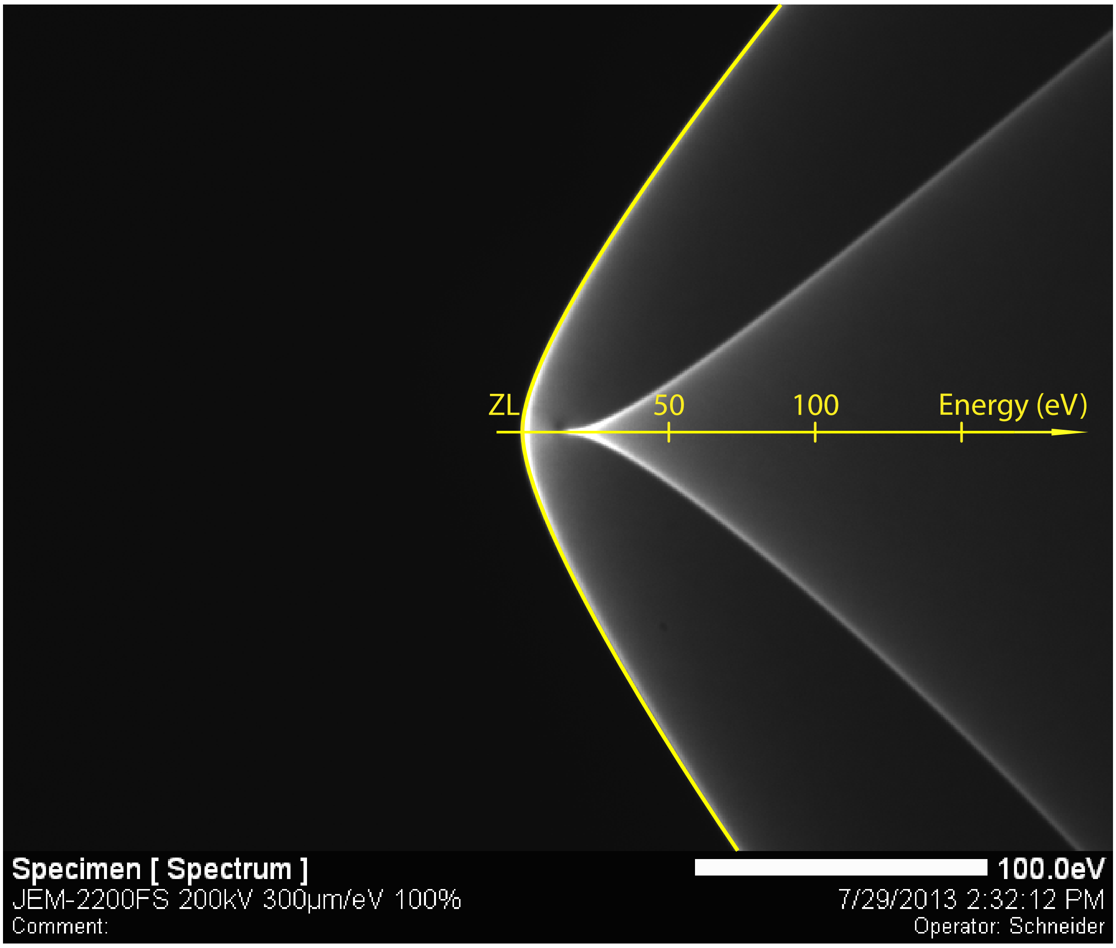

Figure 5.4: Shape of the spectrum without a specimen. The "Zero Loss" plane is the surface of the outer cone. The yellow scale shows the energy axis on the cone axis.

If the energy selecting slit is inserted, it cuts the spectrum perpendicularly to the cone axis. Figure 5.5b shows a 5 eV slit inserted on the vacuum spectrum. On the exit pupil plane, it will look like a ring. In image mode, correcting the non-isochromaticity is done by making the ring become as small as possible with the isochromaticity adjustment tool (adjust the intermediate lens system to be uniform in energy) and make the ring become a disk as large as possible with the slit position in order to select the very top of the cone, as sketched in Figure 5.7.

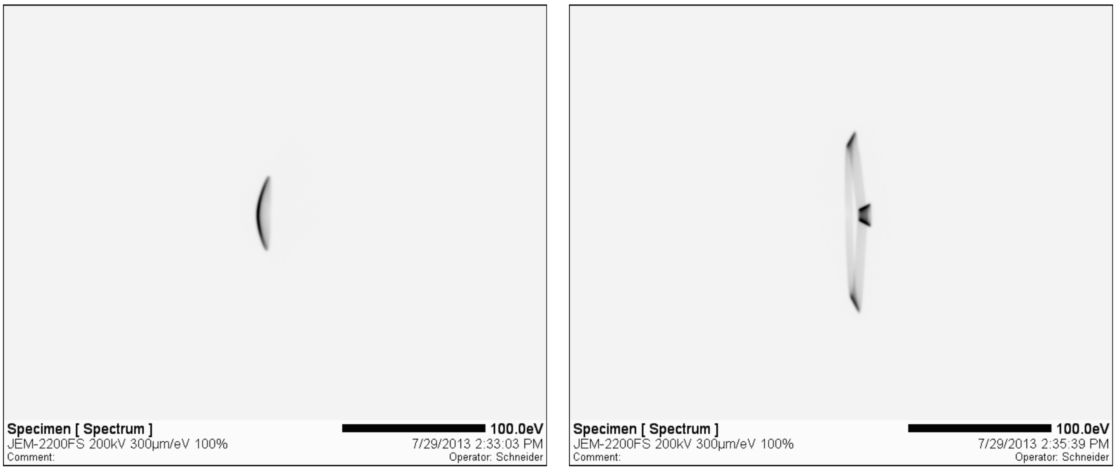

(a) Vacuum spectrum with an SAA1 inserted

(b) Vacuum spectrum with a 5 eV slit inserted

Figure 5.5: Vacuum spectrum with a selecting area aperture SAA1 (a) and an energy slit (b) inserted. The SAA cuts off the caustic and all part of the zero loss wider than the aperture projected on the filter entrance. The energy selecting slit cuts through the spectrum at a given energy. Part of the caustic and the ZL is still visible here because no specimen and no SAA is present. Gray scale is inverted for better contrast.

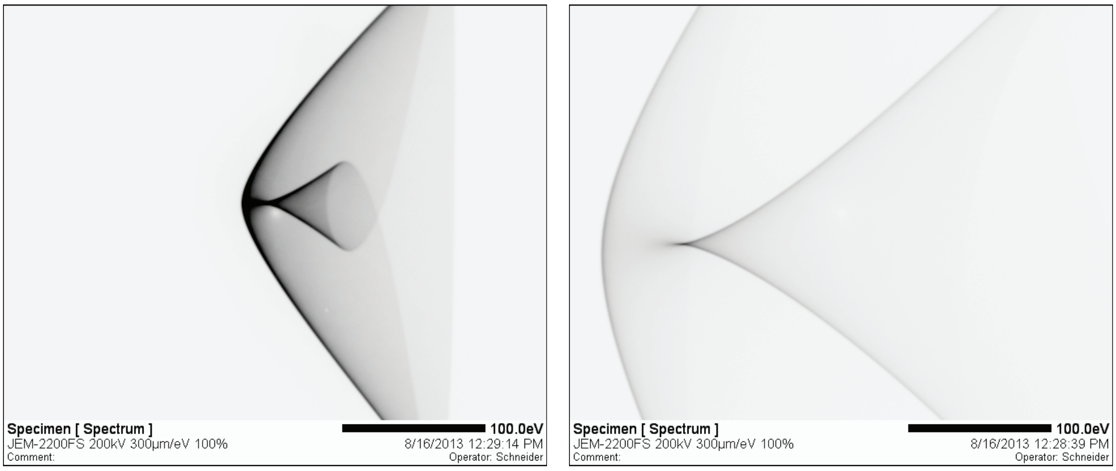

(a) Vacuum spectrum, negative non-isochromaticity

(b) Vacuum spectrum, positive non-isochromaticity

Figure 5.6: Vacuum spectrum with strong non-isochromaticity in the negative direction (a) and the positive direction (b). Gray scale is inverted for better contrast.

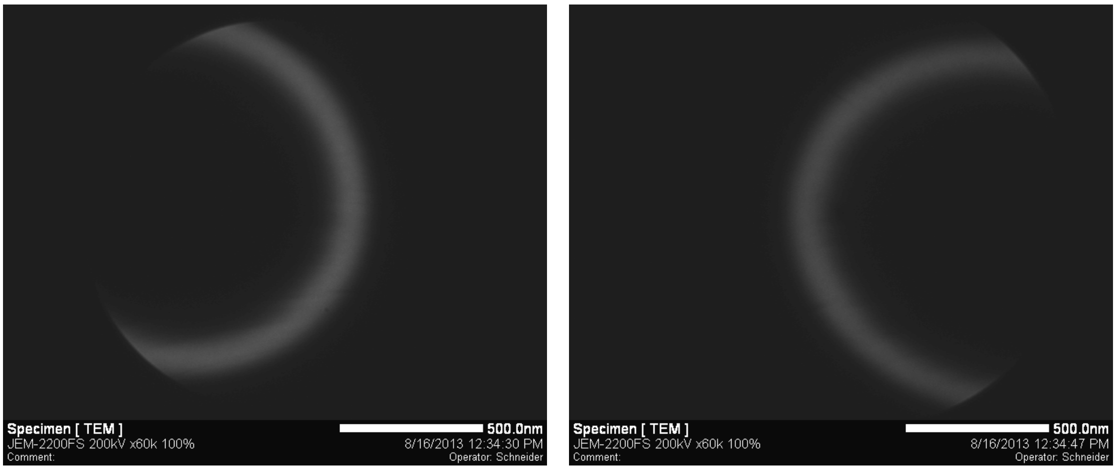

(a) Negative non-isochromaticity

(b) Positive non-isochromaticity

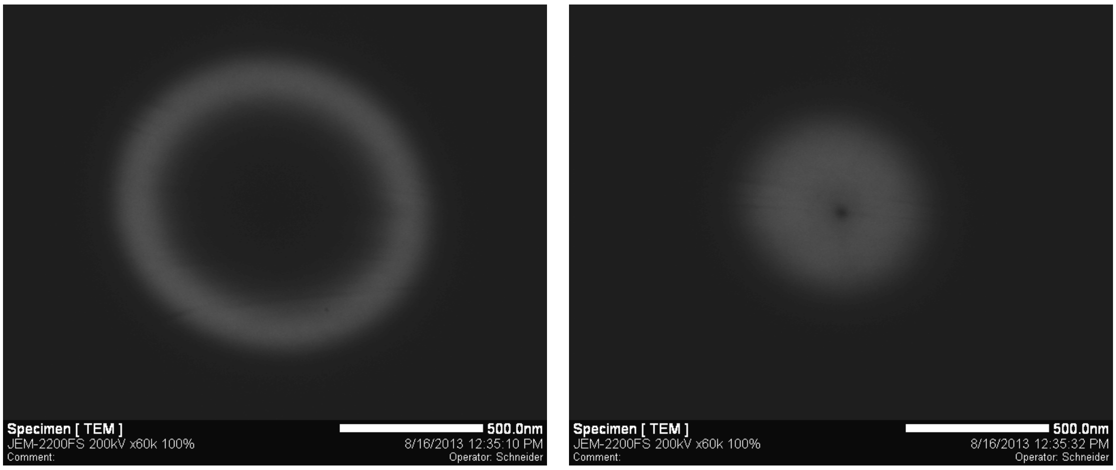

(c) Wrong slit position

(d) Well adjusted isochromaticity and right slit position

Figure 5.7: (a) and (b) show possible situations when the isochromaticity is not adjusted. To correct it, the ring has to be made as small and symmetrical as possible using the isochromaticity adjustment tool (c). The ring is centered on the screen using the FLA button and adjusting the slit position makes the ring become a disk (d).

In diffraction mode, the alignment of the Ω filter for optimal isochromaticity is much more complicated to reach, especially because the microscope does not behave the same in image and in diffraction mode. Indeed, in image mode, the isochromaticity adjustment affects all the IL lenses depending on the magnification, whereas lens $IL3$ is changed in diffraction mode when the camera length is lower or equal 120 cm and $IL4$ is affected if the camera length is higher. The detection of non-isochromaticity in diffraction mode is quite simple (but tricky to align, as shown hereafter): if the energy selecting slit is moved across the zero loss (0 eV) and the diffraction spots do not "light up" together, then the diffraction pattern is not isochromatic. An example of such a non-isochromatic diffraction pattern is shown in Figure 5.8.

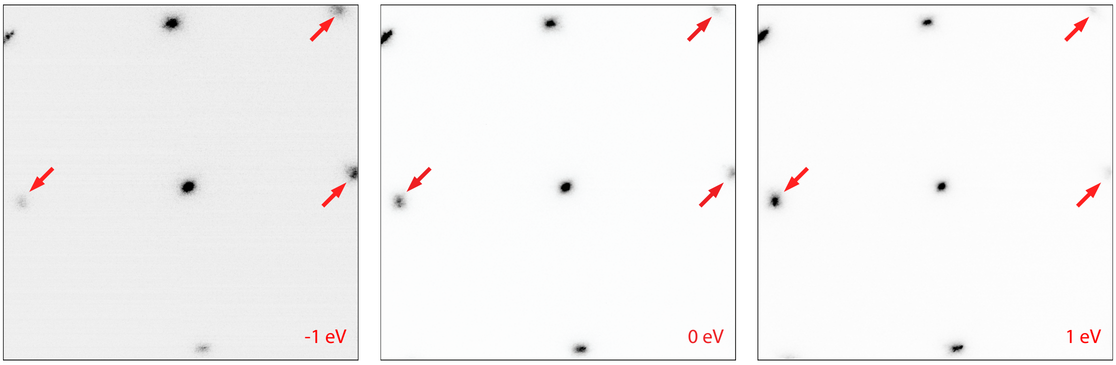

(a) Uncorrected, -1 eV (b) Uncorrected, 0 eV (c) Uncorrected, 1 eV

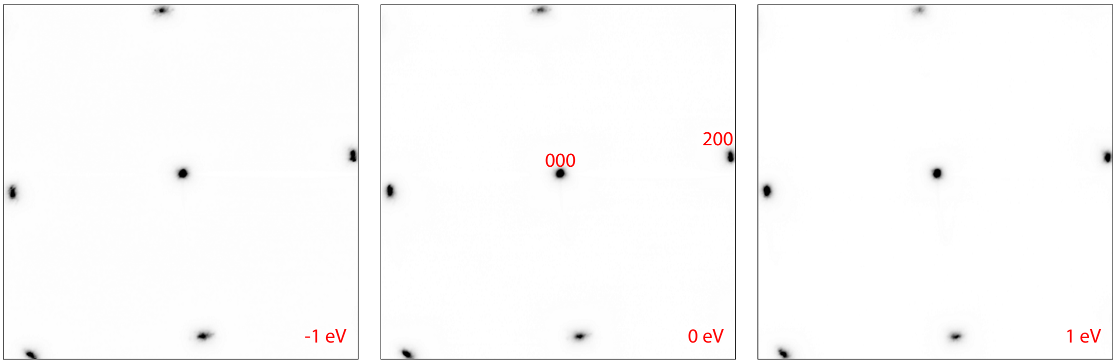

(d) Corrected, -1 eV (e) Corrected, 0 eV (f) Corrected, 1 eV

Figure 5.8: Single diffraction pattern at different energies showing non-isochromaticity (upper series). The red arrows show the spots lighting up and vanishing depending on the selected energy. The lower diffraction pattern series show an isochromaticity-corrected stack at different energies around the ZL. Gray scale is inverted for better contrast.

The correction of this non-isochromaticity is done by using the isochromaticity adjustment tool and moving the energy slit to make the diffraction spots light up simultaneously. Unfortunately, and unlike in image mode, it is not possible in diffraction mode to move the center of the optimal isochromaticity to the center of the image field, because the FLA correction do only move the diffraction pattern, not the optimal center. This makes the correction even more complicated, since the center of isochromaticity most probably lies between the diffraction spots, making it invisible.

Achromaticity

Non-achromaticity is the mismatch between the achromatic image plane (the exit pupil plane) of the Ω filter and the focus of the first projector lens. The achromatic image plane is the one where the path of the electrons from a given incident beam (with respect to the filter entrance) and which have undergone an energy loss meet the path of the electrons from the same beam without energy loss within the last magnet of the Ω filter (Figure 2.7).

In practice, non-achromaticity is easily detected in diffraction: if it is present in a diffraction pattern, little tails (shown in Figure 5.9a), which are actually energy-loss spectra, appear at each diffraction spot. Those tails are the energy spread of the electrons which do not have the same energy as the rest of the transmitted/diffracted beam (so each diffraction spot could work as a spectrum). Other effects that affect a non-achromatic diffraction pattern is the "squeezing" of the spots perpendicular to the tail, a small rotation and a change in magnification of the whole diffraction pattern. Non-achromaticity is corrected by simply using the "achromaticity" correction in the filter menu, which affects the focus of first projector lens. The achromaticity is extremely stable over time and in most of the cases, only a check is needed at the beginning of the TEM session.

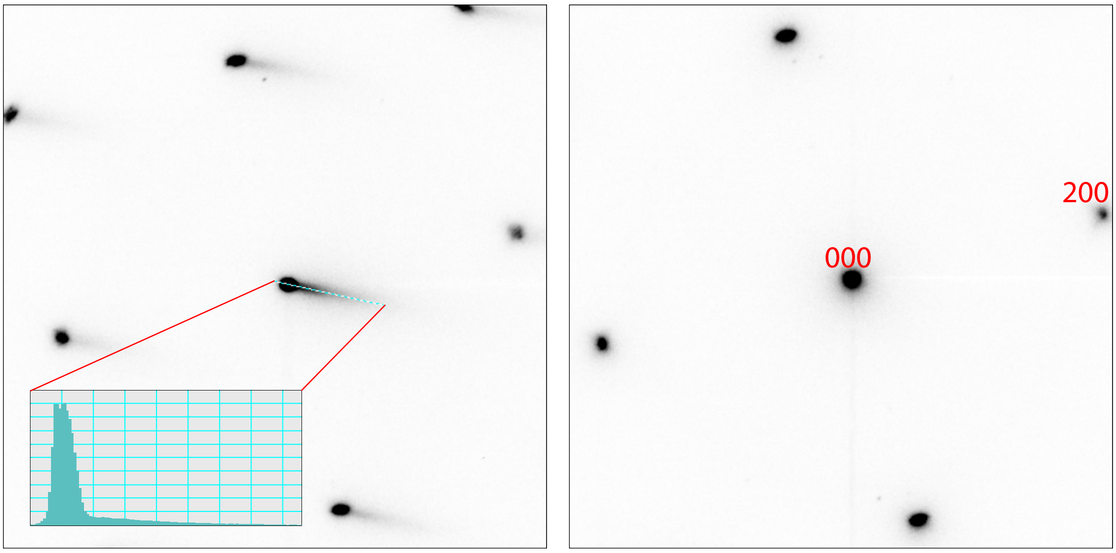

(a) Chromatic diffraction pattern

(b) Achromatic diffraction pattern

Figure 5.9: Diffraction pattern before (a) and after (b) achromaticity correction. The inset in (a) show the upcoming tails at the diffraction spots: an energy-loss spectrum. Gray scale is inverted for better contrast.

5.2 Data acquisition

Before the effective data acquisition, it is strongly recommended to perform a beam shower at the place where the acquisition will be done. Indeed, since the specimen will be illuminated with high intensity on a small area for quite a long time (up to an hour or even more in some cases), it is necessary to do everything to minimize contamination (an example of contamination being shown in Figure 5.10). If the sample allows it, put it into a plasma cleaner. Good beam shower results are obtained for EFNBED by removing the condenser lens aperture in NBD mode and illuminate a three times larger area of the specimen than effectively used for data acquisition for approximatively one hour.

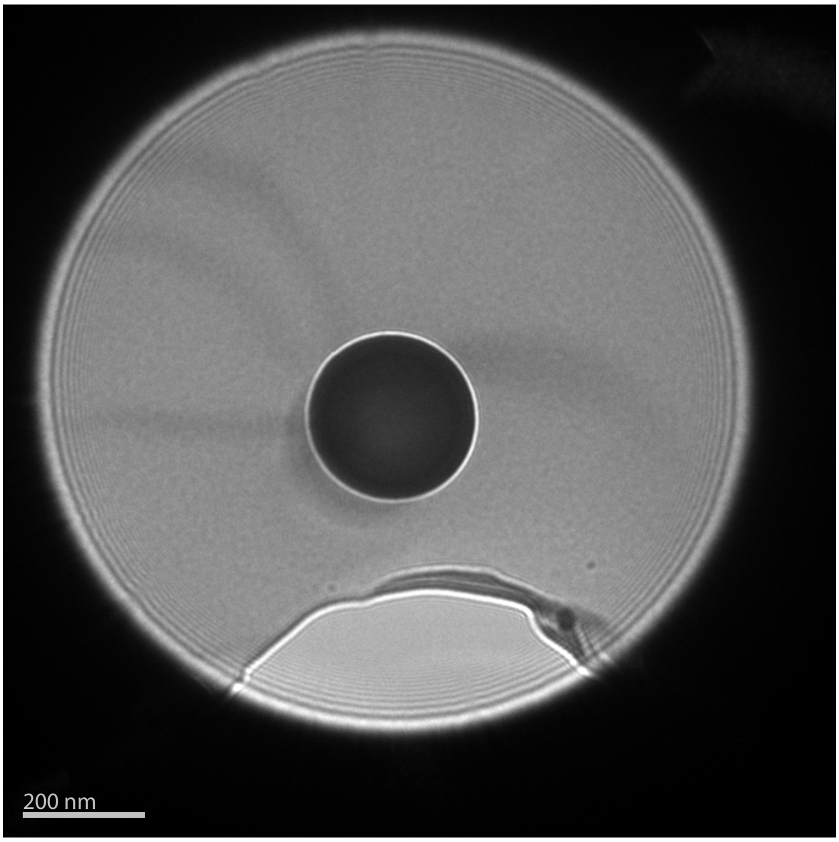

Figure 5.10: Example of contamination if the beam shower is not applied. The specimen is silicon, the image was taken in NBD image mode. The black circle in the center is a carbon contamination "pillar" which grows under the intense illumination. These pillars may grow on and under the specimen, and reach a size of over 10 times the sample thickness [77].

5.2.1 Acquisition with the CCD camera

As demonstrated in section 4.6, the required dynamics by EFNBED is extremely high, thus the data is acquired in two data sets, which then are combined together.

The first EFNBED data cube contains the zero loss peak of the final data set. In order to ensure that the data cube contains the whole ZLP an its tails, the energy range should be at least from -5 to 5 eV. The negative value of -5 eV for the first slice is achieved by aligning the microscope with a filter energy shift of FL = 5 eV. The exposure time and binning shall be chosen such as the CCD camera does not saturate when acquiring the diffraction pattern at the maximum of the ZLP. Care has to be taken not to chose an exposure time which is too short (less than 0.1 s), since shutter effects such as the tails (red arrow) shown in Figure 5.11 may arise. This figure also shows two horizonal black lines (green arrows) which most probably come from the high intensity (diffraction spots) at the internal boundary of the CCD camera (the Gatan UltraScan™ 1000 CCD detection area is a combination of four quadratic 1024×1024 px devices). Such artifacts have to be strictly avoided, since they alter the acquired data and thus the resulting information.

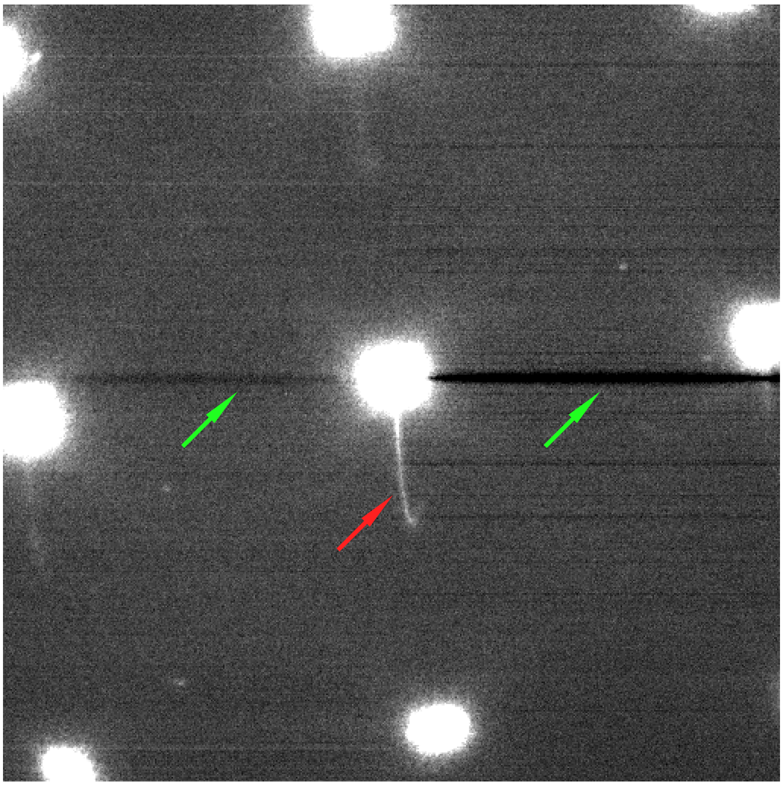

Figure 5.11: Possible artifacts in data acquired with a CCD camera: tails due to a shutter effect (red arrow) and black lines (green arrows), most probably due to high intensity on a CCD area boundary.

The second EFNBED data cube contains the low loss region. The exposure time shall be chosen such that the transmitted beam of the diffraction pattern taken at the energy loss of the most intense feature in the low loss region is just below the saturation limit of the CCD camera. This requires a good knowledge of the EELS spectrum of the sample and a "quick intermediate analysis" to determine the intensity of the feature. To increase the signal to noise ratio, it is possible to sum several frames of the same slice. The binning allows to reduce the exposure time of each slice and consequently the acquisition time of the whole stack. Indeed, this data cube takes the most time to be acquired. However, the gain in time has a cost in angular resolution, as explained in section 4.7. The first slice of this data cube should be as close as possible to the ZLP, but far away enough not to saturate the CCD camera with the exposure parameters.

In order to avoid to have to perform a binning or an interpolation in the energy direction, it is strongly recommended to use the same energy slit width δE and the same energy step for the acquisition of the two EFNBED data cubes.

5.2.2 Acquisition with imaging plates

When using imaging plates, it is recommended to insert an ENTA aperture. This allows then to subtract the "background noise" remaining on the IP. Some tests have been performed to analyze this remaining noise, and it turned out that it is not necessarily uniform (there might be some gradient) and the level is independent of the cleaning time. The mean value is about 17.5 with a standard deviation of 21.5 counts; the maximum pixel value is about 180. The origin of this background is uncertain, nevertheless one can assume that it may come from the cleaning light, from the plate itself (if it becomes old) or even from the scanner. An example of a diffraction pattern taken on an IP with an ENTA inserted is shown in Figure 5.12a.

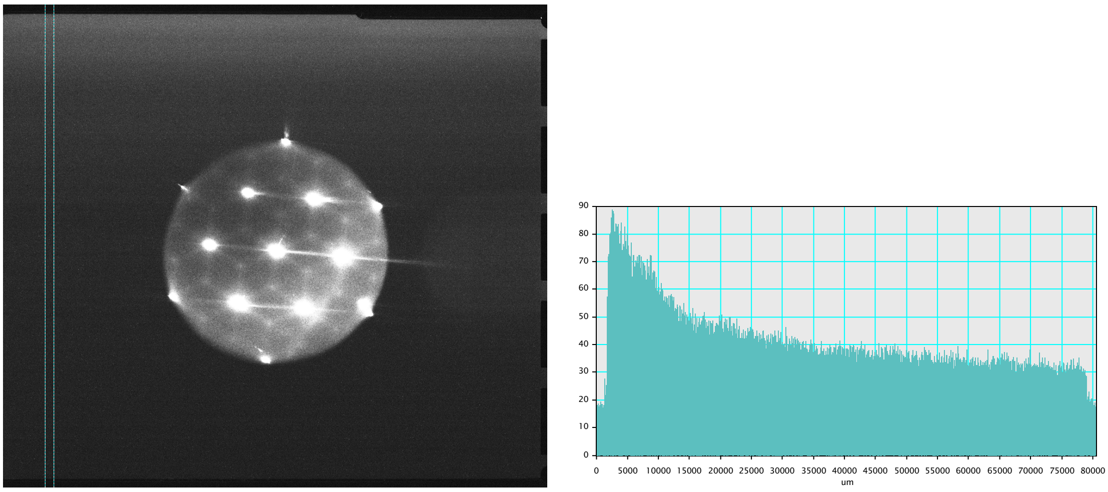

(a) Example of an IP with ENTA

(b) Profile of IP (a)

Figure 5.12: Example of an imaging plate with an ENTA2 aperture (a). The line profile (b) shows the gradient of the background intensity from the top to the bottom of (a) at a place masked by the ENTA.

Since the imaging plates are not software driven, the binning is necessarily 1 (although a binning is possible at the readout) and thus the exposure time may be increased by $4n$ with respect to the one used for the low loss region EFNBED stack, where n is the binning used for the acquisition of the low loss EFNBED stack. The factor 4 comes from the fact that the IP saturate at 4 times longer exposure time than the CCD camera does.

The quantity of plates is limited to 50 in the IP box, and the read-out takes a rather long time. It is thus recommended to use a reasonably wide slit (*e.g.* $\delta E = 1$ eV) and no energy overlapping from one IP to the other to cover the low loss region.

The background noise of each IP has to be corrected individually. This can be done by interpolating the background of the region covered by the ENTA and extrapolate the background of the whole plate from this. The background is then subtracted from the plate scan in order to get the effective data. The IP scan data set shall finally be stacked together and used as an EFNBED data cube.

It is also possible to combine CCD and IP by acquiring the zero loss data cube on the CCD and the low loss region on the IP (thus gaining intensity where the signal is weak). By doing so, it is important to crop the IP EFNBED data cube in order to match the size of the zero loss data cube. Special care has to be taken that the pixel size of both data cubes match before the combination.

5.3 Data formatting

Since the data for this work has been acquired with DigitalMicrograph™ (DM), it is easy to perform the whole analysis with this software. The first action to do is combining the zero loss EFNBED stack and the low loss region EFNBED stack into a single data cube. This is done taking into account the different binning and the different exposure time. The combination of the two stacks is performed by scaling the overlapping energy range of the low loss stack to the one of the zero loss stack such as the difference from one stack to the other is minimized. The overlapping part of the zero loss stack is then removed and the whole low loss EFNBED data cube added to the ZL EFNBED data cube.

Once the stacks combined, following corrections have to be performed:

1. Removal of the cosmic rays, appearing as very intense pixels. This may be done *e.g.* with a DM built-in script called "Remove X-rays." (this name is unlucky, as those intensities are cosmic rays and not x-rays).
2. Correction of the spatial drift (when using imaging plates), the image distortion, the energy drift and the non-isochromaticity, as explained by Schaffer *et al.* in [68]. A DigitalMicrograph script doing this correction has been written by Dr. Lucas[1].
3. Batson correction for plural scattering removal as well as angular distribution correction. These corrections are implemented within the data analysis routines shown in appendix D. Details about the Batson correction are given in section 6.1.3 in the description of this routine.

---

[1] Dr. Guillaume Lucas, scientist, CIME, EPFL.

The important correction in step 2 is the non-isochromaticity, since there is almost no energy drift (some small fluctuations in the beam energy may occur) and no image distortion in a diffraction pattern series. The mentioned DM script generates a non-isochromaticity map from the EFTEM stack (an example of such a map is shown in Figure 5.13) and performs the correction in each slice. From this image, one can see that the non-isochromaticity is not centered. This is always the case in EFTEM diffraction.

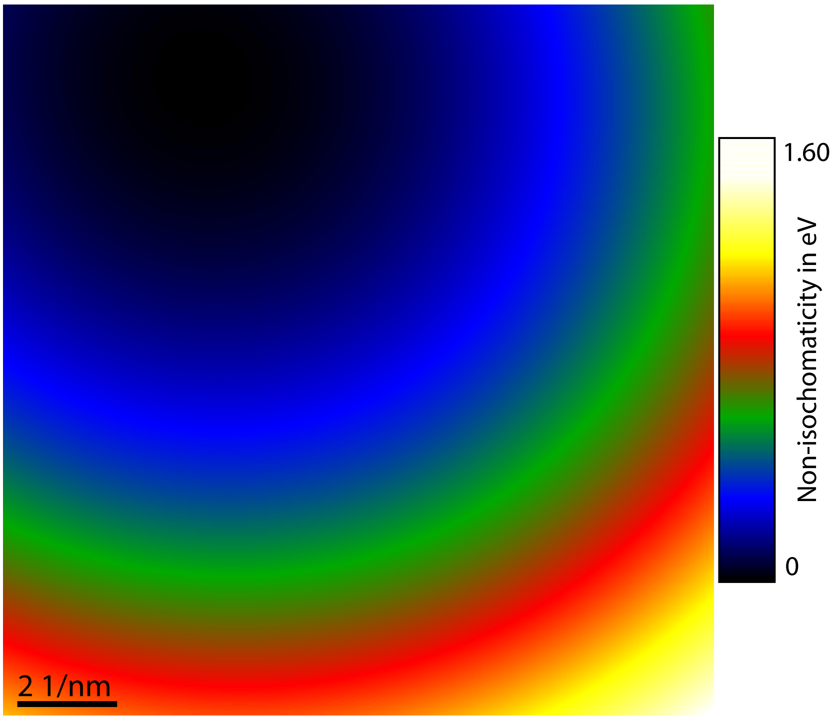

Figure 5.13: Example of a non-isochromaticity map. Once the map is generated, each slice of the EFTEM stack is adequately corrected.

5.4 Comparison with post-column momentum dependent EELS techniques

Nowadays, two main methods using post-column devices are known for momentum transfer resolved EELS acquisitions. Both perform the data acquisition in diffraction mode, since the angular information is already contained in the diffraction pattern. However, as will be shown, only a small fraction of the information is used.

Several different designs of post-column spectrum devices have been created since the beginning of EELS analysis [78]. However, until the early 70's, it was not possible to reach an energy resolution better than a few eV and the incident beam had to be lower than a few keV for angular resolved EELS. In 1971, Curtis and Silcox presented a spectrum analyzer (Figure 5.14a) [36], based on a Wien filter [79].

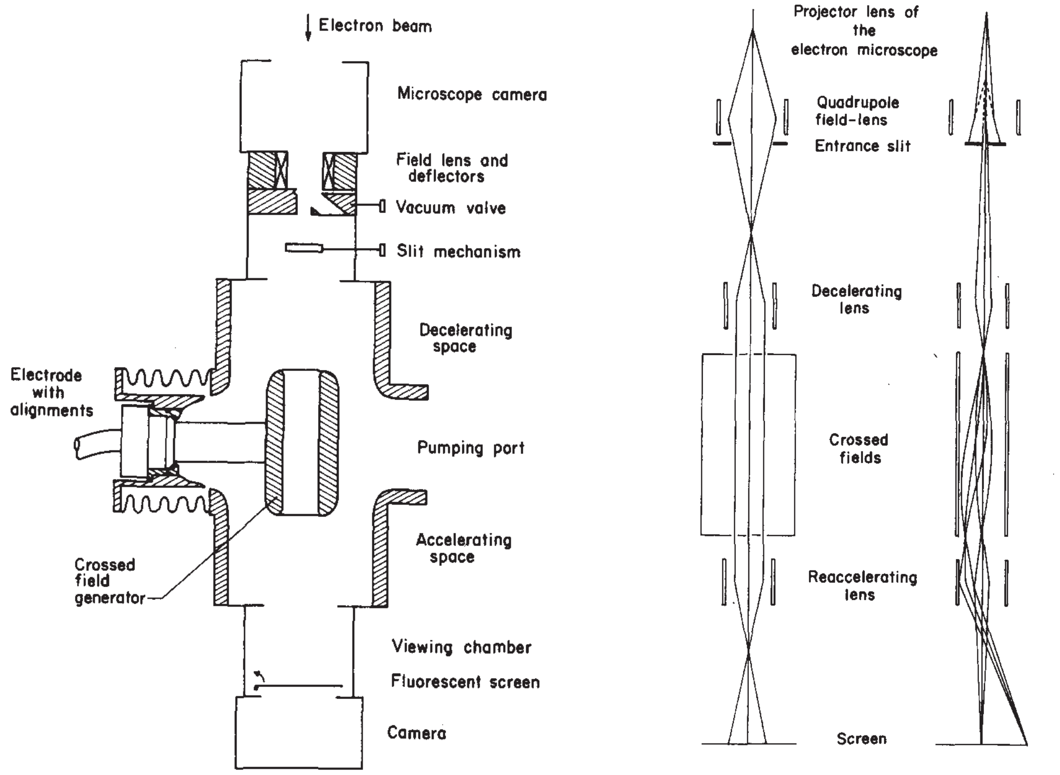

(a) Spectrum analyzer

(b) Beam path in the spectrum analyzer

Figure 5.14: (a) Post-column spectrum analyzer developed by Curtis and Silcox and (b) beam path within the device in the non-dispersive plane (left hand side) and energy-dispersive plane (right hand side) respectively.

The innovation of this device compared with the earlier energy analyzers was the slowing down of the electrons before the spread in the energy direction and the re-acceleration before projecting on photographic plates. By doing so, the energy resolution does no more depend on the stability of the high voltage supplies at an acceleration voltage of 100 kV , but depends only on the spread in energy of the incident beam (generated by a thermionic gun at that time) and on the Boersch effect which augments the thermal motion of the electrons [12]. Due to the Boersch effect, the energy resolution is limited to 1–1.5 eV (the best resolution achieved at the time of publication was 1.5 eV). The dispersion of the device is determined by the offset potential which slows down the electrons from the end of the column to the center of the energy spreading cross-field.

The angular resolution is obtained at the expense of the energy resolution and both depend on the spectrum analyzer entrance slit used because of the conservation of the brightness. Since the selecting slit has more weight in the energy resolution than the design of the spectrum device, Curtis and Silcox chose a Wien filter since the Möllenstedt filter [80] requires a very narrow slit.

The spectrum analyzer designed by Curtis and Silcox suffers from different aberrations which limit the resolution of the final angular resolved EELS map:

- a non-linear distortion of the space in which the spectrum exists. The linearity may be improved, but only at the expense of the energy resolution. The energy interval is also non-linear, which induces a change in the height of the loss peaks.
- Chromatic aberration, especially the one from the analyzer entrance quadrupole induce a tapering in the energy spectrum.
- A lack of orthogonality between the different alignment controls induce a skewing of the energy loss axis in the spectrum.
- The re-accelerating lens induces a pincushion which leads to a magnification of about 10% more at the extreme ends of the final image with respect to the center.

An example of a map acquired with this spectrum analyzer in diffraction mode is shown in Figure 5.15. The specimen is a 100 nm thin Al foil. The dispersion curve is seen about the 000 beam at each plasmon loss level and bright strikes can be seen for each of the first diffraction rings.

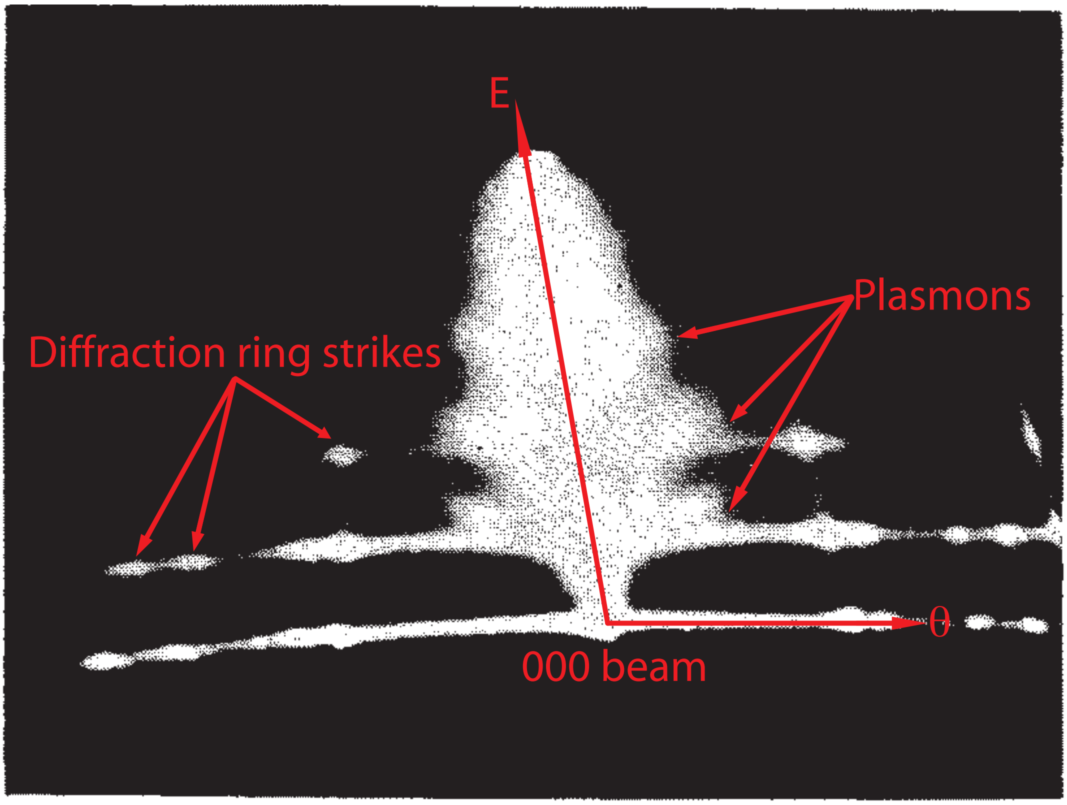

Figure 5.15: Angular resolved EELS map of a thin Al foil by Curtis and Silcox.

This device has also been used by Leapman [21] for the analysis of the orientation dependence of core edges from the anisotropic materials graphite and hexagonal boron nitride. The spectra were acquired with an energy resolution of 1.4 eV and the microscope was set up in selected area diffraction to reach an angular resolution of $2 \cdot 10^{-4}$ rad, corresponding to $q = 0.86$ nm^{-1} for an incident electron beam at 75 keV.

In the mid-nineties, post-column EELS devices such as PEELS [1] and GIFs [65, 81] have been developed. With these devices, instead of using a slit and spread the image or diffraction pattern in the energy direction, an aperture (selecting area aperture in image mode and objective lens aperture in diffraction mode) is used to limit the information projected on the spectrometer. The angular resolved EELS map is thus reconstructed from several EELS spectra. For angular resolved EELS, the OLA is used to select the desired momentum transfer $\boldsymbol{q}$ and a spectrum is acquired. The aperture is then shifted and a new spectrum is acquired. An alternative to moving the objective lens aperture is to keep an ENTA fixed and shift the diffraction pattern with the projector lens system. However, both of these variants are not necessarily accurate. With this method, the energy resolution is limited by the image-coupling in diffraction mode, and the angular momentum resolution is correlated to the size of the aperture. This kind of device is nowadays widely used, some examples being listed hereafter.

Wang *et al.* determined the momentum-dependent charge transfer in a high-T_c superconductor [24]. Using a cold FEG, they reached an energy resolution of 0.5 eV. The presented spectra have been acquired with a momentum transfer difference of at least 0.9 nm^{-1} one from the others.

The group of Neyer *et al.* performed an analysis of plasmon coupling using an asymmetric illumination on cross sectional metallic multilayers [82]. The illumination geometry, designed by the same group in 1994 [83], is applied to avoid contribution from the substrate to the EELS signal. The momentum resolution is optimized by using almost parallel illumination of the specimen area of interest, and the wave vector resolution is roughly ± 0.2 nm^{-1} at a beam acceleration voltage of 100 kV. The energy resolution is not specified.

Plasmons of multishell carbon and boron nitride nanotubes have also been studied by Kociak *et al.* [84]. They operated a STEM VG at 100 kV with a probe size of 0.5–1 nm. The energy resolution was 0.7 eV and the apertures were selected to give a convergence angle of 7.5 mrad and a collection angle of 16.5 mrad.

Laffont *et al.* used plasmons as a tool for *in situ* evaluations of physical properties for carbon materials [85]. The relation between the plasmon peak energy and the electrical resistivity, the Young modulus, the interlayer distance and the thermal conductivity respectively has been determines for 18 different carbon materials. The diffraction mode had specific conditions with incidence angle $\alpha = 5.1$ mrad and collection angle $\beta = 0.5$ mrad. The probe size was about 100 nm and the energy resolution about 0.9 eV. The momentum transfer sampling was set to $q = 0.2$ nm^{-1} in a range $q = 0.2$ nm^{-1} to $q = 1$ nm^{-1}.

Recently, Bertoni *et al.* used a GIF in the filter mode for determining the characteristic angle θ_E and the cut-off angle of a thin polycrystalline aluminum foil [35]. The energy resolution was about 1.2 eV and the angular resolution was $q = 0.3$ nm^{-1}. The purpose of the work was to demonstrate a model based fitting technique to extract the loss function from the angular resolved spectra instead of using a deconvolution technique. The loss function is estimated by using a nonlinear least-square minimization algorithm for the fit. The results are represented as 2D 60 × 24 mesh (E, q) maps with axes relative to the plasmon energy and the Fermi wave vector q_F of aluminum. The collection half-angle of the spectrometer was 0.3 mrad and Bertoni *et al.* used a script that permits the automatic acquisition of a series of spectra corresponding to different values of $q_\perp$ along a defined direction acting on the projector lens deflectors of the microscope, thus shifting the diffraction pattern instead of selecting the area of interest with an OLA.

Both presented techniques have a major disadvantage: they only use a small part of the diffraction pattern for a single acquisition. An enormous waste of information occurs therefor. The sketch of the angular resolved EELS map reconstruction is shown in Figure 5.16.

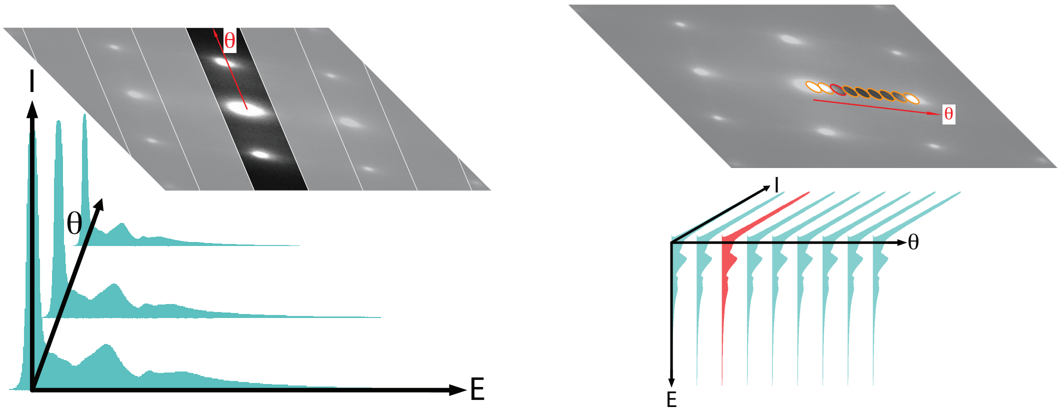

(a) Curtis and Silcox

(b) Post-column EELS devices

Figure 5.16: Sketch of momentum dependent EELS acquisition methods. (a) Curtis and Silcox use a slit to select the part of the diffraction pattern which is spread in the energy direction. (b) A series of EELS spectra is acquired while moving an aperture along the θ axis.

In both cases, the amount of information acquired in one time is restricted to the size of the selected aperture/slit. When a slit is used, its size is determining the energy resolution of the method. When an aperture is used (newer method with post-column EELS devices), the angular resolution is limited by the size of this aperture.

The advantage of EFNBED over the presented methods is that more 3D voxels are acquired at one time (which makes EFNBED very efficient), and that the angular resolved EELS map is extracted afterwards. Thus, all available information is used. Furthermore, the spatial, angular and energy resolution are independent one from the other and all limited to the intrinsic resolutions (angular, energy) and installed devices (spatial) of the microscope.

5.5 EFNBED using imaging plates

As mentioned in section 4.6, EFNBED pushes the CCD camera to its limits with the dynamics, even by separating the acquisition of the zero loss peak and the low loss region. A possibility to overcome this limit is the use of imaging plates. Some new issues such as stacking the IP read-outs together or the decreasing of the DQE while working in diffraction mode may arise.

In order to determine these new challenges, a whole set of silicon data from 2 to 41 eV with a step of 1 eV has been acquired using the acquisition process mentioned in this chapter. The background has been removed from each plate using a fit routine (similar to the one used for the non-isochromaticity detection) and the resulting diffraction pattern have been stacked together and aligned. An energy-loss spectrum resulting from this stack is shown in Figure 5.17a.

The unusual shape of the spectrum (especially around 20 eV) leads to following conclusion: the gain (or sensitivity) of the IP differs from plate to plate. This may have different origins:

- The plates are not from the same series, thus the active layer may not be the same for each plate.
- The plates have not been used the same number of times. Since they are re-usable for about 1000 times, there must be a degradation of the active layer each time.
- The degradation of the active layer may also take effect with the age of the plates.
- The DQE is not the same for each plate.

Two possibilities are suggested to overcome this issue:

1. Measure of the gain: if there is a possibility to measure the gain of each plate, it would be possible reconstruct a gain-corrected stack to perform the q-EELS analysis. A solution would be an additional information on the plate in form of a "single point source illumination". If a place on each plate with the ENTA aperture as background is illuminated with the same source for the same amount of time, then the sensitivity of the plate can be determined by scaling the resulting spot of this source. This point source could be the beam of the microscope in the vacuum (without specimen). However, it is not 100% straightforward to guarantee that the intensity from the beam will stay constant that long.
2. A less complex, but also less precise solution would be the fit of the EELS spectrum with a (much) noisier one taken with the CCD camera. The idea is the following: the spectrum taken with the CCD camera serves as reference for the scaling of the imaging plates (relative to the sensitivity). Once the IP stack corrected, the more precise data (for the reasons mentioned in section 2.3) can be extracted for the q-EELS analysis.

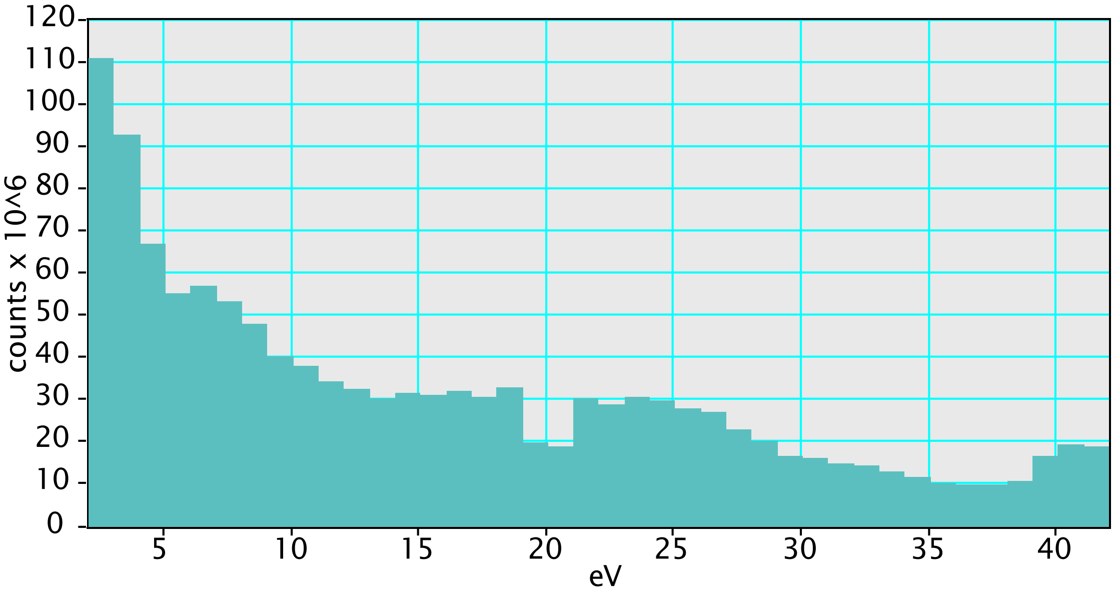

(a) Reconstructed spectrum from IP's

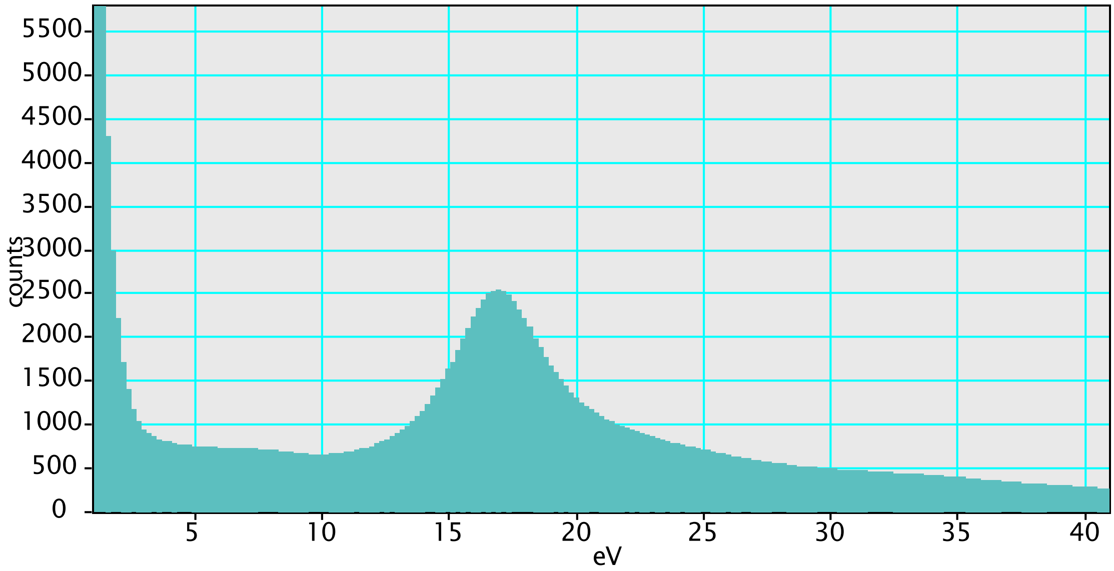

(b) Si spectrum from the EELS atlas

Figure 5.17: Spectrum taken at the transmitted beam in the reconstructed imaging plate stack (a) and the silicon spectrum from the EELS atlas [86] (b) adapted to the energy range of (a) for comparison.

6 Angular resolved EELS with Energy Filtered Nano-Beam Electron Diffraction

6.1 Data extraction

Once the data are acquired and combined in a single non-isochromaticity corrected EFTEM data cube, it can be analyzed and the angular resolved low loss EELS information extracted. This is done in two different ways, which are described hereafter.

6.1.1 Working conditions

The data presented in this chapter was acquired on a sputtered silver film with a sample thickness of 50 nm for silver, determined with the thickness measurement method described by Egerton [1]. The sample has been put into a ion polishing machine for gentle surface contamination removal (25 minutes at 0.6 kV beam, 8° at the bottom and 5° on the top, followed by 5 minutes at 0.4 kV at same angle conditions) prior to an electron irradiation (usually called "beam shower") of 1 hour in the TEM column.

The acceleration voltage and the emission current of the microscope were set to 200 kV and 60 μA respectively. CLA3 with a diameter of 40 μm was used, giving a parallel illumination area with 220 nm diameter on the specimen in NBD mode with a spot size of 1.8 nm and convergence alpha3. A filter lens energy (FL) shift of 5 eV has been applied before setting the 0 eV position of the energy selecting slit.

As explained in section 5.2.1, the zero loss stack and the low loss stack were acquired separately. Both stacks were taken using a camera length of 80 cm centered on the transmitted beam (so that the first diffraction spots are visible), a slit width of $\delta E = 0.5$ eV and a step of 0.25 eV between each slice. The ZL stack has been acquired from 0–12 eV, which gives an effective energy range of -5–7 eV with the FL shift. The exposure time of each slice was set to 0.15 s with a CCD binning of 1, giving a total acquisition time of 271.8 s for 48 slices. The low loss stack has been acquired in an effective energy range of 2–42 eV. The exposure time of each frame was 0.75 s with a CCD binning of 4, giving a total exposure time of 542.7 s for 160 slices.

Before the recombination of the two stacks, the ZL data cube has been binned with a DM routine in the (x, y) planes, in order to match the low loss data cube. The final EFNBED data cube after re-alignment has a dimension 505 px × 506 px × 183 slices, which corresponds to 398 nm^{-1} × 399 nm^{-1} × 45.75 eV. The angular resolution in the stack is 0.5 nm^{-1} and the energy resolution is 1 eV, with a residual non-isochromaticity of 1.6 eV corrected after the recombination (section 5.3).

Note: the norm of the wave vector k is defined in physics as $k = \frac{2\pi}{\lambda}$, whereas $k = \frac{1}{\lambda}$ in crystallography. These two definitions lead to a scaling factor of 2π between the scale bars of the diffraction patterns acquired with DigitalMicrograph (using the physical definition) and the values reported in this work (crystallographic definition in order to match the theoretical calculations).

6.1.2 Radial integration

The "Radial integration" analysis is done with the `RadialIntegration.s` script (fully copied in appendix D). This script takes the whole data cube and scans several times through the different slices (at different energies, the dashed rings in Figure 6.1). Each scan is done with a different analysis area, a ring with a width chosen by the user (this width may also be called "integration step"). The first scan is performed at the center of the diffraction pattern (the transmitted beam, whose position is determined automatically as being the brightest pixel in the most intense slice) and the ring is increased each scan until reaching 5/8 of the edge distance of the stack in the (x, y) plane (the value 5/8 has been chosen arbitrarily, but it gives good results). Each scan results in a line of a q-EELS map which corresponds to the EELS spectrum for a given scattering angle (corresponding to the radius of the ring). This spectrum is divided by the surface of the ring for normalisation.

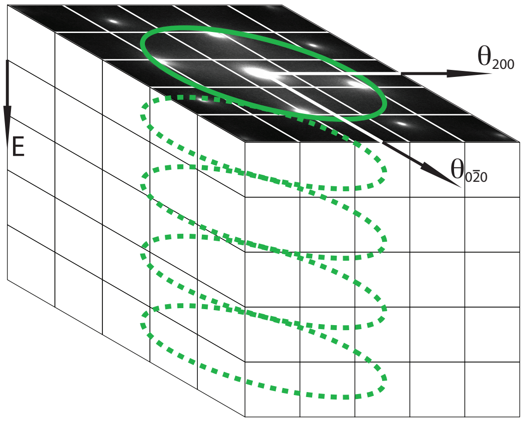

Figure 6.1: Schematic representation of the radial integration. The stack is scanned through the energy direction (green dashed rings) with a given radius (namely the scattering angle θ). Once the scan performed, the radius is increased and the scan performed again.

6.1.3 Batson correction

At each part of a diffraction pattern, there is contribution from the single scattering process towards this position and from plural scattering from anywhere else. In this work, plural scattering is considered as a combination of one single inelastic scattering process and one or more elastic scattering processes, as done by Batson and Silcox in 1983 [20] (Figure 6.2). The reason is that the deconvolution of plural inelastic scattering processes is much more complicated, requiring the use of Bessel functions as shown by Su and Schattschneider [87].

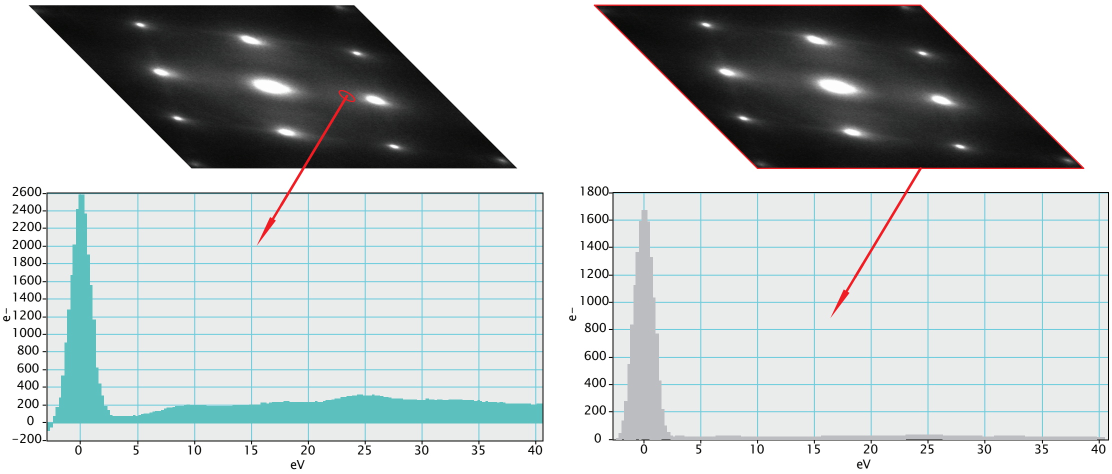

(a) Spectrum with specific q

(b) Image spectrum

Figure 6.2: The idea behind the Batson correction is that the single inelastic plus elastic scattering at $\boldsymbol{q}$ is the sum of the inelastic scattering at $\boldsymbol{q}$ (a) plus the elastic scattering from the image (which corresponds to the integral of the diffraction pattern) [20] (b).

With their method, Batson and Silcox use an EELS spectrum taken in image mode to perform the plural scattering correction on the diffraction EELS spectra. However, the energy range between the spectrum acquired in image mode and the recombined EFTEM stack do not match, and it is quite challenging to correct this in DM. Therefore, the spectrum used for the Batson correction in this work is directly reconstructed from the EFTEM stack by summing each slice and adding it as the value at the given energy in the spectrum for the Batson correction. The comparison between the reconstructed spectrum and a spectrum acquired in image mode on the same place of the specimen and with same illumination conditions is shown in Figure 6.3. The collection angle for the acquisition of the spectrum in image mode was 10.5 mrad, which corresponds approximatively to $2\theta_B$ for silver with an acceleration voltage of 200 keV (the first diffraction spots were just hidden by the OLA1) since $d_{200,Ag} = 0.2005$ nm. A slight energy shift of the spectrum acquired in image mode with respect to the reconstructed spectrum is visible, and a discrepancy appears in the low loss region. The difference in intensity at high losses comes from the fact that for the reconstructed spectrum, the first diffraction spots are taken into account, thus more electrons which have not undergone any energy loss are considered, lowering the relative intensity of the low loss region with respect to the ZLP. The increasing energy shift with increasing energy loss comes from a inaccurate energy calibration either of the dispersion or of the FL shift: considering the edge at 25 eV energy loss, the energy shift is about 0.75 eV, which is a mismatch of 3%. This is also a reason why the Batson correction works better with the reconstructed image spectrum. The energy resolution (the FWHM, measured on both spectra) during this session was about 0.9 eV.

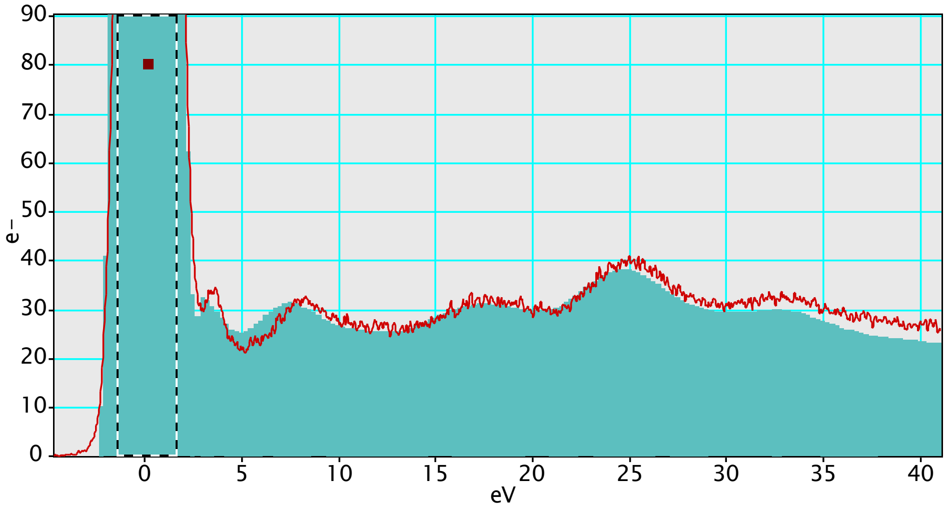

Figure 6.3: Comparison between the image mode acquired (red line) and the reconstructed spectrum for the Batson correction. The spectra are scaled to match over the dashed integration window (3 eV). There is good agreement, thus the Batson correction may be performed with the reconstructed spectrum without altering the data.

Batson and Silcox demonstrate mathematically [20] that all contributions to the scattering may be decomposed into a combination of quasi-elastic scattering (close to the ZLP), and electronic multiple-scattering when the multiple inelastic scattering is neglected. Furthermore, they prove that the intensity distribution produced by normalizing the image spectrum to the quasi-elastic intensity at each momentum transfer $\boldsymbol{q}$ is a good approximation to the quasi-elastic plus electronic (plasmon) scattering at $\boldsymbol{q}$, leading to the normalization over an energy window. The multiple electronic scattering intensity as a function of scattering angle is obtained by the intensity in the BFP. Thus, subtracting the normalized image spectrum from the originally acquired spectrum leads to the single scattering EELS spectrum.

The effect of the Batson correction is demonstrated in Figure 6.4. The correction process goes as follows: the reconstructed spectrum (red spectrum in Figure 6.4c) is scaled to the EELS spectrum of a given momentum transfer q. The scaling is performed by multiplying the reconstructed spectrum by a scalar such that the integration of the ZLP over a given energy window (3 eV for this work) are equal in both spectra. The corrected spectrum (light green filled spectrum in Figure 6.4c) is obtained by subtracting the scaled reconstructed spectrum from the uncorrected one (turquoise filled spectrum in Figure 6.4c). This correction is performed line by line over the whole uncorrected map (Figure 6.4a) in order to finally obtain the Batson corrected map, as shown in Figure 6.4b.

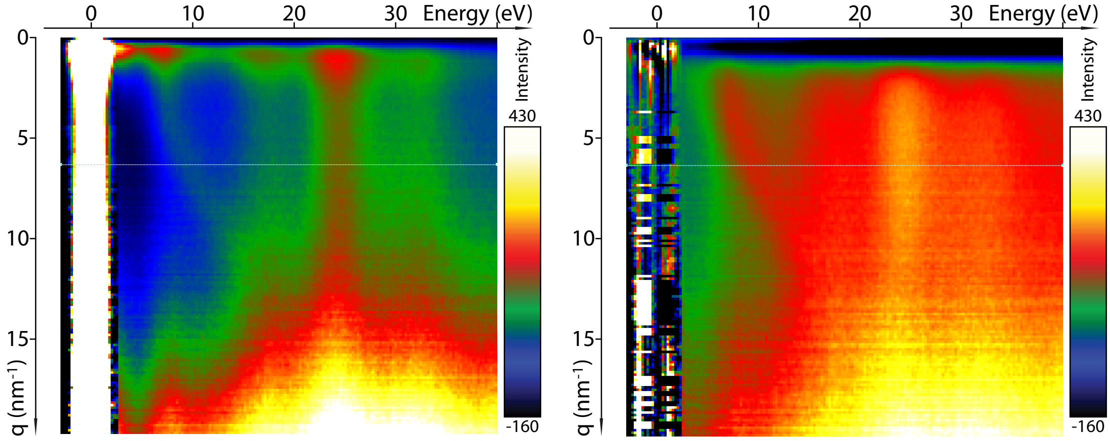

(a) Uncorrected q-EELS map

(b) Batson corrected q-EELS map

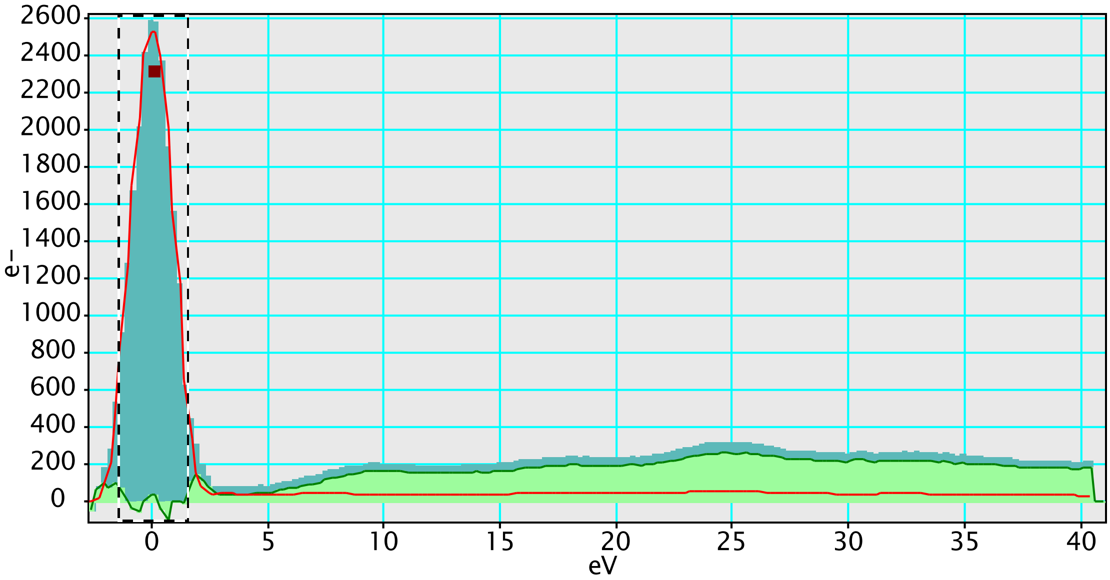

(c) Sketch of the Batson correction

Figure 6.4: Sketch of the Batson correction. A spectrum at a given momentum transfer q (the turquoise filled spectrum in (c), here at $q = 6.283$ nm^{-1}) is extracted from the uncorrected map (a). The image spectrum for Batson correction (red spectrum in (c)) is scaled to the initial EELS spectrum over an energy window of 3 eV on the ZLP and subtracted, giving the final Batson corrected light green spectrum in (c). Doing so for each q gives the corrected map (b).

After the Batson correction, the angular distribution correction is performed within the extraction routine by dividing each pixel of the map by the Lorentzian function $f(E,\theta) = \frac{1}{\theta^2+\theta_E^2}$, where (E,θ) are the coordinates of the considered pixel, θ being converted into q via $q = k\theta$. Remembering the loss probability (equation (4.5)), this Lorentzian function is, next to a scaling factor, the only undesired term in the double differential scattering probability in order to retrieve the dielectric tensor. The final angular resolved EELS map is shown in Figure 6.5.

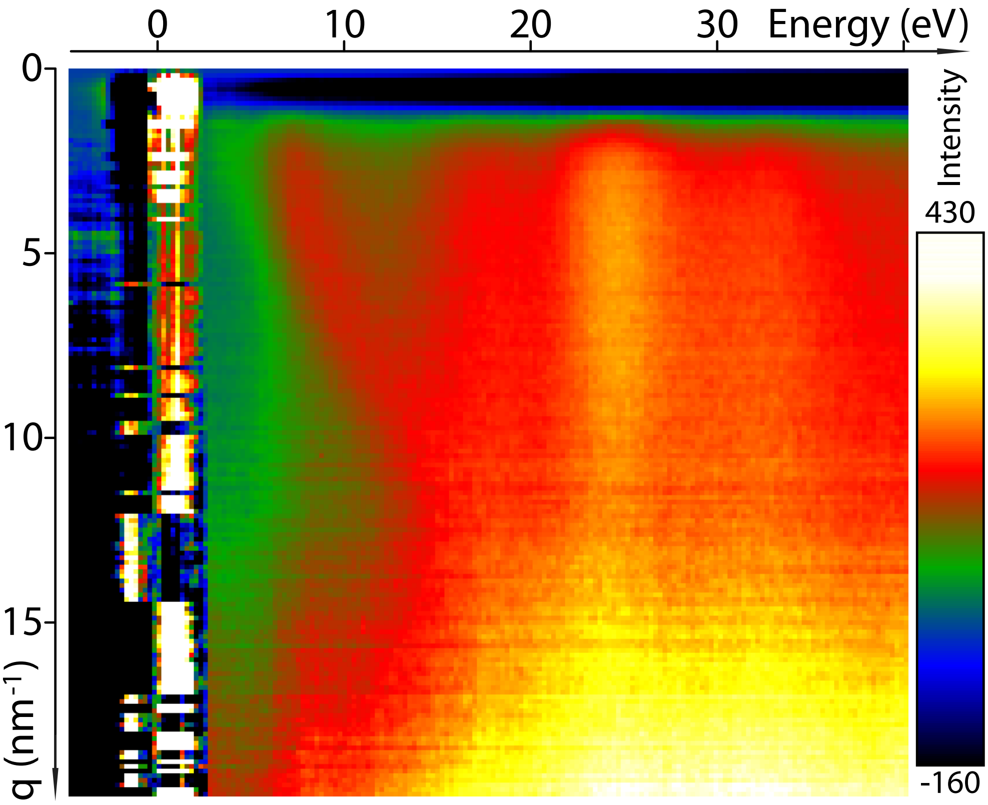

Figure 6.5: Angular resolved EELS map of [001] oriented silver. The energy range is from –4.75 to 40.25 eV with a step of 0.25 eV. The spectra are from $q = 0$ to $q = 19.73$ with a step of 0.126 nm^{-1}. The map is in "temperature" colors, meaning the warmer the color, the more intensity at this place.

Figure 6.5 is a Bethe surface obtained using EFNBED. The energy range is from –4.75 to 40.25 eV from left to right with a step of 0.25 eV. The spectra are from $q = 0$ to $q = 19.73$ nm^{-1} from the top to the bottom with a step of 0.126 nm^{-1}. The first 7 eV (the noisy part on the left) is the ZLP, which has been removed with the Batson correction. The upper part of the map (the blue edged black area, 9 spectra corresponding to $q = 0$ to $q = 1.13$ nm^{-1}) has contribution from the transmitted beam. This part appears black because of the Batson correction. Indeed, the transmitted beam has mostly elastically scattered electrons, thus the ZLP is much more intense with respect to the low-loss part than elsewhere. This ZL/low-loss ratio gives then a wrong estimation for the Batson correction and too much "multiple scattering electrons" are removed in the low-loss region, making this part negative.

The effective information is contained in the green-red-yellow area, colored with a "temperature" color code, meaning the warmer the color, the more intensity at this place. Thus, the yellow vertical line at about 25 eV corresponds to the most intense peak in the map, which is an inter-band transition from the *d* state to unoccupied states above the vacuum level. Starting at a certain momentum transfer (when the yellow line broadens, at about q = 12.5 nm^{-1}) contribution from the first diffraction spots 200, $\bar{2}$00, 020 and 0$\bar{2}$0 arises and alter the signal.

Some tests have been performed using Principal Component Analysis (PCA) on the data before doing the radial integration analysis. It follows that using too few principal components almost kills the data as shown in Figure 6.6a, and using enough components smoothen the variance in the map, but doesn't improve the data in a significant way (Figure 6.6b). Thus, PCA was not applied for this work. The reason is that PCA is a good method to improve data made out of linear combinations of components. However, since angular resolved diffraction EELS is far from a linear phenomenon, almost all components are needed to reconstruct the data.

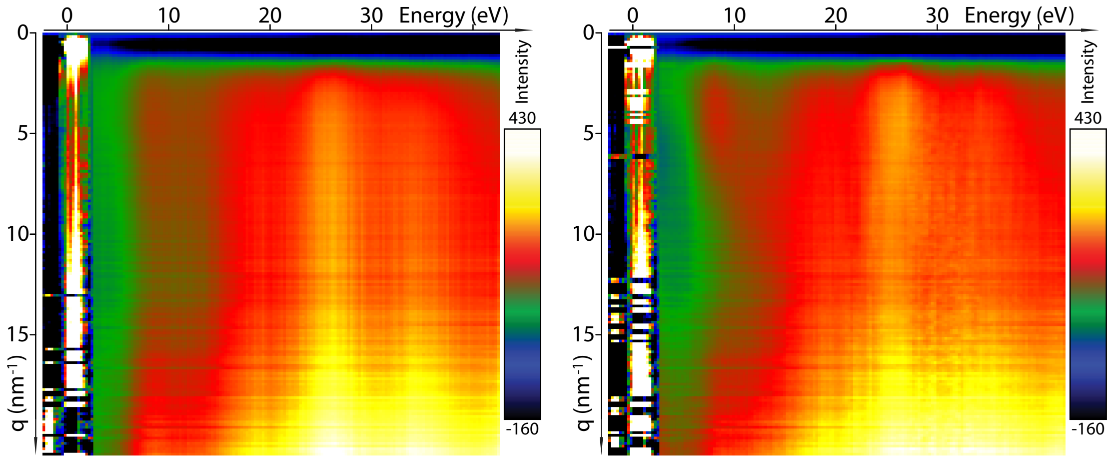

(a) q-EELS maps with 11 principal components out of 172

(b) q-EELS maps with 39 principal components out of 172

Figure 6.6: q-EELS map with PCA. Using too few components almost kills the data (a), and using enough components smooth the map (b).

Note: the calculation time of an angular resolved EELS map may be quite long depending on the size of the EFTEM stack and the entered integration step. 50 minutes were necessary to compute Figure 6.5 with a step of 1 pixel. It is possible to see the advancement of the calculation in the "Progress" bar in DigitalMicrograph.

6.2 Comparison with theoretical calculations

The calculations presented here were performed with the full-potential linearized augmented plane-wave code Exciting [88]. Wave functions were expanded up to the cutoff parameter $R_{\mathrm{mt}}K_{\mathrm{max}} = 8$, and ground state calculations were carried out using the Generalized Gradient Approximation (GGA) of Pedrew *et al.* [89] for the exchange-correlation potential. The loss function is given by $\Im(-1/\boldsymbol{\varepsilon}) = v\ \Im(\chi)$. It corresponds to the Born approximation to the scattering problem [70]. Here χ is the density-density response function and v is the bare Coulomb interaction. In the construction of the non-interacting density-density response function χ^0, the GGA wave-functions as well as the single-electron eigenvalues were used. The loss function was calculated in the energy range of 0–55 eV to avoid an overlap with the silver M-edge (excitation from $3p$ orbitals to the Fermi level), which occurs at ~58 eV in GGA. Response function calculations were converged when including empty states up to 200 eV above the Fermi level. The interacting response function χ has been obtained in the RPA from the solution of the Dyson equation, symbolically $\chi = \chi_0 + \chi_0 v \chi$ [73]. The calculation of the q-dependent loss function was performed in two energy ranges. In the first one, which covers energies up to 15 eV, the dispersion of two plasmon peaks has been calculated. Here, local-field effects are very small and have been therefore neglected. The computation required a very dense k-point sampling, *i.e.* an off-symmetry 30 × 30 × 30 regular k-point mesh. For energies between 10 and 55 eV, the dispersion of peaks caused by inter-band transitions have been determined taking into account local-field effects and including at least three shells of reciprocal space vectors in the inversion of the Dyson equation. In this case, an off-symmetry 20 × 20 × 20 regular k-point mesh has been used. These sets of k-point meshes were chosen because of practical reasons. The lowest plasmon peak is very narrow, thus it is essential to have dense k-point sampling in the low-energy range. In contrary, peaks caused by inter-band transitions are substantially wider, and therefore a sparser grid suffices.

Figure 6.7 is the resulting q-EELS map, calculated from the band structure of silver along the [111] zone axis, published in 2010 [63]. At first sight, there is good agreement. All expected peaks are visible, except peak 1 which is hidden by the ZLP in the experimental data and has been removed with the Batson correction. At higher q, the small peak at energy 8–9 eV (white ellipse in Figure 6.8) predicted by the theory is confirmed. Peak number 2 has an energy dispersion with an almost quadratic shape. This shape is also predicted by the theory [63]. Peak 3 is in good agreement, as well as the merge of peaks 2 and 3 (black ellipse in the experimental data, and easily recognizable in the theoretical map). Peaks 4 and 5 seems to be much sharper in theory than found experimentally. Nevertheless, it is possible to see the inter-band transition (peak number 4) narrowing with increasing q predicted by the theory confirmed. The general broadening of the peaks in the acquired map comes from the resolution of the microscope, which is at about 1 eV, and probably also from some remaining contamination. Furthermore, starting on $q = 12.5\ \mathrm{nm}^{-1}$, there seems to be contribution from the first diffraction spots, which makes the comparison between theory and experiment more and more difficult. In any case, it is possible to see that at low momentum transfer, the peaks

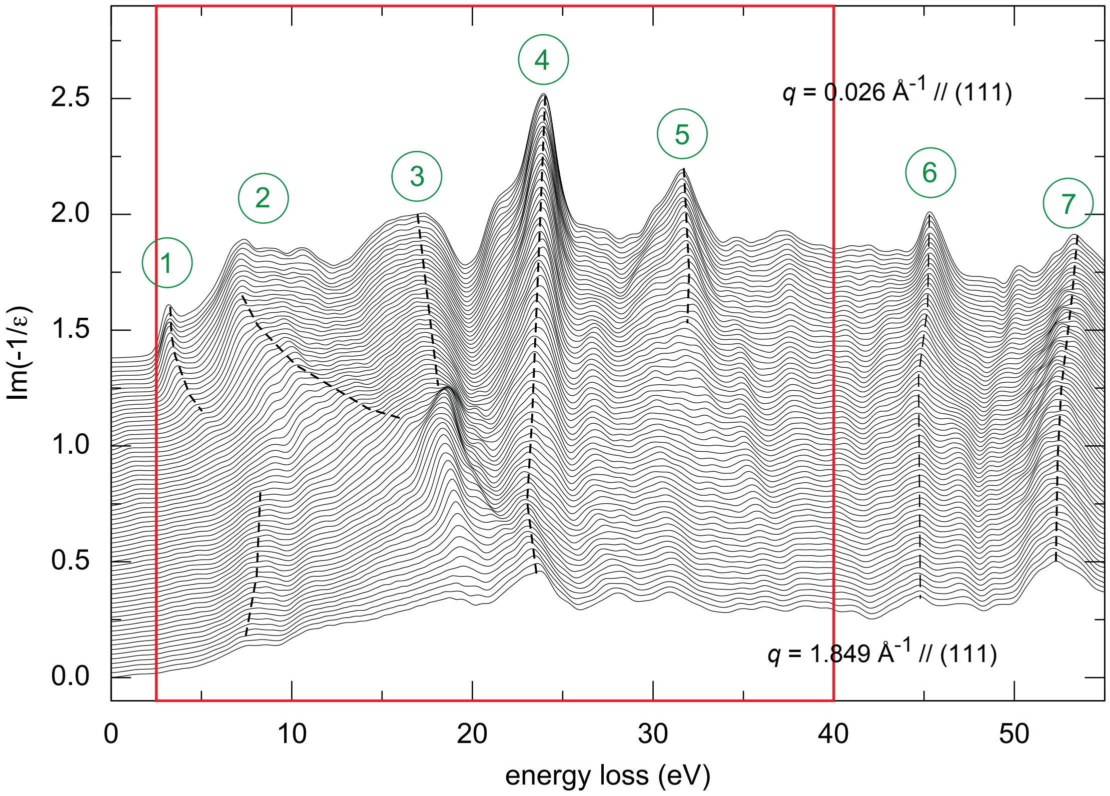

Figure 6.7: Theoretical angular resolved EELS map along the [111] zone axis for $q = 0.26\ \text{nm}^{-1}$ to $q = 18.49\ \text{nm}^{-1}$. The red rectangle shows the area covered by Figure 6.5 in energy (from 2.75 eV to 40.25 eV).

are easily recognizable and they vanish with increasing q.

The peaks and edges may be explained with the behavior of the real and the imaginary part of the dielectric function ε_1 and ε_2 respectively, since the loss function is given by

$$\Im\left(-\frac{1}{\varepsilon}\right) = \frac{\varepsilon_2}{\varepsilon_1^2 + \varepsilon_2^2} \tag{6.1}$$

Peak 1 is a bulk low-energy plasmon. It is present at a frequency at which a zero of ε_1 occurs and ε_2 is small [6,90]. However, it is not a simple Drude-type collective excitation of the free electrons in the sp band, otherwise the plasmon would occur at the plasmon frequency ω_p, which is estimated at 9.2–9.5 eV [91,92]. The origin of peak 1 is the interplay of the free-electron plasmon resonance and the lowest strong optical absorption band, this later corresponding to the onset of transitions from occupied d states to empty states above the Fermi level [63]. Peak 2 occurs as a consequence of a very small value of ε_1. It results from an interplay between a free-electron plasma resonance, a strong absorption peak at 4–5 eV and higher lying optical bands. Even if peak 2 is quite broad, the small value of ε_1 allows to classify this peak likewise as the plasmon peak. ε_1, ε_2 and the loss function in the energy ranges 0–15 eV where peak 1

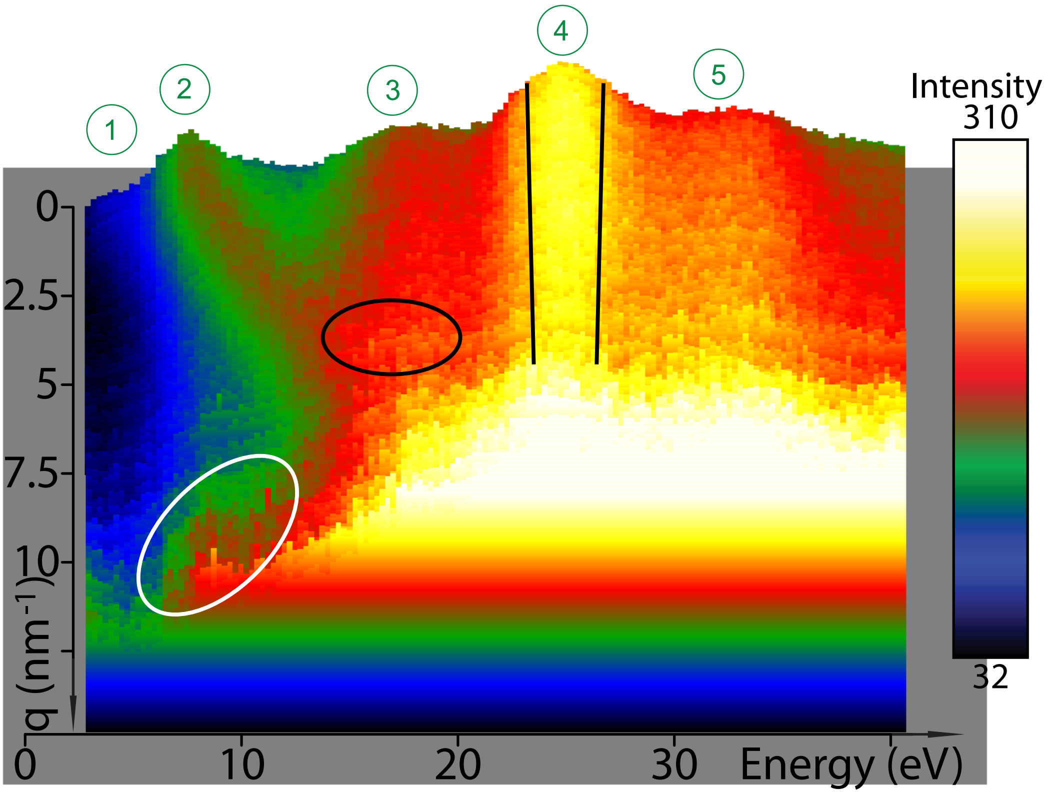

Figure 6.8: 3D representation of the map shown in Figure 6.5. The map is cropped to match the theoretical data in q shown in Figure 6.7. The energy range is from 2.75 eV to 40.25 eV. The intensity range is optimised for best visibility.

and 2 occurs are shown in Figure 6.9a. It is clearly visible in Figure 6.9b that each peak in ε_2 caused by the inter-band transitions from filled d states to those in the unoccupied manifold which yields a large Density Of States (DOS) has a corresponding peak in the loss function.

Figure 6.10 shows the overlap of the theoretical data (red line, calculated with a broadening corresponding to an energy resolution of 1 eV) and the experimental data (black line) for a selection of four different q for comparison. The agreement between the theory and the experiment is good, even if the intensity of peak 2 is systematically lower and the intensity of peak 4 systematically higher in the theory. The mismatch grows with increasing q for peak 3 where the agreement is growing for peak 5. For $q = 12.50\ \mathrm{nm}^{-1}$, all peaks disappear in the background curve, consolidating the statement that the comparison between the theory and the experiment is limited in q to this value.

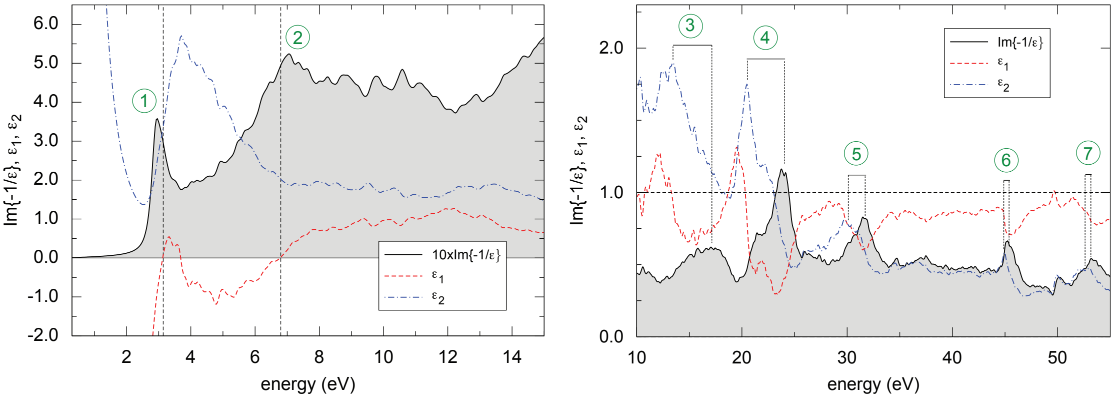

(a) Range 0–15 eV

(b) Range 10–55 eV

Figure 6.9: ε_1, ε_2 and the loss function calculated in the energy ranges 0–15 eV (a) and 10–55 eV (b) for bulk Ag, using a broadening of 0.1 eV. In (a), the loss function has been multiplied by 10 for better visibility.

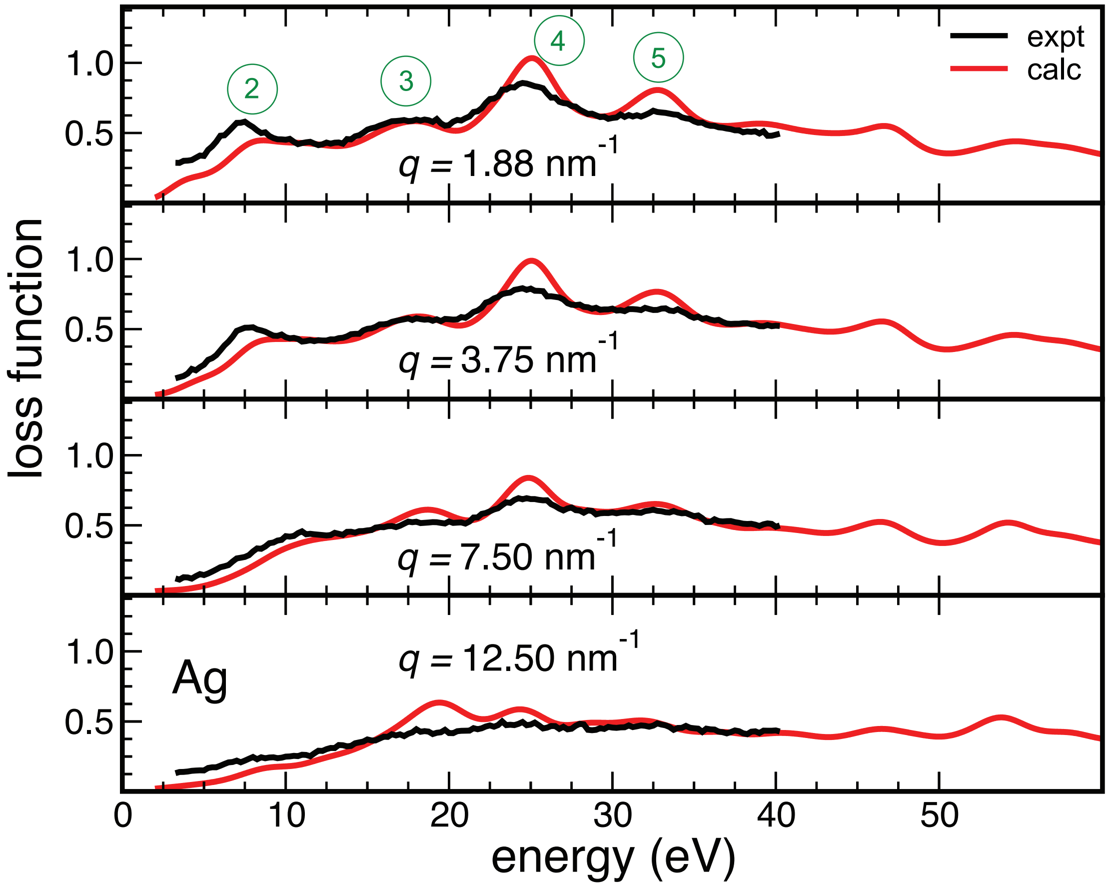

Figure 6.10: Comparison between the theory (red line) and the experimental (black line) data for some selected q. Peaks 2–5 are easily recognizable for low momentum transfer and vanish with increasing q.

6.2.1 Directional integration

So far in this section, theoretical data were calculated along the [111] direction, whereas the experimental data has a [001] zone axis and is integrated over a circle, thus contains everything within the $xy0$ plane. Recently published calculations [93] shown in Figure 6.11, present a slight difference in the loss function in different high-symmetry directions with increasing momentum transfer for silver. In order to determine if this difference is also detectable experimentally with EFNBED, a directional integration routine has been implemented.

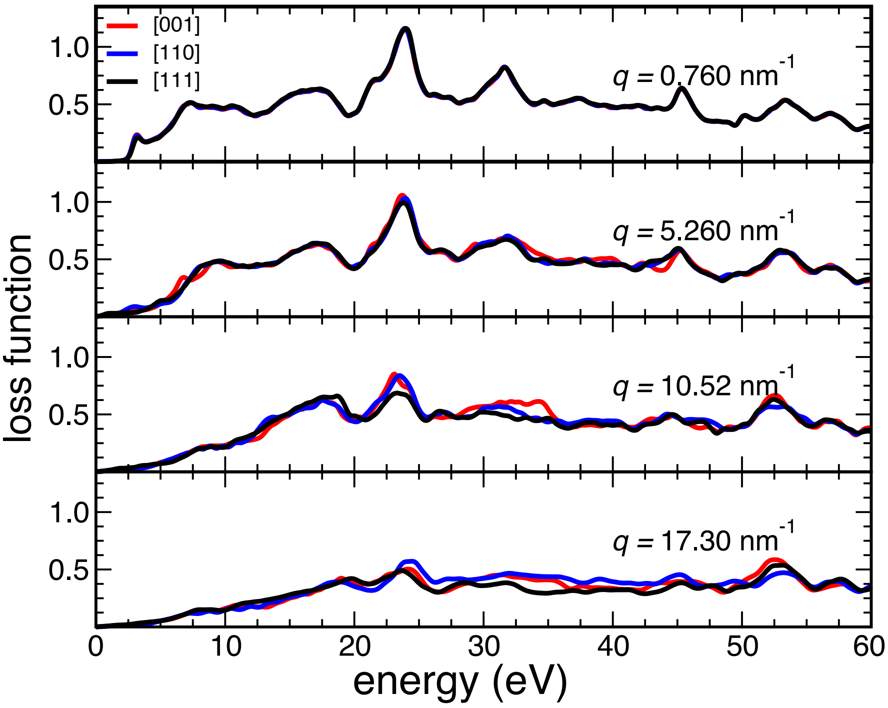

Figure 6.11: Loss functions of Ag for different momentum transfers along high-symmetry crystallographic directions.

The directional integration script DirectionalIntegration.s (which can be found in appendix D) calculates a q-EELS map starting at the transmitted beam spot of the diffraction pattern (determined automatically as the brightest pixel in the most intense slice) in four directions. The four directions are calculated from a single (x, y) coordinate entered by the user. Figure 6.12b shows an example of the analysis area determined by the position (36,500) which is the coordinate of the lower left $\bar{2}\bar{2}0$ diffraction spot in Figure 6.12a (the position of the peaks may be determined by the FindPeakPositions.s routine described in Appendix D). The red, green, blue and yellow trapezoids are the regions from where the information is picked out and summed. The trapezoids have a height determined by the user (in pixel size) and the width is proportional to the distance of the transmitted beam with a ratio 3/40. This may be adjusted in the script, but there is a trade off between angular resolution and the signal to noise ratio.

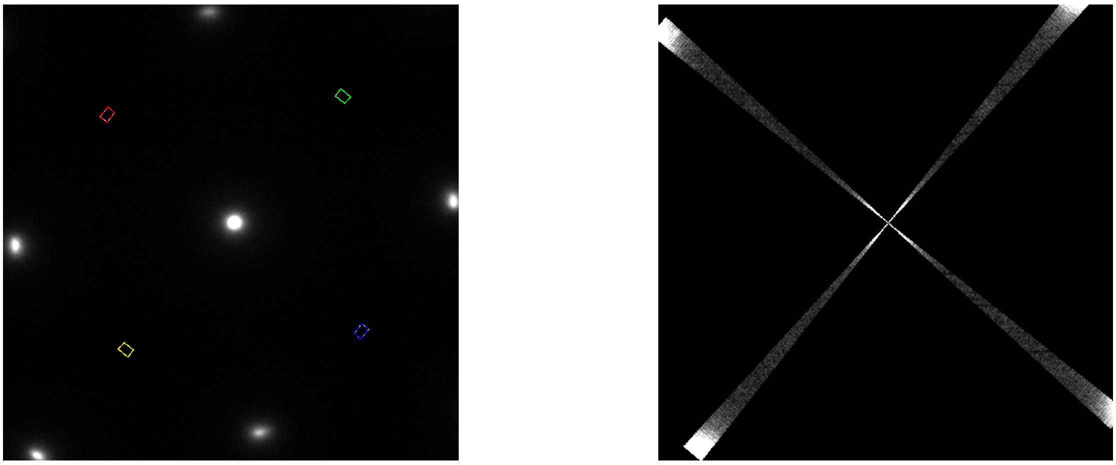

(a) EFTEM diffraction stack

(b) Analysed area in the 220–group direction

Figure 6.12: Example of the analysed area with the directional integration routine towards the lower left $\bar{2}\bar{2}0$ diffraction spot. The red, green, blue and yellow trapezoids are the zones from which the information is taken out.

Once the map is constructed, the Batson correction and the angular distribution correction are applied. The user is asked to enter the "direction" of the analysis at the end of the calculation for the naming of the resulting map. An example of maps calculated towards the 200 – $\bar{2}00$ – 020 – $0\bar{2}0$ spots (referred hereafter as the 200–group) and the 220 – $2\bar{2}0$ – $\bar{2}20$ – $\bar{2}\bar{2}0$ spots (referred hereafter as the 220–group) is shown in Figure 6.13. In this figure, the two maps are not of the same size, since the distance between the transmitted beam and the first spot is in ratio $\sqrt{2}$ for 220–group with respect to 200–group.

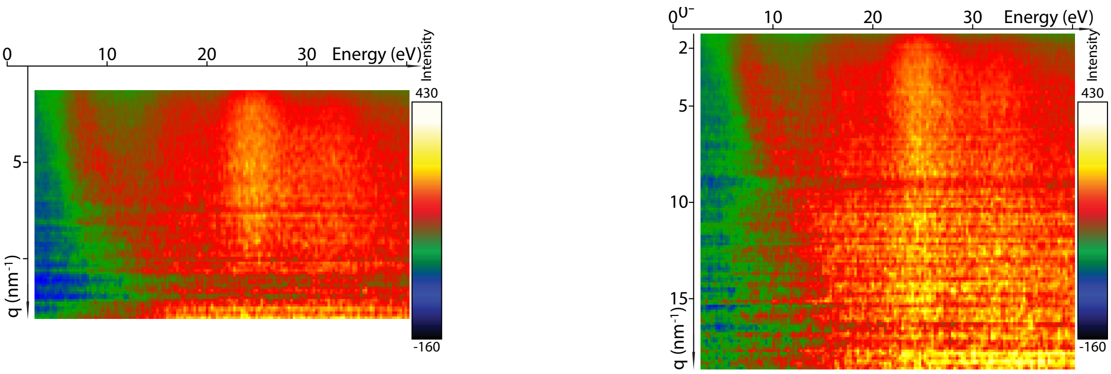

(a) Directional 200–group integration of [001] silver

(b) Directional 220–group integration of [001] silver

Figure 6.13: q-EELS map calculated with directional integration. The energy range is from 2.75 to 40.25 eV with a step of 0.25 eV. The angular momentum range is $q = 1.26\,\mathrm{nm}^{-1}$ to $q = 13.19\,\mathrm{nm}^{-1}$ for (a) and $q = 1.26\,\mathrm{nm}^{-1}$ to $q = 18.66\,\mathrm{nm}^{-1}$ (b), both with a step of $0.126\,\mathrm{nm}^{-1}$.

The comparison between the results from the radial and the directional integration respectively shows similar maps with an easily recognisable inter-band transition at 25 eV and the almost parabolic shaped dispersion of peak number 2. As in the radial integrated map, starting on $q = 12.5\ \mathrm{nm}^{-1}$ for the 200–group integration map and $q = 12.5\sqrt{2} = 16.67\ \mathrm{nm}^{-1}$ for the 220–group integration map, some contribution from the diffraction spot starts to alter the data.

Figure 6.14 shows the subtraction of the cropped 220–group map from the 200–group map. Since no clear structure is visible, one can conclude that the difference of energy loss depending on the high symmetry direction predicted by the theory is clearly below the experimental detection limit. Therefore, the experimental over a circle integrated data containing everything within the $xy0$ plane is compared with calculations done along the [111] direction, which is the most comprehensive data set yet calculated.

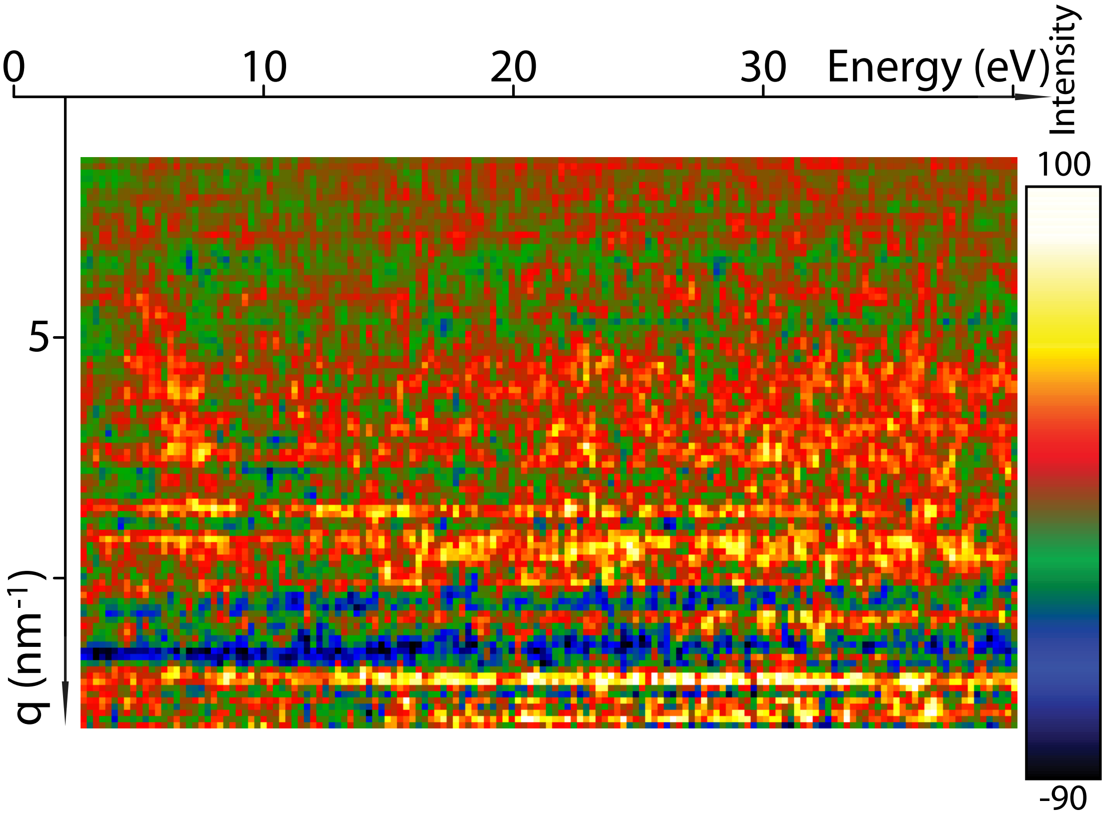

Figure 6.14: Difference between the 200 and the cropped 220 map. From this map, it is obvious that the difference between the two directions is below the actual experimental resolution.

The analysed region in the band structure of silver in the present section is represented in Figure 6.15

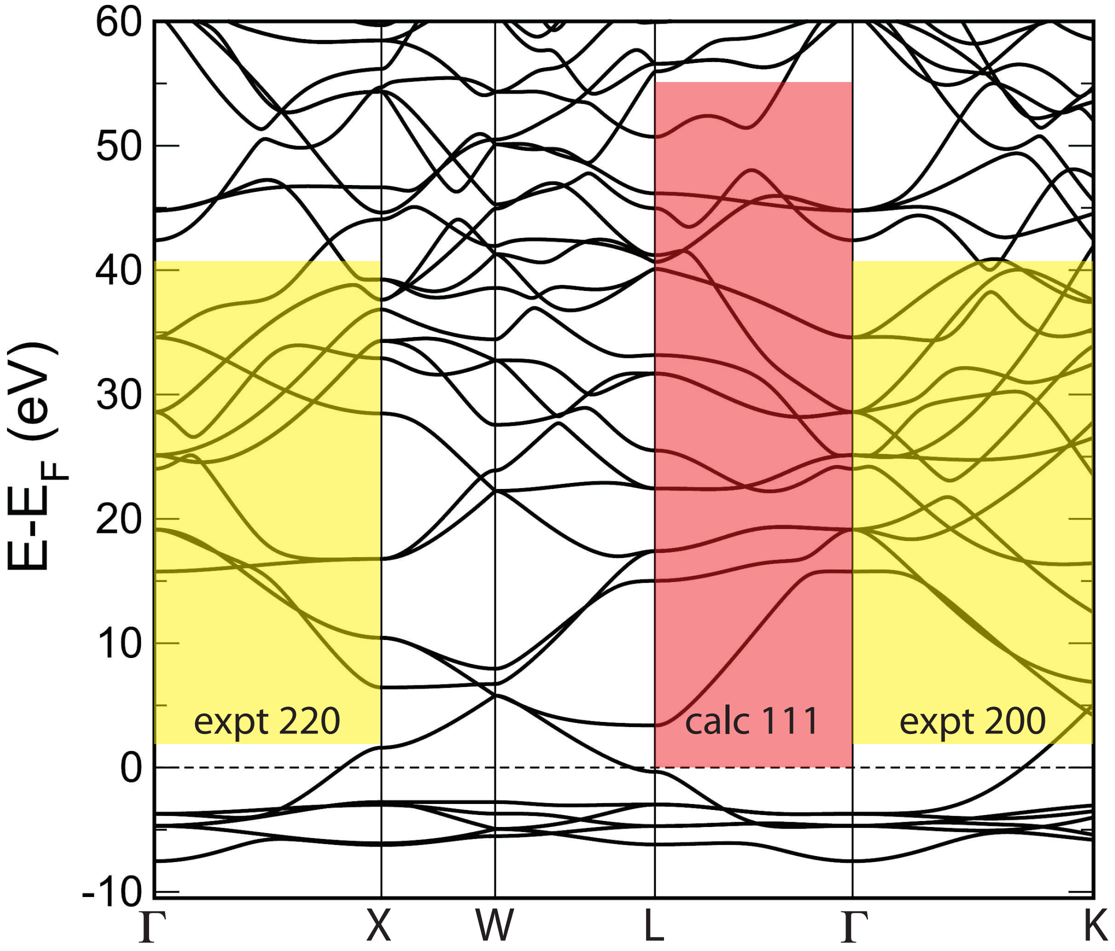

Figure 6.15: Band-structure of silver, where the red region corresponds to the analysed region by theoretical calculations and the combination of the two yellow areas the regions covered by the experimental data.

6.3 Comparison with other experimental data

The plasmon peak 1 has been extensively studied by different groups (*e.g.* [90,94–98]). However, since this peak is not visible in the experimental data presented in this work, no comparison will be performed.

The low-loss region up to 25 eV of silver has been studied for over four decades at $\boldsymbol{q} = \mathbf{0}$ (optical data, *e.g.* [99–103]) as well as momentum transfer resolved [92, 104, 105]. A selection of different works is presented hereafter and the data presented in this chapter compared to it.

Otto and Petri measured the plasmon dispersion and the $d \rightarrow f$ extended fine structure of silver in 1976 [104]. The specimen were polycrystalline silver films of different thicknesses, 43 nm in the case of the data reproduced in Figure 6.16a. The beam energy was set to 25 keV. The spectrum analyzer was based on a Hartl type filter lens [106], with which an energy resolution of 0.8–1.0 eV and an angular resolution of 0.25 nm^{-1} was achieved. The lateral resolution of their microscope setup is not specified.

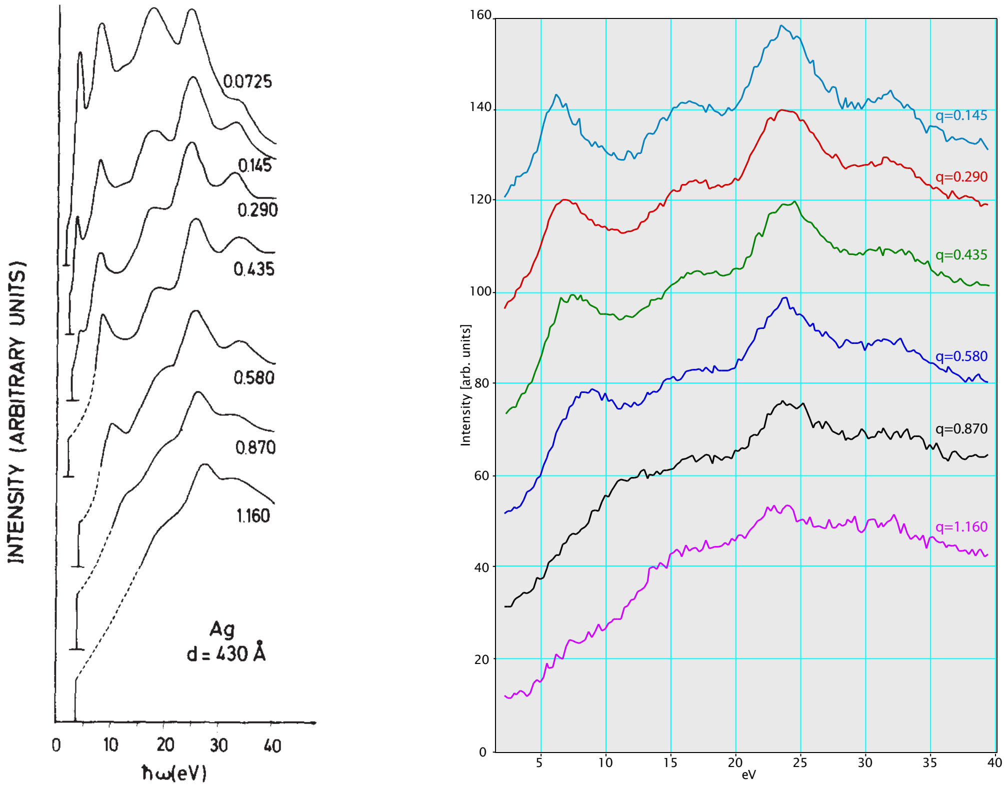

(a) Data from Otto and Petri

(b) Data of this work corresponding to those from Otto

Figure 6.16: Reproduction of the momentum transfer resolved loss spectrum from Otto and Petri [104] (a) and corresponding spectra of this work (b). The spectra are normalized with respect to the peak at 25 eV and shifted for clarity. The dashed part in the spectra of (a) correspond to multiple scattering which is not drawn for clarity. The momentum transfers are given in Å^{-1}.

The spectrum at $q = 0.725$ nm^{-1} is not drawn in Figure 6.16b since the setup of the microscope used for the acquisition of the data presented in this section does not allow a value of q that close to the transmitted beam (a new acquisition with a higher camera length would be necessary). All the other spectra are drawn and reproduce very well the features shown by Otto and Petri. The only slight discrepancy is visible at the second plasmon peak 2 at $q = 1.45$, which is higher in the data presented in this work.

Schöne *et al.* performed a theoretical and experimental study of the dynamical electronic response of silver [105]. The experimental data was acquired at 200 keV on a GIF operated in spectroscopic mode. The sample was a single crystal oriented in the [110] zone axis, prepared by polishing and ion-milling. The diffraction pattern was moved over the entrance aperture of the energy filter to select the desired momentum transfer $\boldsymbol{q}$. The spectra were multiple inelastic-scattering corrected via the Batson method up to momentum transfer $\boldsymbol{q} < \frac{\boldsymbol{G}}{2}$. The resulting data is represented as solid lines in FIG. 5. of [105] (as well as Fig. 1. in [107]). This data is reproduced in Figure 6.17a, where q is in units of $\frac{2\pi}{a}$ with the lattice parameter $a = 4.09$ Å for silver. The energy resolution is not mentioned in the publication.

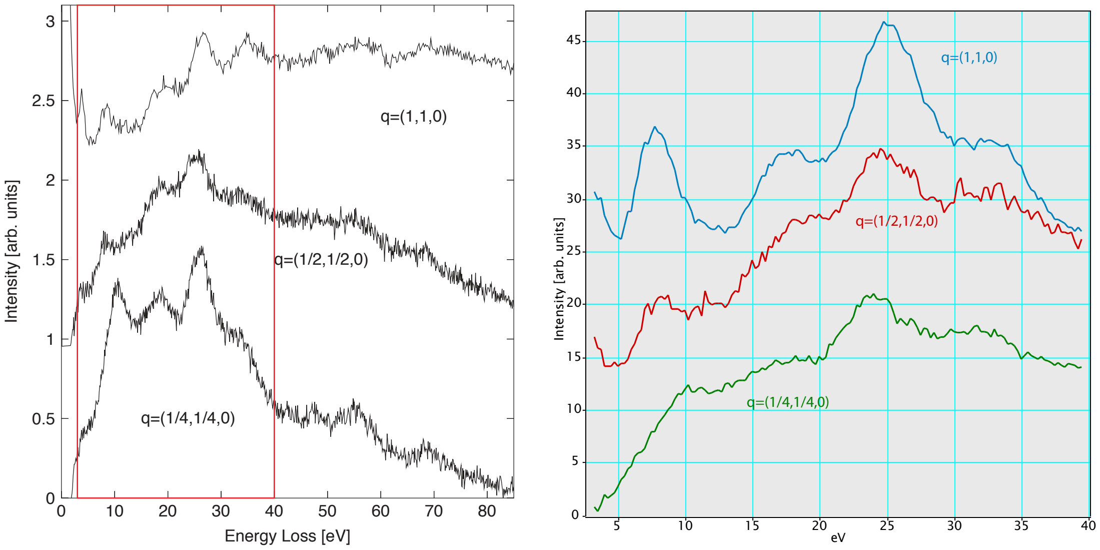

(a) Data from Schöne *et al.*

(b) Data of this work corresponding to those from Schöne *et al.*

Figure 6.17: Reproduction of the momentum transfer resolved loss spectrum from Schöne *et al.* [105] (a) and corresponding spectra of this work (b). The red square in (a) corresponds to the energies covered by the data presented in this work. The spectra in (b) are normalized with respect to the peak at 25 eV and shifted for clarity. The units of q are $\frac{2\pi}{a}$.

Compared to the data of Schöne *et al.* , the relative intensities of peak 2 do not agree in the case of $\boldsymbol{q} = (1/4, 1/4, 0)$, good agreement occurs in the case of $\boldsymbol{q} = (1/2, 1/2, 0)$ and there is a discrepancy in the height of peak 2 in the case of $\boldsymbol{q} = (1/2, 1/2, 0)$. Schöne *et al.* conclude their publication by claiming a disagreement in the relative heights of the peaks and the drop-off at high energies (higher than 60 eV) in their experiment with respect to their calculations. The comparison shown in the previous section also show a discrepancy in the relative peak height, but less pronounced than in the work of Schöne *et al.*

Recently, Werner *et al.* measured the optical constant of silver and gold [103] using Reflection Electron Energy Loss Spectrometry (REELS). A data analysis approach has been reported in 2006 [101, 108], where the deconvolution method consists in cross-convolute two spectra acquired at high difference in beam energies (5 kV and 40 kV respectively). Werner and coworkers managed with this method, which requires a relatively heavy data treatment, to extract the dielectric function ε. Thanks to REELS, an energy resolution better than 0.5 eV is achievable. Therefore, it has not only been determined that the plasmon peak 1 at 3.8 eV in silver can be decomposed into a contribution of a surface excitation at 3.7 eV and a bulk excitation at 3.9 eV, but also a very precise loss spectrum, shown in Figure 6.18a has been measured.

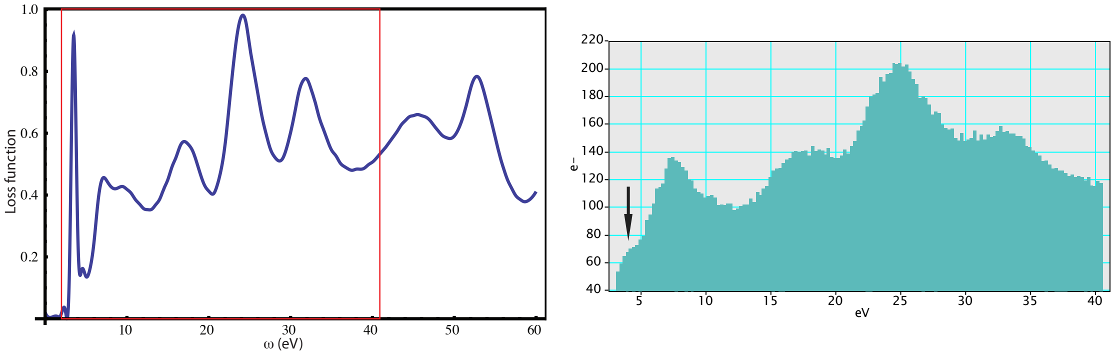

(a) Data extracted from Werner *et al.*

(b) Data of this work corresponding to those from Werner *et al.*

Figure 6.18: Reproduction of the loss spectrum measured with REELS by Werner *et al.* [103] (a) and corresponding spectrum of this work (b). The red square in (a) corresponds to the energies covered by the data presented in this work. The arrow in (b) show the energy of 3.8 eV which corresponds to the narrow plasmon peak 1.

The comparison between the REELS spectrum from Werner *et al.* and a spectrum close to $q = 0\ \mathrm{nm}^{-1}$ from the data presented in this chapter shows that except the extremely narrow peak 1 which is only visible as a weak edge (the arrow indicates the position 3.8 eV), the relative intensities of the peaks are in good agreement. A broadening of the peaks is clearly visible, which is due to the energy resolution of 1 eV instead of maximum 0.5 eV for the REELS data.

6.4 Conclusion

The experimental data presented in this work are in good agreement with theoretical calculations [63] as well as previous angular resolved EELS data of silver [104, 105] and optical data obtained with reflection EELS [103]. The spatial resolution is not mentioned in the publications cited here, thus no comparison can be performed.

Compared to Otto and Petri, the energy resolution of 0.8–1 eV is also achieved with the presented method. The angular resolution of $0.25\ \mathrm{nm}^{-1}$ with an beam energy of 25 keV cannot be achieved with the JEOL 2200 FS at 200 keV, limited by the lens and filter aberrations to $0.5\ \mathrm{nm}^{-1}$. The energy resolution of 0.5 eV obtained with REELS by Werner *et al.* may only be achieved with a monochromated microscope.

7 Conclusions and outlook

7.1 Conclusions

In this work, I have presented a reliable experimental and analytical technique to retrieve the momentum transfer resolved single scattering distribution at low energy losses with good accuracy. The energy resolution of the final angular resolved EELS data map is limited by the energy resolution of the microscope, as well as by the width of the energy selecting slit. This is also the limiting factor in the investigations at very low energies, especially in the infrared region (less than 1 eV energy loss). Nevertheless, the 1 eV energy resolution of the JEOL 2200 FS was good enough to compare semi-quantitatively the experimental results with *ab initio* calculations obtained within the time dependent density functional theory and Bethe-Salpeter equation. This comparison has been made with theoretical calculations by A. Alkauskas that used the random phase approximation [63]. Further comparisons with experimental data from Otto and Petri [104], Schöne *et al.* [105] in TEM and Werner *et al.* [103] with REELS also show good agreement.

Several optical alignments and operational modes of the JEOL 2200 FS have been tested, and finally nano-beam diffraction was found to be the optimal running mode. Our work provides for the first time a full 3D energy loss data cube in diffraction mode with energy and angular resolutions of 1 eV and 0.5 nm^{-1} respectively. After processing, the energy and angular relevant data span an energy loss range from 2.75 eV to 40.25 eV and the angular momentum transfer up to 12.5 nm^{-1}. Although theoretically, without CCD camera binning and the maximum available camera length of the JEOL (250 cm), a momentum transfer resolution of 0.04 nm^{-1} would have been possible, the effective angular resolution was limited by the smallest obtainable beam convergence as well as by the remaining aberrations of the microscope.

The energy range of the presented data set (2.75 eV to 40.25 eV) has been obtained with a sampling step of 0.5 eV. Within this work, the absolute lower limit of the accessible energy range on the JEOL 2200 FS installed at CIME has been reached. This limit is determined by the resolution of the microscope since the tails of the ZLP hides the signal at very low energy loss. The higher energy limit may be chosen arbitrarily high, considering a software limit (the DigitalMicrograph version installed on the JEOL at CIME is limited to data cubes of ~ 750 Mo memory size in practice). Making the slit width narrower than $\delta E = 0.5$ eV only results in an oversampling, the microscope having an energy resolution of ~ 0.8 eV.

The presented technique can be reproduced on any transmission electron microscope equipped with an in-column energy filter. The critical alignments are the parallelism of the beam in NBD mode and the correction of the non-isochromaticity of the filter. As the acquisition time of a single data cube is large (approximatively 1.5 hours), the stability of the microscope and its environment are also critical. In this aspect, the in-column Ω filter of the JEOL 2200 FS is of great advantage as its energy stability is much higher than that of a post-column filter. Furthermore, it has been demonstrated that the proposed method provides working ranges in energy, spatial and angular resolution limited only by the performance of the microscope. Previous techniques did not provide experimental results showing an energy resolution independent of the spacial and angular resolutions.

7.2 Outlook

While the directional analysis method is limited to square diffraction patterns (*e.g.* for the analysis of [001] oriented single cubic crystals), the script could easily be adapted to other symmetries. It is possible to increase the number of scanning sectors (if necessary) and to change the scanning angle between these areas in order to increase the possibilities of diffraction pattern scanning. A much more evolved script may have the possibility to ask for the crystal structure and the zone axis, and perform the subsequent analysis in all directions of interest.

The limitation of the lateral resolution on the specimen is directly linked to the condenser lens optics and the size of the condenser lens aperture. Technically, the presented method is suitable for any selected condenser lens aperture. In this work, the CLA3 with a diameter of 40 μm has been used, giving an illuminated area of about 220 nm in diameter. The CLA4 (with a diameter of 10 μm) has been tested, giving an illumination area with a diameter of 50 nm. However, working with this aperture is almost impossible, since most of the electrons of the incident beam are blocked and thus the signal to noise ratio is much too low. An intermediate condenser aperture (20 μm) would probably be a good compromise. Using another microscope which allows higher intensities in the nano-beam mode with a small condenser lens aperture would also improve the lateral resolution.

In section 5.5, it was shown that the data acquisition method using imaging plates suffers from issues related to the IP's non-isotropic background and the variable sensitivity of the photostimulable layer from plate to plate. However, two investigation ideas are also mentioned to overcome these issues: the first method proposes to illuminate all plates used for acquiring the data set with a reference beam (which should be absolutely constant over the whole period of marking the IP's for best accuracy) which would then allow calibration of the plates individually, and the second method suggests using a noisy data set acquired with the CCD camera to calibrate the plates and then to use the reconstructed stack to extract the data from the IP's. Even if the imaging plates system developed in the early sixties is primitive, the much higher dynamic of the plates allows a better signal to noise ratio than a CCD camera, increasing the precision and the clarity of the resulting data. However, the improvement of electron detection devices could make the use of imaging plates obsolete. This year, an improved CMOS detector has been released by Gatan: the K2™ series (http://www.gatan.com/products/digital_imaging/products/K2/index.php). It is a 4k × 4K Direct Detection camera (doing an electron to electron conversion, opposed to the traditional CCD cameras performing an integration of the analog signal obtained by an electron to light conversion) which makes it much more sensitive, has a higher read-out rate, and even more important in the frame of this work, has a much higher dynamic range and a much higher intrinsic signal to noise ratio than the CCD camera. The access to a higher dynamic range is possible via summation of frames (realizable because of the fast readout, where a conventional CCD needs approximatively 2 s).

In the last years, the development of monochromated transmission electron microscopes has improved energy resolution to below 100 meV. With such an energy resolution, it is probable that applying the method presented in this work would not only allow investigation of the infrared region, but also to get an angular resolved EELS data set of such unprecedent accuracy that it makes the comparison with theoretical calculation straightforward at any energy with enough precision to move forward in theoretical modeling.

A Silver sample preparation by twin jet polishing: tables of technical data

A.1 Phosphoric acid

Table A.1: First chemical thinning with phosphoric acid, 20.02.2009.

# attack	T1 [s]	Flux 1	T2 [s]	Flux 2	Result
1	120	35	124	44	Two holes and probable surface contamination
2	600	35			Strong yellow contamination
			16	?	Small hole without contamination, except under the support (sample edge); hole edge absolutely rough (topographically)

Remark: For this day, the temperature was kept at 20.5°C, the cathode was Al 40 μm prepared by Danièle Laub[1], the tension fixed at 25 V, giving a resulting current of 10–14 mA.

Table A.2: Second chemical thinning with phosphoric acid, 05.03.2009.

# attack	Cathode	Tens [V]	Temp [°C]	Crt	T [s]	Result
3	Al 150 μm	40	23	272	9	Did slab move? Cathode and sample are black!
4	Al 150 μm without ring	40	23	362	16	Cathode and sample are black.
5	Pt 170 μm	40	23	362	16	Cathode is OK, sample was attacked at the edge, $\varnothing < 2$ mm; Pt cathode method is discarded.
6	Al $\tilde{8}0$ μm	40	20.5	288	8	Cathode OK, sample got holes at the edge, center is yellow.
7*	Al $\tilde{8}0$ μm	40	20.5	362	9	A big gray slimy thing (too big for being silver particles) appeared on the cathode; sample is dirty but intact.
8*	Al $\tilde{8}0$ μm	30	20.5	9–13	171	Sample attacked at the edge, a crust appeared in the middle; cathode OK.

Remark: For this day, the flux has been kept at 35.
* Sample has been washed with nitric acid 50% during one minute and cleaned in ethanol before thinning.

---

[1] Danièle Laub, technical employee, CIME, EPFL.

A.2 Perchloric acid

Table A.3: First try of Cockayne *et al.* solution using perchloric acid after nitric acid, 16.07.2009.

# attack	Tens [V]	Temp [°C]	Crt	T [s]	Flux	Result
1	40	20	?*	15	25	Huge hole. The sample is a 0.1 mm thin ring.
2	20	20	?*	1	18	"crater", has to be checked in a TEM.
3	20	12.5	?*	2	18	Rough without any hole. Sample moved → is it too thin?

Remark: For this day, the cathode was Pt 170 μm.
* There was no time for the machine to get a current signal...

Table A.4: Second try of Cockayne *et al.*, only using the perchloric acid solution, 17.07.2009.

# attack	T [s]	Flux	Result
4	176	23	Promising. 4 holes, grains are well visible, small brown stains present → low tension ion bombarding necessary?
5	126	23	Half-moon hole and small brown stains.
6	200	10	Nice hole, small stains.

Remark: For this day, the temperature was between 40.2 and 40.6°C, the cathode was Pt 170 μm, the tension was fixed at 20 V, giving a current response oscillating between 10 and 12 mA each time.
The sample have been washed (deoxidized) with nitric acid 50% and cleaned with CH_3OH before electropolishing.

A.3 Sulfuric acid

Table A.5: Electropolishing results using Lyles *et al.* mixture based on sulfuric acid. Three polishing sessions have been performed: EP 1–5 on 26.11.2009, EP 6–9 on 27.11.2009 and EP 10–15 on 22.01.2010.

# attack	Tens [V]	Temp [°C]	Crt	T [s]	Flux	Thick [μm]	Result
1	9	21	16–22	164	6	200	Small hole, thick edges; surface more or less smooth, slightly strained.
2	9	20.3	22–36	156	6–10	200	Flux "ramp", change after 10”; similar result.
3	9	20.3	24–30	151	13	200	Similar result, strains more pronounced.
4	9	20.3	26–38	165	1	200	Similar result than attack #1.
5	9	20.3	20–36	266	6	300	Sample pre-polished with paper, without HNO_3; Hole sharp, thick edges, strongly strained.
6	20.5*	20.8	32–64	191	6	300	Strongly strained, thick edges.
7	20.5*	20.5	24–55	242	1	300	Similar result.
8	20.5*	12.2	12–36	449	1	300	Similar result with dirty edges.
9	9	12	20–32	450	13–10	300	Mode "ramp", change after 60”; similar, less strains.
10	9	20	0	0	13–10	100	Bug with the Tenupol, sample attacked, no hole.
11	9	20	14–16	109	13–10	100	Similar result with much less strains.
12	9	20	18–14	98	13–10	100	No HNO_3 used; sample much less shiny.
13	9	20.3	10–9	80+5	13–10	100	Cleaning during 5”; No hole; sample will be finished with IBT.
14	9	20.3	10	80+5+5	9–5	100	Cleaning during 35”; EP stopped when light reaches 20; sample clean and shiny.
15	9	20.3	22	5	13	200	EP3, trying to increase the hole; doesn’t work.

Remark: The cathode was Pt 170 μm. This is the first time samples thicker than 100 μm have been used.
Remark: If not specified, the sample have been deoxidized in nitric acid (33% on 26.11, 50% afterwards) and cleaned with CH_3OH before polishing.
*: The machine can automatically seek for the "plateau", which gives here an optimal tension of 20.5 V.

A.4 Synthesis of all sulfuric acid techniques

Table A.6: Comparison of H_2SO_4 electrolytes preparation for Ag 99.999%.

	Lyles *et al.*	**Sigle *et al.***	**CIME**
Mix (in order)	glacial AcOH* conc. H_2SO_4 MeOH+Thiourea**?	glacial AcOH* conc. H_2SO_4 MeOH+Thiourea**	glacial AcOH* conc. H_2SO_4 MeOH+Thiourea**
Cooling	ice	LN in electrolyte	ice (bath)
Note	solution lasts for 20–30 samples; discard when elemental sulfur precipitate	Shake for long time; if still some Thiourea, it doesn't matter	It takes a long time until Thiourea is dissolved
Storage	not specified	room temperature; keep bottle cap only gently screwed (avoid overpressure)	in safety refrigerator
Sample	⌀ 3 mm; 50 μm thin lamellas	not mentioned	⌀ 3 mm; 100, 200 and 300 μm thick lamellas, previously cleaned with HNO_3
Polishing	@9V: removes 200 nm/sec		Several atempts
Cathode	Platinum		Platinum
Control	several observations during polishing process		wait until polishing is finished
Washing	CS_2 followed by anhydr. MeOH		anhydr. MeOH
Results	15–20 μm flat area	nice results; works well	no thin areas
Remark	H_2O rinsing causes a distinct etching of the surface; not enough Thiourea engender a faceting of the surface (too much doesn't matter)		Preferential attack on grain boundaries?

*: Glacial acetic alcohol (CH_3COOH), "glacial" standing for pure, anhydrous.
**: Thiourea ($(NH_2)_2CS$).

A.5 Sample preparation devices

A.5.1 Ion milling devices

Two different ion milling devices have been used for this work: an E.A. Fischione Instruments, Inc. **1010**® Ion Mill® instrument (http://www.fischione.com/products/model_1010.asp) as well as a NVision 40 CrossBeam® FIB from Carl Zeiss SMT AG.

The Fischione 1010 has two position fixed HAD ion sources which are independently operable from 0.5 to 6.0 keV. The mill angle can be adjusted between 0° and 45°. Milling is possible either under an argon atmosphere (inert) or under a reactive gas atmosphere (thus interacting with the sample while milling).

The FIB beam is produced by using ions from a gallium source, accelerated between 5 and 30 keV. With this beam, a thin lamella (the sample) is cut out of the bulk, lift out with a needle (usually made out of tungsten) and welded on a FIB lift-out TEM grid (*e.g.* http://www.tedpella.com/grids_html/4510half.htm). More details on this method can be found *e.g.* in [109] or [110]. Almost all kind of material can be prepared with this method. Another method for FIB sample preparation, the so-called "H-bar" method, consists in milling directly a thin layer of the specimen into the bulk material [57, 58].

A.5.2 Electropolisher

The CIME is equipped with a TenuPol-5 (Struers, http://www.struers.com) Twin Jet Electropolishing device. The TenuPol-5 is a dedicated TEM-sample preparation system. It allows a simultaneous electrolytic thinning from both sides of the sample to avoid damages. Furthermore, it has an automatic shut-off function which stops the thinning process as soon as a hole appears (thanks to an infra-red detection system). It has also a scan function, allowing to determine the correct polishing voltage. If the sample is very thick, it is also possible with the TenuPol-5 to pre-thin it electrolytically (thus avoiding mechanical deformation).

A.5.3 Plasma cleaner

The plasma cleaner installed in the sample preparation lab of the CIME is a Model 1020 from E.A. Fischione Instruments, Inc. (http://www.fischione.com/products/model_1020.asp). The plasma is generated in a high frequency oscillating field system coupled to a quartz and stainless steel plasma chamber. The ion energy is less than 15 eV and the gas is composed of 25% oxygen and 75% argon. The high vacuum of 10^{-6} Pa is created with an oil-free turbomolecular drag pump backed with a multi-stage diaphragm pump in order to have a dry and clean chamber. During the cleaning process, the pressure in the chamber is maintained at about 50 mTorr.

A.5.4 Nordiko

For this work, some silver samples have been prepared by sputtering in the ceramic laboratory of the EPFL. Sputtering was performed with a magnetron sputtering machine, NORDIKO 2000 (Nordiko Ltd, Havants, Hants, UK). 99.99% pure Ag target (from Kurt J. Lesker) was used for depositing the film. More details can be found in section 3.4.

A.5.5 PIPS

The 691 Precision Ion Polishing System™ (PIPS) from Gatan, Inc. (http://www.gatan.com/specimenprep/691_pips.php) has been used to clean samples which cannot be put into the plasma cleaner. Basically, the PIPS consists of two Penning ion beams with miniature rare earth magnets directed towards the sample. The energy (100 eV to 6.0 keV) and the angle of the beams with respect to the specimen (-10° to +10°) can be adjusted independently one from the other. The vacuum system of the sample chamber is identic to the one from the plasma cleaner, and pure argon at 144 kPa is used to produce the ion beam.

B Comment on diffraction notations

The scientific community could not agree on a single notation in diffraction: some people measure the "distances" as fractions of $\boldsymbol{G}_{hkl}$, some others in angles (θ mrad) and even others in fraction of Brillouin Zone (BZ). This appendix gives the relation between the different notations.

Figure B.1 gives the sketch of a point P at an angle θ_P of the transmitted beam 000 towards a diffraction spot hkl, which is located at an angle $2\theta_{hkl}$, linked to d_{hkl} via Bragg's law $\lambda = 2d_{hkl}\sin\theta_{hkl} \approx d_{hkl}2\theta_{hkl}$, where λ is the wavelength.

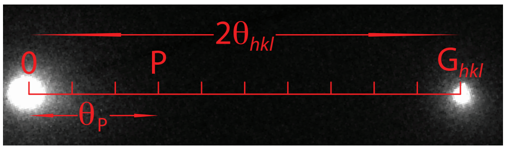

Figure B.1: The two different notations "P is at θ_P from 000 towards hkl" and "P is at $^1/_x$ from G_{hkl}" are equivalent.

From a vector point of view,

$$\boxed{\boldsymbol{OP} = \frac{1}{x}\boldsymbol{OG}} \tag{B.1}$$

The angular notation is found as follows: combining equations (4.2) and (4.3) leads to $\lambda \approx 2d_{hkl}\theta_{hkl}$, and since $\lambda = \frac{2\pi}{k}$ (where k is the wave number),

$$\theta_{hkl} = \frac{2\pi}{k}\frac{1}{2d_{hkl}} \tag{B.2}$$

The relation between the direct and the reciprocal space (the last one being indicated by *) is given by

$$d_{hkl} = \frac{2\pi}{d^*_{hkl}} \tag{B.3}$$

Thus, the angle θ_P is expressed as

$$\boxed{\theta_P = \frac{1}{x}(2\theta_{hkl}) = \frac{1}{x}\frac{d^*_{hkl}}{k}} \tag{B.4}$$

The first Brillouin zone is constructed as follows: lines are drawn from the transmitted beam to all the closest diffraction spots. The medians of all these lines correspond to the edge of the first Brillouin zone. If forbidden reflections exist, they have to be taken into account and the medians are to be taken on the line between the transmitted beam and the forbidden reflections if they are closest. Mathematically spoken, $\mathrm{BZ}_{hkl} = \frac{1}{2}d^*_{hkl}$. Combining this last expression with (B.4) gives finally

$$\boxed{\theta_P = \frac{1}{x}\frac{2\mathrm{BZ}_{hkl}}{k}} \tag{B.5}$$

In addition, when comparing data in θ or fraction of $\boldsymbol{G}$ with data shown as fraction of BZ limit, one should take care that often the first visible G is not a primary one. For example in fcc structures, 100 reflections are forbidden and the first G is 200.

C Microscope alignment

The alignment of the microscope is a crucial step before each use, in order to ensure the right beam path and subsequently the correct data acquisition. The alignment procedure used in this work is given hereafter (the numbers in brackets corresponding to the sections in the handbook of the JEM-2200FS):

Degauss The filter lens tends to grow a magnetic field by induction. It is important to degauss the filter at the beginning of each microscope session.

Condenser lens aperture Insert the desired CLA and center it: at about mag 10kx, center the spot while the beam is fully condensed, adjust the aperture position while the spot is over-focused (open the beam clockwise). Adjust the condenser stigmators approximatively with COND STIG.

Eucentric height Press STD FOCUS and adjust the specimen high: use IMAGE WOBB X and minimize the move with Z-shift.

Spectrum mode Neutralise PL, center the Spectrum ZLP (with FL shift and PLA-Y).

Gun shift Go to mag higher than 80kx. While Gun turned off, go to Spot 5 and center the beam with the SHIFT buttons. Switch to Spot 1, switch on Gun and center the beam with the SHIFT buttons. Repeat this sequence as many time as necessary.

Gun tilt (5.8.1) Click on Gun and Anode Wobbler (Alignment Panel) and make the movement concentric.

Pivot points (Tilt and shift purity, 5.8.3)

- In image mode, click on TiltX Wobbler (Alignment Panel) and unify the split beam with the Tilt compensator DEF/STIG X. Do the same for TiltY Wobbler.
- Put in an SAA (*e.g.* SAA2) and spread the beam fully. In diffraction mode, defocus the spot with DIFF FOCUS (clockwise) and correct the caustic with Il Stig (make the spot perfectly circular). Focus the spot again, click ShiftX Wobbler and unify the split spots with Shift compensator DEF/STIG X. Do the same for ShiftY Wobbler.

Beam tilt (Bright tilt "Voltage axis", 5.9.2) Go to mag 400kx ant press STD FOCUS, switch HT WOBB on and make the movement concentric with the BRIGHT TILT deflectors.
N.B.: Use TV cam for higher precision.
Other method: set mag to 200kx, find a recognizable feature and center it in DM. Turn HT on and make the feature stable. Or: make Live FFT circular.

Check eucentric hight

Correct condenser stigmators

Isochromaticity (5.12.7c) Neutralize isochromaticity and align it as mentioned in section 5.1.1.

Table C.1: Affected lenses during the alignment.

Button/knob	**Affected lens**
FL	$FLfine$
COND STIG	$CLStig$
OBJ STIG	$OLStig$
DARK TILT	$Cond1$ and $Cond2$
BRIGHT TILT	$Cond1$ and $Cond2$
IMAGE SHIFT	$Image1$
BRIGHTNESS	$CL2$
MAG/CAM L	all IL and $OLfine$ in image mode[1] all IL and $PL1$ in diffraction mode $PL1$ and $PL2$ in spectrum mode[2]
OBJ FOCUS	$OLfine$
DIFF FOCUS	$IL1$ in diffraction mode
PLA	$PL1$

The different alignment steps affect the lenses as shown in Table C.1.

Furthermore, the Ω filter may be aligned with following parameters (in brackets the affected lens): Achromaticity ($PL1$), FL S1 ($FLStig1$), FL S2 ($FLStig2$), FLA ($FLA2$).

The Isochromaticity affects the lenses in a complicated way, as the influenced lens changes depending on the magnification/camera length. Table C.2 gives the summary of the affected lens/magnification link. The non-isochromaticity has to be realigned each time when the working mode is switched from image to diffraction or inversely.

Table C.2: Affected lenses when changing Isochromaticity depending on the magnification (image mode) or camera length (diffraction mode).

Mode	$IL1$	$IL2$	$IL3$	$IL4$
Image	8'000 – 12'000	15'000 – 60'000	1'500 – 6'000	80'000 – 10^6
Diffraction	—	—	25 – 120 cm	150 – 250 cm

The switch between image and diffraction mode changes the behavior of following lenses: all IL, $FLA1$, $PL1$ and $Proj$, which is almost the full lens system after the objective mini-lens. The switch between TEM and NBD mode changes following lens currents: $CLStig$, $Cond1$, $Cond2$, $CL1$, $CL2$ and CM and $Spot$. This corresponds to the illumination lens system, before the specimen.

Since in electromagnetic lenses, the electrons rotate , it is not obvious in which direction the different apertures of the microscope move. Figure C.1 gives the directions for the JEOL 2200 FS at CIME in TEM mode with magnification higher than 8000x.

---

[1] The OM lens is off if the magnification is higher than 8000x.

[2] $PL1$ and $PL2$ change in the opposite direction: if the strength of $PL1$ is increased, the strength of $PL2$ decreases.

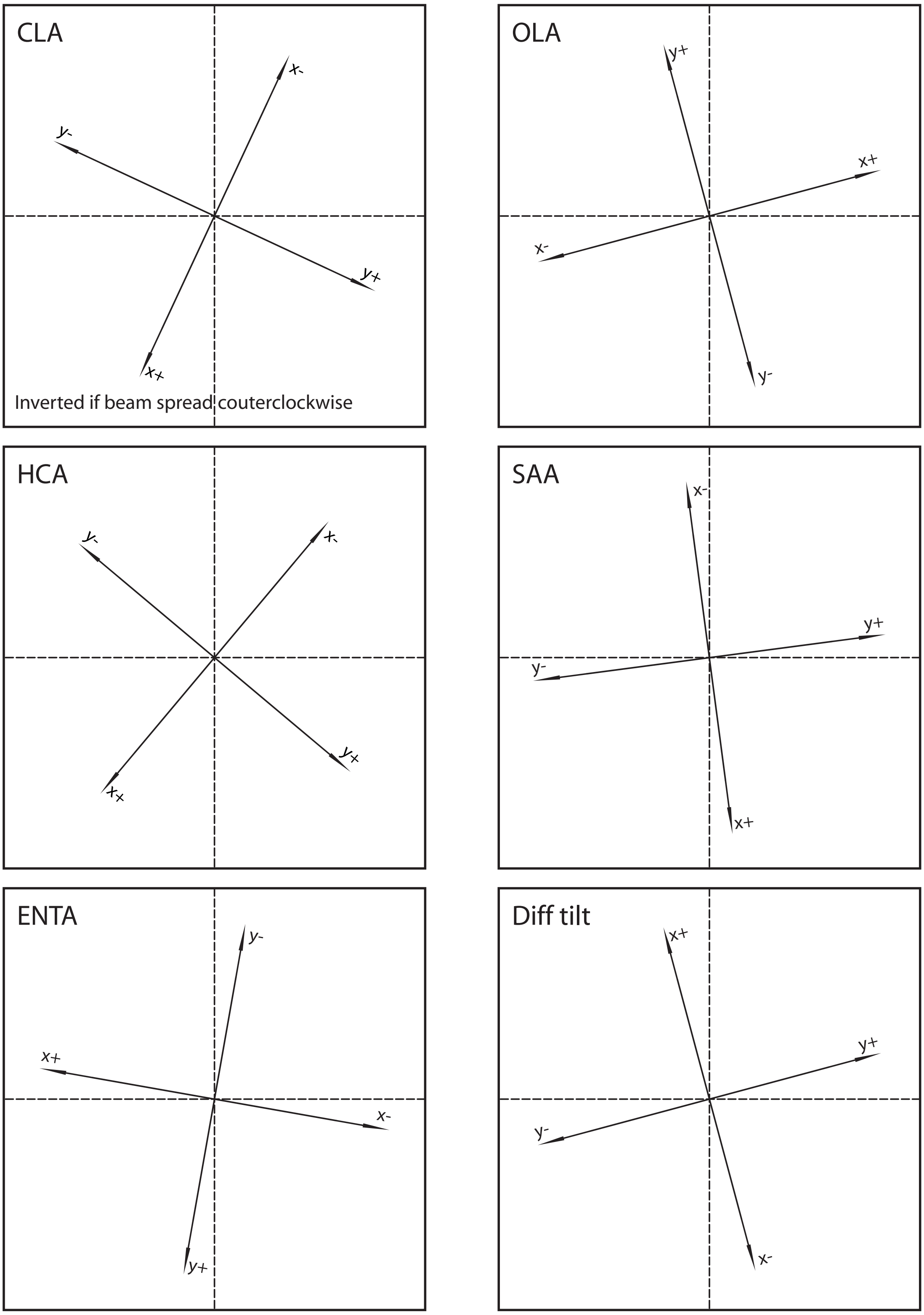

Figure C.1: Behavior of the apertures in the JEOL in TEM mode at a magnification higher than 8000x.

D DigitalMicrograph™ scripts

This appendix gives the source code for following DigitalMicrograph™ scripts used in this work: "FindPeakPositions.s", "RadialIntegration.s" and "DirectionalIntegration.s". DigitalMicrograph™ is an imaging software developed by Gatan, Inc. (http://www.gatan.com/imaging/dig_micrograph.php).

D.1 Find Peak Position

This script detects a number of peaks (defined by the user) in an image or a 3D stack above a certain threshold, and returns the coordinates of the brightest pixel in the spot. The threshold value is determined by the mean of the image increased by twice the quadratic mean. In the 3D stack, the most intense slice is determined before the peak analysis. The information is written in the "Result" window, as well as in the Image Info of the "Peak Analysis" image.

```
image front:=GetFrontImage()
string name=front.ImageGetName()

number xLength=front.ImageGetDimensionSize(0)
number yLength=front.ImageGetDimensionSize(1)
number zLength=front.ImageGetDimensionSize(2)

//******************* Functions ********************************

// Checking stack for highest peak position
number FindMaxPosition(image Img, number &TransmittedX, \
    number &transmittedY)
{
    number nx=Img.ImageGetDimensionSize(0)
    number ny=Img.ImageGetDimensionSize(1)
    number nz=Img.ImageGetDimensionSize(2)
    number k,valmax, z=0, newvalmax=0
    image slice
    for(k=0;k<nz;k++)
    {
        slice:=slice2(Img,0,0,k,0,nx,1,1,ny,1)
        valmax=Sum(slice)
        if(valmax>newvalmax)
        {
            max(slice,TransmittedX,TransmittedY)
            z=k
            newvalmax=valmax
        }
    }
    Return(z)
}

// Find maximum in image
number xmax, ymax, valmax
```

```
void FindMax(image img, number &xmax, number &ymax, number &valmax) \
    valmax=Max(img,xmax, ymax)

// Set threshold value for peak size
number SetPeakThreshold(image img)
{
    number temp
    number threshold=(mean(img)+(2*rms(img)))
    if(!(TwoButtonDialog("Threshold value for peak search is " \
    +threshold+". \
    Do you want to change it?", "No", "Yes")))
    {
        getnumber("Enter new threshold value", threshold, temp)
        threshold=temp
    }
    return(threshold)
}

// Mask a peak
number MaskPeak(Image Img, image &mask, number xmax, number ymax, \
    number valmax, number threshold)
{
    number size=0, cropxmax, cropymax, cropvalmax=valmax, count=0
    image crop:=Img.ImageClone()[ymax,xmax,ymax+1,xmax+1]
    while(cropvalmax>=threshold)
    {
        size+=10
        crop:=Img.ImageClone()[ymax-((size/2)+1), xmax-((size/2)+1), \
            ymax+(size/2)+1, xmax+(size/2)+1]
        crop=tert(iradius<(size/2)-1,0,crop)
        FindMax(crop, cropxmax, cropymax, cropvalmax)
    }
    number radius=size/2
    subarea zone:=mask[ymax-(radius+1), xmax-(radius+1), ymax+radius+1, \
        xmax+radius+1]
    zone=tert(iradius<radius,1,zone)
    Return(radius)
}

//******************* Main ************************************
```

```
// Generate mask with dimension of the input image
image mask=BinaryImage("Mask",xLength,yLength)

// Ask number of peaks
number PeakNumber
if (!getnumber("How many peaks to find?", 9, PeakNumber )) \
    Throw("Analysis aborted!")

number trash
number MaxSlice=FindMaxPosition(front,trash,trash)

Result(DateStamp()+" Most intense slice is #"+MaxSlice+"\n")

number nx=xLength, ny=yLength
number i, Xboundary=nx/5, Yboundary=ny/5, test, threshold= \
    SetPeakThreshold(front), oldnx, oldny, tempx, tempy
image original=Slice2(front,0,0,MaxSlice,0,nx,1,1,ny,1)
string PeakString=("Most intense slice is #"+MaxSlice+"\n")

PeakString+=("Threshold at "+threshold+"\n")

Result("Start searching "+PeakNumber+" maxima; threshold = \
    "+threshold+"\n")
for(i=0;i<(PeakNumber);i++)
{
    // Find maximum and check if above peak threshold or near image
    // boundary
    FindMax(!mask*original, xmax, ymax, valmax)
    if(!(valmax>threshold))Throw("Entered peak number higher than peaks \
        above threshold!")

    //Boundary test
    while(!(((xmax-Xboundary)>0)&&((xmax+Xboundary)<nx)&&\
        ((ymax-Yboundary)>0)&&((ymax+Yboundary)<ny)))
    {
        /*if(OkCancelDialog("Peaks too close of image boundary! \
            Image will be enlarged by (" +\
        trunc(nx/4)+", "+trunc(ny/4)+") pixels to ensure analysis."))*/
        {
            image enlarged:=RealImage("Enlarged",4,nx+(nx/4),ny+(ny/4))
            subarea intermed:=enlarged[ny/8,nx/8,ny+(ny/8),nx+(nx/8)]
```

```
            intermed=original
            original:=enlarged
            image enlargedMask:=BinaryImage("EnlargedMask",nx+(nx/4), \
                ny+(ny/4))
            subarea intermedMask:=enlargedMask[ny/8,nx/8,ny+(ny/8), \
                nx+(nx/8)]
            intermedMask=mask
            mask:=enlargedMask
            xmax+=trunc(nx/8)
            ymax+=trunc(ny/8)
            oldnx=trunc(nx/8)
            oldny=trunc(ny/8)
            nx=enlarged.ImageGetDimensionSize(0)
            ny=enlarged.ImageGetDimensionSize(1)
            tempx+=oldnx
            tempy+=oldny
            //Result("Image boundary reached: image has been enlarged\n")
        }
        //else Throw("Peaks too close of image boundary!" \
            " Analysis stopped...")
    }

    Result("Found a maximum at position (" + (xmax-tempx) + ", " + \
        (ymax-tempy) + ")\t with value "+valmax+"\n")
    PeakString+=("Maximum at position (" + (xmax-tempx) + ", " + \
        (ymax-tempy) + ")\n")
    // Create mask on peak
    test=MaskPeak(original, mask, xmax, ymax, valmax, threshold)
    if(test>=Xboundary) Xboundary=test
    if(test>=Yboundary) Yboundary=test
}

image output=(!Mask*original)[tempy,tempx,tempy+yLength,tempx+xLength]
output.SetName("Peak Analysis of "+name)

output.ImageSetDescriptionText(PeakString)

ShowImage(output)
//ShowImage(Mask)
```

D.2 Radial Integration

The following script is the analysis of a diffraction EFTEM stack. The output is an EELS spectrum map where the Batson correction [20] and the angular distribution correction $\frac{1}{\theta^2+\theta_E^2}$ are taken into account. The user is free to chose the ring thickness for integration. The script has to be modified if the acceleration voltage is different from 200 keV (`E0`) or if the integration has to be performed wider than 5/8 of the image size (`IntegrationDiagonalFraction`).

```
// $BACKGROUND$

image front:=GetFrontImage()
string name=front.ImageGetName()

Number originX, originY, originZ, scaleX, scaleY, scaleZ, trash
String unitX, unitY, unitZ

front.ImageGetDimensionCalibration(0, originX, scaleX, unitX, trash )
front.ImageGetDimensionCalibration(1, originY, scaleY, unitY, trash )
front.ImageGetDimensionCalibration(2, originZ, scaleZ, unitZ, trash )

//******************* Functions ***********************
void InverseInput (number &r1,number &r2)
{
    number temp
    if(r1>r2)
    {
        temp=r1
        r1=r2
        r2=temp
        return
    }
}
//Count non-zero pixels in an image
number CountPixels (image Img)
{
    image CountPixel:=tert(Img>0,1,0)
    number PixelNumber=Sum(CountPixel)
    Return(PixelNumber)
}
// Calculate the radial integration
number RadialIntegration (image SelectedImage, number r1, number r2)
{
```

```
    SelectedImage=tert(iradius>=r1 && iradius<=r2, SelectedImage, 0)
    number total=sum(SelectedImage)/CountPixels(SelectedImage)
    Return(total)
}
// Shows the selected area on the "Highest peak" slice
void ShowFrontImage(image Img, number r1, number r2, number dept)
{
    number nx=Img.ImageGetDimensionSize(0)
    number ny=Img.ImageGetDimensionSize(1)
    image Slice:=Slice2(Img,0,0,dept,0,nx,1,1,ny,1)
    Slice=tert(iradius>=r1 && iradius<=r2, Slice, 0)
    image Output=slice
    Output.ImageSetName("Analyzed area of "+name)
    Output.ImageSetDimensionCalibration(0, originX, scaleX, unitX, 0 )
    Output.ImageSetDimensionCalibration(0, originY, scaleY, unitY, 0 )
    ShowImage(Output)
}
// Checking stack for highest peak position
number FindMaxPosition(image Img, number &TransmittedX, \
    number &transmittedY)
{
    number nx=Img.ImageGetDimensionSize(0)
    number ny=Img.ImageGetDimensionSize(1)
    number nz=Img.ImageGetDimensionSize(2)
    number k,valmax, z=0, newvalmax=0
    image slice
    for(k=0;k<nz;k++)
    {
        slice:=slice2(Img,0,0,k,0,nx,1,1,ny,1)
        valmax=Sum(slice)
        if(valmax>newvalmax)
        {
            max(slice,TransmittedX,TransmittedY)
            z=k
            newvalmax=valmax
        }
    }
    Return(z)
}

//***************** Body ***************************
```

```
Result(DateStamp()+" Start radial integration of "+name+"\n")
number width = front.ImageGetDimensionSize( 0 )
number height = front.ImageGetDimensionSize( 1 )
number dept=front.ImageGetDimensionSize(2)
number MaxRadius=(height>=width) ? width/2 : height/2
number TransmittedFWHM=0, Step=5, transmittedX, transmittedY, MaxDept

//if(!getnumber("Enter transmitted peack width (px):", \
    //15,TransmittedFWHM))exit(0)
if(!getnumber("Enter radial step (px):", 5,Step))exit(0)

// Check automatically for most intense slice
MaxDept=FindMaxPosition(front, transmittedX, transmittedY)

/* Center the transmitted beam:
    take coordinates and create new stack with transmitted beam in center.
    Dimensions are increased by "Shift" and old stack stuck in it.*/
number ShiftX=(trunc(width/2)-transmittedX)
number ShiftY=(trunc(height/2)-transmittedY)
number NewDimX=width+abs(ShiftX)
number NewDimY=height+abs(ShiftY)

image Increased=RealImage("Machin",4,NewDimX,NewDimY, dept)
image SliceIncreased

if(ShiftX>=0 && ShiftY>=0)
{
    SliceIncreased:=Slice3(Increased,ShiftX,ShiftY,0,0,width,1, \
        1,height,1,2,dept,1)
    SliceIncreased=Slice3(front,0,0,0,0,width,1,1,height,1,2,dept,1)
}
else if(ShiftX<0 && ShiftY>=0)
{
    SliceIncreased:=Slice3(Increased,0,ShiftY,0,0,width,1,1,height,1, \
        2,dept,1)
    SliceIncreased=Slice3(front,0,0,0,0,width,1,1,height,1,2,dept,1)
}
else if(ShiftX>=0 && ShiftY<0)
{
    SliceIncreased:= Slice3(Increased,ShiftX,0,0,0,width,1,1,height,1, \
        2,dept,1)
    SliceIncreased=Slice3(front,0,0,0,0,width,1,1,height,1,2,dept,1)
```

```
}
else
{
    SliceIncreased:=Slice3(Increased,0,0,0,0,width,1,1,height,1,2,dept,1)
    SliceIncreased=Slice3(front,0,0,0,0,width,1,1,height,1,2,dept,1)
}

number IntegrationDiagonalFraction=5/8
// Analyze IntegrationDiagonalFraction of smaller image dimension
number SmallerSize=trunc(MaxRadius*IntegrationDiagonalFraction)

number TotalIntegrations=trunc((SmallerSize-TransmittedFWHM)/Step)
image LinePlot:=RealImage("",4,dept,1)
image ADCLinePlot:=RealImage("",4,dept,1)


image Map=RealImage("Map", 4, dept, TotalIntegrations)
image AngularDistributionCorrection=RealImage("ADC", 4, dept, \
    TotalIntegrations)
image Slice, ADCslice
number i=0, k=0, r1=TransmittedFWHM, r2=r1+Step

image IncreasedForBatson=Increased.ImageClone()

number Theta, ThetaE, E0=200000 // Supposing 200kV acceleration voltage
//Fill map
for(i=0;i<TotalIntegrations;i++)
{
    Theta=((((i+0.5)*(Step*scaleX))+(TransmittedFWHM*scaleX))*2*Pi()/2505)
    Slice:=Slice2(Map,0,i,0,0,dept,1,1,1,1)
    ADCslice:=Slice2(AngularDistributionCorrection,0,i,0,0,dept,1,1,1,1)
    for(k=0;k<dept;k++)
    {
        ThetaE=(((k*scaleZ)-originZ)/(2*E0))
        OpenAndSetProgressWindow("Radial integration process","Radius: " \
            +(i+1)+"/"+(TotalIntegrations)+" ("+trunc((i*dept+k+1)/ \
            (TotalIntegrations*dept)*100)+"%)","Channel: "+(k+1)+"/"+dept)
        image FrontSlice=slice2(Increased,0,0,k,0,width,1,1,height,1)
        number value=RadialIntegration (FrontSlice, r1, r2)
        image GraphPoint:=LinePlot[0,k,1,k+1]
        image ADCGraphPoint:=ADCLinePlot[0,k,1,k+1]
        GraphPoint=value
```

```
        ADCGraphPoint=1000000*((Theta**2)+(ThetaE**2))
    }
    Slice=LinePlot
    ADCslice=ADCLinePlot
    r1=r2
    r2=r1+Step
}

//ShowFrontImage(Increased, TransmittedFWHM, r2, MaxDept)

//Set up map look
Map.ImageSetDimensionCalibration(0, originZ, scaleZ, unitZ, 0 )
Map.ImageSetDimensionCalibration(1, (TransmittedFWHM*scaleX), \
    (Step*scaleX), unitX, 0 )
Map.ImageSetIntensityScale(front.ImageGetIntensityScale())
Map.ImageSetIntensityUnitString("e-")
Map.SetZoom(8)
Map.ImageSetName("Radial integration map of "+Name)
Map.SetContrastMode(1)
Map.SetColorMode(4)

//Map.ShowImage()
//*********************************************************************
//********************* Setup Batson correction ***********************
//*********************************************************************
/*if(!(ContinueCancelDialog("Perform Batson correction?")))
{
    Map*=AngularDistributionCorrection
    Map.ImageSetDescriptionText("Created on "+DateStamp()+"\n\n \
        Inner radius:\t"+TransmittedFWHM+" px\nOuter radius:\t" \
        +SmallerSize+" px\nStep:\t\t"+Step+" px")
    ShowImage(Map)
    Exit(0)
}*/
Result(DateStamp()+ " Performing Batson correction" \
    " on radial integration map of "+name+"\n")
//************** Functions ***********************
number IntegrateOverWindow(image Spectrum, number EnergyWindow, \
    number &Peak)
{
    number Eorigin, Escale, Iscale, trash, HalfWindow, Integral
    string unit
```

```
    image Window

    Spectrum.ImageGetDimensionCalibration(0, Eorigin, Escale, \
        unit, trash )
    Iscale=Spectrum.ImageGetIntensityScale()

    if (Peak==0)
    {
        Max(Spectrum, Peak, trash)
        Spectrum.ImageSetDimensionOrigin(0, (-Peak*Escale) )
    }

    HalfWindow=trunc(EnergyWindow/(2*Escale))
    number MinWindow=((Peak-HalfWindow)>0) ? (Peak-HalfWindow) : 0
    Window=Spectrum[0,MinWindow,1,(Peak+HalfWindow)]
    Integral=Sum(Window*Iscale)
    Return(Integral)
}

number IntegrateOverWindowWithFloatingPeak(image Spectrum, \
    number EnergyWindow, number &Peak)
{
    number Eorigin, Escale, Iscale, trash, HalfWindow, Integral
    string unit
    image Window

    Spectrum.ImageGetDimensionCalibration(0, Eorigin, Escale, \
        unit, trash )
    Iscale=Spectrum.ImageGetIntensityScale()
    Max(Spectrum, Peak, trash)
    HalfWindow=trunc(EnergyWindow/(2*Escale))
    number MinWindow=((Peak-HalfWindow)>0) ? (Peak-HalfWindow) : 0
    Window=Spectrum[0,MinWindow,1,(Peak+HalfWindow)]
    Integral=Sum(Window*Iscale)
    Return(Integral)
}

/*number IntegrateOverWindowWithFixedPeak(image Spectrum, \
    number EnergyWindow, number Peak)
{
    number Eorigin, Escale, Iscale, trash, HalfWindow, Integral
    string unit
```

```
    image Window

    Spectrum.ImageGetDimensionCalibration(0, Eorigin, Escale, \
        unit, trash )
    Iscale=Spectrum.ImageGetIntensityScale()

    HalfWindow=trunc(EnergyWindow/(2*Escale))
    number MinWindow=((Peak-HalfWindow)>0) ? (Peak-HalfWindow) : 0
    Window=Spectrum[0,MinWindow,1,(Peak+HalfWindow)]
    Integral=Sum(Window*Iscale)
    Return(Integral)
}*/
//*************** Body ************************
// Create Image Spectrum for plural scattering removal
image ImageSpectrum=RealImage("ImageSpectrum for Batson correction", \
    4,dept,1)
for(i=0;i<dept;i++)
{
    image FrontSlice=slice2(IncreasedForBatson,0,0,i,0,width,1,1,height,1)
    number value=sum(FrontSlice)/(width*height)
    value=(value>0) ? value : 0
    image ImageGraphPoint:=ImageSpectrum[0,i,1,i+1]
    ImageGraphPoint=value
}

ImageSpectrum.ImageSetDimensionCalibration(0, originZ, scaleZ, unitZ, 0 )
ImageSpectrum.ImageSetIntensityScale(front.ImageGetIntensityScale())
ImageSpectrum.ImageSetIntensityUnitString("e-")
ImageSpectrum.ImageSetName("Image Spectrum of "+Name+ \
    " for Batson correction")
//ShowImage(ImageSpectrum)

// Perform Batson correction
number EnergyWindow=3

number ImageSpectrumMax=0
number ImageSpectumIntegral=IntegrateOverWindow(ImageSpectrum, \
    EnergyWindow, ImageSpectrumMax)

image BatsonCorrectedMap:=Map.ImageClone()
image NormalizedImageSpectrum:=ImageSpectrum.ImageClone()
number MapISPeak
```

```
number PeakShift, LeftCrop, RightCrop

for(k=0;k<TotalIntegrations;k++)
{
    image slice:=BatsonCorrectedMap[k,0,k+1,dept]
    number SliceIntegral=IntegrateOverWindowWithFloatingPeak(slice, \
        EnergyWindow,MapISPeak)
    NormalizedImageSpectrum:=ImageSpectrum.ImageClone()
    NormalizedImageSpectrum*=(SliceIntegral/ImageSpectumIntegral)
    PeakShift=ImageSpectrumMax-MapISPeak
    if (PeakShift>0)
    {
        image CropedMapSlice:=slice[0,0,1,(Dept-PeakShift)]
        image PartToSubstract:=NormalizedImageSpectrum[0, PeakShift, \
            1, Dept]
        CropedMapSlice-=(PartToSubstract)
        RightCrop=(PeakShift>RightCrop) ? PeakShift : RightCrop
    }
    else if (PeakShift<0)
    {
        image CropedMapSlice:=slice[0,-PeakShift,1,Dept]
        image PartToSubstract:=NormalizedImageSpectrum[0, 0, 1, \
            (Dept+PeakShift)]
        CropedMapSlice-=(PartToSubstract)
        LeftCrop=(PeakShift<LeftCrop) ? PeakShift : LeftCrop
    }
    else
    {
        image PartToSubstract:=NormalizedImageSpectrum[0, 0, 1, Dept]
        slice-=(PartToSubstract)
    }
    //NormalizedImageSpectrum.ShowImage()
}
BatsonCorrectedMap*=AngularDistributionCorrection
image CroppedMap=BatsonCorrectedMap[0,-LeftCrop,TotalIntegrations, \
    (Dept-RightCrop)]
CroppedMap.ImageSetDescriptionText("Created on "+DateStamp()+"\n\n \
    Inner radius:\t"+TransmittedFWHM+" px\nOuter radius:\t" \
    +SmallerSize+" px\nStep:\t\t"+Step+" px\n\n \
    Batson peak integration window: "+EnergyWindow+" eV")
CroppedMap.ImageSetDimensionCalibration(0, \
    (originZ-(LeftCrop*ScaleZ)), scaleZ, unitZ, 0 )
```

```
CroppedMap.ImageSetDimensionCalibration(1, \
    (TransmittedFWHM*scaleX), (Step*scaleX), unitX, 0 )
CroppedMap.ImageSetIntensityScale(front.ImageGetIntensityScale())
CroppedMap.ImageSetIntensityUnitString("e-")
CroppedMap.SetZoom(8)
CroppedMap.SetInversionMode(0)
CroppedMap.ImageSetName("Batson corrected radial integration map of " \
    +Name)
CroppedMap.SetContrastMode(1)
CroppedMap.SetColorMode(4)

ShowImage(CroppedMap)
```

D.3 Directional Integration

The directional integration script computes the angular momentum transfer spectra taking into account the contribution from the center towards a given direction (determined by the user via image coordinates). The iteration step is defined by the user. The integration is done until reaching the (x, y) coordinates. Since the routine works with four opposite directions, it only works for "squared" diffraction pattern. For another crystal orientation, the script has to be modified.

```
// $BACKGROUND$

ImageDocument imageDoc = CreateImageDocument( "New ImageDocument" )
imageDoc.ImageDocumentEnsurePlacedOnPage()
//******************* Functions **************************
// Checking stack for highest peak position
number FindMaxPosition(image Img, number &TransmittedX, \
    number &transmittedY)
{
    number nx=Img.ImageGetDimensionSize(0)
    number ny=Img.ImageGetDimensionSize(1)
    number nz=Img.ImageGetDimensionSize(2)
    number k,valmax, z=0, newvalmax=0
    image slice
    for(k=0;k<nz;k++)
    {
        slice:=slice2(Img,0,0,k,0,nx,1,1,ny,1)
        valmax=Sum(slice)
        if(valmax>newvalmax)
        {
            max(slice,TransmittedX,TransmittedY)
            z=k
            newvalmax=valmax
        }
    }
    Return(z)
}

number CheckIfElasticDiffractionContribution(image Map, \
    image LinePlot, number Iterator)
{
    if(Iterator>5)
    {
```

```
        number MapXsize=Map.ImageGetDimensionSize(0)
        number LinePlotSum=Sum(LinePlot)
        image slice:=Slice2(Map,0,(Iterator-6),0,0,MapXsize,1,1,5,1)
        number MapSliceMean=Sum(slice)/5
        number RaiseFactor=1.15
        if(LinePlotSum>(RaiseFactor*MapSliceMean))Return(1)
        Return(0)
    }
    Return(0)
}
//******************* Main ****************************
number nx, ny, nz
number scalex, scaley, scalez, originx, originy, originz, trash
string name, direction="000"
string unitx=" 1/nm", unitz

image front:=GetFrontImage()
front.GetName(name)
front.GetSize(nx, ny)
nz=front.ImageGetDimensionSize(2)
front.GetScale(scalex, scaley)
front.GetOrigin(originx, originy)
front.ImageGetDimensionCalibration(2, originz, scalez, unitz, trash)

imageDoc.ImageDocumentAddImage(front)
ImageDisplay imgDisplay = front.ImageGetImageDisplay(0)

Result(DateStamp()+" Start directional integration of "+name+"\n")

image mask:=BinaryImage("Mask", nx, ny)
Mask=0

number centerX, centerY, OldPeakX, OldPeakY, PeakX, PeakY
number Step, Offset=0

MostIntenseSlice=FindMaxPosition(front, centerX, centerY)

//if(!getnumber("Enter x coordiante of transmitted beam", \
    nx/2, centerX))Throw("Integration aborted!")
//if(!getnumber("Enter y coordiante of transmitted beam", \
    ny/2, centerY))Throw("Integration aborted!")
if(!getnumber("Enter x coordiante of a peak", 0, PeakX)) \
```

```
    Throw("Integration aborted!")
if(!getnumber("Enter y coordiante of the same peak", 0, PeakY)) \
    Throw("Integration aborted!")
//if(!getnumber("Enter ZLP offset", 15, Offset)) \
    Throw("Integration aborted!")
if(!getnumber("Enter analysis step", 5, Step)) \
    Throw("Integration aborted!")

if(((PeakX-centerX)>0)&&((PeakY-centerY)<0))
{
    OldPeakX=PeakX
    OldPeakY=PeakY
    PeakX=centerX-abs(OldPeakY-centerY)
    PeakY=centerY-(OldPeakX-centerX)
}
else if(((PeakX-centerX)>0)&&((PeakY-centerY)>0))
{
    OldPeakX=PeakX
    OldPeakY=PeakY
    PeakX=centerX-(OldPeakX-centerX)
    PeakY=centerY-(OldPeakY-centerY)
}
else if(((PeakX-centerX)<0)&&((PeakY-centerY)>0))
{
    OldPeakX=PeakX
    OldPeakY=PeakY
    PeakX=centerX-(OldPeakY-centerY)
    PeakY=centerY-abs(OldPeakX-centerX)
}

number width = (centerX-PeakX), height = (centerY-PeakY)
number diagonal=Trunc(Sqrt((width**2)+(height**2)))

number IntegrationDIagonalFraction=1

number NumberIntegration=trunc(diagonal*IntegrationDIagonalFraction/Step)

image map:=RealImage("Map", 4, nz, NumberIntegration)
image AngularDistributionCorrection=RealImage("ADC", 4, nz, \
    NumberIntegration)
image MapSlice, ADCSlice
image LinePlot:=RealImage("",4,nz,1)
```

```
image ADCLinePlot:=RealImage("",4,nz,1)

number StepX=Step*width/diagonal, StepY=Step*height/diagonal
number Px1, Py1, newPx1, newPy1, Px2, Py2, newPx2, newPy2, Px3, Py3, \
    newPx3, newPy3, Px4, Py4, newPx4, newPy4
number k, n
number Ax1, Ay1, Bx1, By1, Cx1, Cy1, Dx1, Dy1
ROI trapez1=NewROI()
number Ax2, Ay2, Bx2, By2, Cx2, Cy2, Dx2, Dy2
ROI trapez2=NewROI()
number Ax3, Ay3, Bx3, By3, Cx3, Cy3, Dx3, Dy3
ROI trapez3=NewROI()
number Ax4, Ay4, Bx4, By4, Cx4, Cy4, Dx4, Dy4
ROI trapez4=NewROI()
number test
/* */
newPx1=CenterX-Offset*width/diagonal
newPy1=CenterY-Offset*height/diagonal

newPx2=CenterX+Offset*height/diagonal
newPy2=CenterY-Offset*width/diagonal

newPx3=CenterX+Offset*width/diagonal
newPy3=CenterY+Offset*height/diagonal

newPx4=CenterX-Offset*height/diagonal
newPy4=CenterY+Offset*width/diagonal

number DeltaX, DeltaY, newDeltaX, newDeltaY, TrapezBasis=3/80

number Theta, ThetaE, E0=200000 // Supposing 200kV acceleration voltage

//Fill map
image clone=mask.ImageClone()
image mostIntense:=Slice2(front,0,0,MostIntenseSlice,0,nx,1,1,ny,1)

for (k=0;k<NumberIntegration;k++)
    {
    Px1=newPx1
    Py1=newPy1
    newPx1=Px1-StepX
    newPy1=Py1-StepY
```

```
DeltaX=TrapezBasis*(Px1-centerX)
DeltaY=TrapezBasis*(Py1-centerY)
newDeltaX=TrapezBasis*(newPx1-centerX)
newDeltaY=TrapezBasis*(newPy1-centerY)

Ax1=newPx1-newDeltaY
Ay1=newPy1+newDeltaX
trapez1.ROISetPoint (Ax1, Ay1)

Bx1=newPx1+newDeltaY
By1=newPy1-newDeltaX
trapez1.ROIAddVertex(Bx1, By1)

Cx1=Px1+DeltaY
Cy1=Py1-DeltaX
trapez1.ROIAddVertex(Cx1, Cy1)

Dx1=Px1-DeltaY
Dy1=Py1+DeltaX
trapez1.ROIAddVertex(Dx1, Dy1)

trapez1.ROIAddVertex(Ax1, Ay1)
trapez1.ROISetColor( 1, 0, 0 )
trapez1.ROISetIsClosed(1)
imgDisplay.ImageDisplayAddROI( trapez1 )


Px2=newPx2
Py2=newPy2
newPx2=Px2+StepY
newPy2=Py2-StepX


Ax2=newPx2-newDeltaX
Ay2=newPy2-newDeltaY
trapez2.ROISetPoint (Ax2, Ay2)

Bx2=newPx2+newDeltaX
By2=newPy2+newDeltaY
trapez2.ROIAddVertex(Bx2, By2)
```

```
Cx2=Px2+DeltaX
Cy2=Py2+DeltaY
trapez2.ROIAddVertex(Cx2, Cy2)

Dx2=Px2-DeltaX
Dy2=Py2-DeltaY
trapez2.ROIAddVertex(Dx2, Dy2)

trapez2.ROIAddVertex(Ax2, Ay2)
trapez2.ROISetColor( 0, 1, 0 )
trapez2.ROISetIsClosed(1)
imgDisplay.ImageDisplayAddROI( trapez2 )


Px3=newPx3
Py3=newPy3
newPx3=Px3+StepX
newPy3=Py3+StepY

Ax3=newPx3+newDeltaY
Ay3=newPy3-newDeltaX
trapez3.ROISetPoint (Ax3, Ay3)

Bx3=newPx3-newDeltaY
By3=newPy3+newDeltaX
trapez3.ROIAddVertex(Bx3, By3)

Cx3=Px3-DeltaY
Cy3=Py3+DeltaX
trapez3.ROIAddVertex(Cx3, Cy3)

Dx3=Px3+DeltaY
Dy3=Py3-DeltaX
trapez3.ROIAddVertex(Dx3, Dy3)

trapez3.ROIAddVertex(Ax3, Ay3)
trapez3.ROISetColor( 0, 0, 1 )
trapez3.ROISetIsClosed(1)
imgDisplay.ImageDisplayAddROI( trapez3 )


Px4=newPx4
```

```
Py4=newPy4
newPx4=Px4-StepY
newPy4=Py4+StepX

Ax4=newPx4+newDeltaX
Ay4=newPy4+newDeltaY
trapez4.ROISetPoint (Ax4, Ay4)

Bx4=newPx4-newDeltaX
By4=newPy4-newDeltaY
trapez4.ROIAddVertex(Bx4, By4)

Cx4=Px4-DeltaX
Cy4=Py4-DeltaY
trapez4.ROIAddVertex(Cx4, Cy4)

Dx4=Px4+DeltaX
Dy4=Py4+DeltaY
trapez4.ROIAddVertex(Dx4, Dy4)

trapez4.ROIAddVertex(Ax4, Ay4)
trapez4.ROISetColor( 1, 1, 0 )
trapez4.ROISetIsClosed(1)
imgDisplay.ImageDisplayAddROI( trapez4 )


ROIAddToMask(trapez1, Mask, 0, 0, nx, ny)
ROIAddToMask(trapez2, Mask, 0, 0, nx, ny)
ROIAddToMask(trapez3, Mask, 0, 0, nx, ny)
ROIAddToMask(trapez4, Mask, 0, 0, nx, ny)

Theta=((((k+0.5)*(Step*scaleX))+(Offset*scaleX))*2*Pi()/2505)
MapSlice:=Slice2(Map,0,k,0,0,nz,1,1,1,1)
ADCSlice:=Slice2(AngularDistributionCorrection,0,k,0,0,nz,1,1,1,1)
for (n=0;n<nz;n++)
{
        ThetaE=(((n*scaleZ)-originZ)/(2*E0))
        OpenAndSetProgressWindow("Directional integration process", \
            "Angle: "+(k+1)+"/"+(NumberIntegration)+" (" \
            +trunc((k*nz+n+1)/(NumberIntegration*nz)*100)+"%)", \
            "Channel: "+(n+1)+"/"+nz)
        image Slice:=Slice2(front,0,0,n,0,nx,1,1,ny,1)
```

```
            number value=Sum(Slice*Mask)/Sum(Mask)
            image GraphPoint:=LinePlot[0,n,1,n+1]
            image ADCGraphPoint:=ADCLinePlot[0,n,1,n+1]
            GraphPoint=value
            ADCGraphPoint=1000000*((Theta**2)+(ThetaE**2))
        }
    MapSlice=LinePlot
    ADCSlice=ADCLinePlot
    clone+=Mask*mostIntense
    Mask=0

    /*test=CheckIfElasticDiffractionContribution(Map,LinePlot,k)
    if(test)break*/
}

clone.ImageSetName("Analysed area")
clone.ShowImage()
GetString("Analysed direction?","200", direction)

//Set up map look
Map.ImageSetDimensionCalibration(0, originz, scalez, unitz, 0 )
Map.ImageSetDimensionCalibration(1, (Offset*scaleX), (Step*scaleX), \
    unitX, 0 )
Map.ImageSetIntensityScale(front.ImageGetIntensityScale())
Map.ImageSetIntensityUnitString("e-")

Map.SetZoom(8)
Map.SetContrastMode(2)
Map.ImageSetName("Directional "+direction+" integration map of "+Name)

/*image map_display
if(test)
{
    OKDialog("Contribution of diffracted spot detected;" \
        " analysis stopped...")
    map_display:=Slice2(Map,0,0,0,0,nz,1,1,k,1)
}
else
{
    map_display:=Map
}
```

```
map_display.SetZoom(8)
map_display.SetContrastMode(2)
map_display.ImageSetName("Directional integration map of "+Name)

ShowImage(map_display)*/

/*image AnalysedRegion:=RealImage("Analysed region", 4, nx, ny)
image Slice:=Slice2(front,0,0,11,0,nx,1,1,ny,1)
AnalysedRegion=mask*Slice
ShowImage(AnalysedRegion)*/
//Map.ShowImage()
//ShowImage(Mask)

//*********************************************************************
//********************* Setup Batson correction ***********************
//*********************************************************************
/*if(!(ContinueCancelDialog("Perform Batson correction?")))
{
    Map*=AngularDistributionCorrection
    Map.ImageSetDescriptionText("Created on "+DateStamp()+"\n\n \
        ZLP offset:\t"+Offset+" px\nStep:\t\t"+Step+" px\n \
        Analysed direction:\t"+direction)
    ShowImage(Map)
    Exit(0)
}*/
Result(DateStamp()+" Performing Batson correction" \
    " on directional integration map of "+name+"\n")
//************** Functions ************************
number IntegrateOverWindow(image Spectrum, number EnergyWindow, \
    number &Peak)
{
    number Eorigin, Escale, Iscale, trash, HalfWindow, Integral
    string unit
    image Window

    Spectrum.ImageGetDimensionCalibration(0, Eorigin, Escale, \
        unit, trash )
    Iscale=Spectrum.ImageGetIntensityScale()

    if (Peak==0)
    {
        Max(Spectrum, Peak, trash)
```

```
        Spectrum.ImageSetDimensionOrigin(0, (-Peak*Escale) )
    }

    HalfWindow=trunc(EnergyWindow/(2*Escale))
    number MinWindow=((Peak-HalfWindow)>0) ? (Peak-HalfWindow) : 0
    Window=Spectrum[0,MinWindow,1,(Peak+HalfWindow)]
    Integral=Sum(Window*Iscale)
    Return(Integral)
}

number IntegrateOverWindowWithFloatingPeak(image Spectrum, \
    number EnergyWindow, number &Peak)
{
    number Eorigin, Escale, Iscale, trash, HalfWindow, Integral
    string unit
    image Window

    Spectrum.ImageGetDimensionCalibration(0, Eorigin, Escale, \
        unit, trash )
    Iscale=Spectrum.ImageGetIntensityScale()
    Max(Spectrum, Peak, trash)
    HalfWindow=trunc(EnergyWindow/(2*Escale))
    number MinWindow=((Peak-HalfWindow)>0) ? (Peak-HalfWindow) : 0
    Window=Spectrum[0,MinWindow,1,(Peak+HalfWindow)]
    Integral=Sum(Window*Iscale)
    Return(Integral)
}

//Count non-zero pixels in an image
number CountPixels (image Img)
{
    image CountPixel:=tert(Img>0,1,0)
    number PixelNumber=Sum(CountPixel)
    Return(PixelNumber)
}

// Calculate the circular integration
number RadialIntegration (image SelectedImage, number r1, number r2)
{
    SelectedImage=tert(iradius>=r1 && iradius<=r2, SelectedImage, 0)
    number total=sum(SelectedImage)/CountPixels(SelectedImage)
    Return(total)
```

```
}
//*************** Body ************************
// Create Image Spectrum for plural scattering removal
image ImageSpectrum=RealImage("ImageSpectrum for Batson correction",4, \
    nz,1)
for(k=0;k<nz;k++)
{
    image FrontSlice=slice2(front,0,0,k,0,nx,1,1,ny,1)
    number value=sum(FrontSlice)/(width*height)
    value=(value>0) ? value : 0
    image ImageGraphPoint:=ImageSpectrum[0,k,1,k+1]
    ImageGraphPoint=value
}

ImageSpectrum.ImageSetDimensionCalibration(0, originZ, scaleZ, unitZ, 0 )
ImageSpectrum.ImageSetIntensityScale(front.ImageGetIntensityScale())
ImageSpectrum.ImageSetIntensityUnitString("e-")
ImageSpectrum.ImageSetName("Image Spectrum of "+Name+ \
    " for Batson correction")
//ShowImage(ImageSpectrum)

// Perform Batson correction
number EnergyWindow=3

number ImageSpectrumMax=0
number ImageSpectumIntegral=IntegrateOverWindow(ImageSpectrum, \
    EnergyWindow, ImageSpectrumMax)

image BatsonCorrectedMap:=Map.ImageClone()
image NormalizedImageSpectrum:=ImageSpectrum.ImageClone()
number MapISPeak
number PeakShift, LeftCrop, RightCrop

for(k=0;k<NumberIntegration;k++)
{
    image slice:=BatsonCorrectedMap[k,0,k+1,nz]
    number SliceIntegral=IntegrateOverWindowWithFloatingPeak(slice, \
        EnergyWindow,MapISPeak)
    NormalizedImageSpectrum:=ImageSpectrum.ImageClone()
    NormalizedImageSpectrum*=(SliceIntegral/ImageSpectumIntegral)
    PeakShift=ImageSpectrumMax-MapISPeak
```

```
    if (PeakShift>0)
    {
        image CropedMapSlice:=slice[0,0,1,(nz-PeakShift)]
        image PartToSubstract:=NormalizedImageSpectrum[0, PeakShift, \
            1, nz]
        CropedMapSlice-=(PartToSubstract)
        RightCrop=(PeakShift>RightCrop) ? PeakShift : RightCrop
    }
    else if (PeakShift<0)
    {
        image CropedMapSlice:=slice[0,-PeakShift,1,nz]
        image PartToSubstract:=NormalizedImageSpectrum[0, 0, 1, \
            (nz+PeakShift)]
        CropedMapSlice-=(PartToSubstract)
        LeftCrop=(PeakShift<LeftCrop) ? PeakShift : LeftCrop
    }
    else
    {
        image PartToSubstract:=NormalizedImageSpectrum[0, 0, 1, nz]
        slice-=(PartToSubstract)
    }
}

BatsonCorrectedMap*=AngularDistributionCorrection
image CroppedMap=BatsonCorrectedMap[0,-LeftCrop,NumberIntegration, \
    (nz-RightCrop)]
CroppedMap.ImageSetDescriptionText("Created on "+DateStamp()+"\n\n \
    Peak offset:\t"+Offset+" px\nStep:\t\t"+Step+" px\n\n \
        Batson peak integration window: "+EnergyWindow+" eV")
CroppedMap.ImageSetDimensionCalibration(0, (originZ-(LeftCrop*ScaleZ)), \
    scaleZ, unitZ, 0 )
CroppedMap.ImageSetDimensionCalibration(1, (Offset*scaleX), \
    (Step*scaleX), unitX, 0 )
CroppedMap.ImageSetIntensityScale(front.ImageGetIntensityScale())
CroppedMap.ImageSetIntensityUnitString("e-")
CroppedMap.SetZoom(8)
CroppedMap.SetInversionMode(0)
CroppedMap.ImageSetName("Batson corrected directional "+direction+ \
    " integration map of "+Name)
CroppedMap.SetContrastMode(1)
CroppedMap.SetColorMode(4)
ShowImage(CroppedMap)
```

E Implementation of the Kröger formula using Mathematica©

E.1 Motivation

As explained in chapter 4.3, the simpler relation between the loss function and the double differential cross section neglects both, relativistic and surface effects. This is justified in the case of metallic films of reasonable thickness, but might change for semi-conductors or very thin films.

The idea behind this appendix was to compare experiments with theoretical calculations in the case where those effects are relevant. In such cases, the complexity of the relation makes it impossible to retrieve the loss function from the experimental data.

The complete relation between the loss function and the double differential scattering probability with consideration of surface and relativistic effects has been published in 1968 by Erhard Kröger [111], thus commonly called "Kröger formula":

$$\begin{aligned}
\frac{\partial P(\omega,\boldsymbol{k}_\perp)}{\partial\omega\partial^2 k_\perp} = &\frac{e^2}{\pi^2\hbar v^2}\cdot\Im\left[\frac{\mu^2}{\varepsilon^*\varphi^2}\cdot 2a\right.\\
&-\frac{2k_\perp^2\left(\varepsilon^*-\varepsilon_0\right)^2}{\varphi_0^4\varphi^4}\cdot\left\{\frac{\varphi_{01}^4}{\varepsilon^*\varepsilon_0}\left(\frac{\sin^2\left(\frac{\omega a}{v}\right)}{L^+}+\frac{\cos^2\left(\frac{\omega a}{v}\right)}{L^-}\right)\right.\\
&+\beta^2\cdot\frac{\lambda_0}{\varepsilon_0}\cdot\frac{\omega}{v}\cdot\varphi_{01}^2\cdot\left(\frac{1}{L^+}-\frac{1}{L^-}\right)\cdot\sin\left(\frac{2\omega a}{v}\right)\\
&\left.\left.-\beta^4\cdot\frac{\omega^2}{v^2}\cdot\lambda_0\lambda\left(\frac{\cos^2\left(\frac{\omega a}{v}\right)\tanh(\lambda a)}{L^+}+\frac{\sin^2\left(\frac{\omega a}{v}\right)\coth(\lambda a)}{L^-}\right)\right\}\right]
\end{aligned}$$

using following abbreviations:

$$\lambda=\sqrt{k_\perp^2-\frac{\varepsilon^*\omega^2}{c^2}} \qquad \lambda_0=\sqrt{k_\perp^2-\frac{\varepsilon_0\omega^2}{c^2}}$$

$$L^+=\lambda_0\varepsilon^*+\lambda\varepsilon_0\tanh(\lambda a) \qquad L^-=\lambda_0\varepsilon^*+\lambda\varepsilon_0\coth(\lambda a)$$

$$\beta^2=\frac{v^2}{c^2} \qquad \mu^2=1-\varepsilon^*\beta^2 \qquad \mu_0^2=1-\varepsilon_0\beta^2$$

$$\varphi^2=\lambda^2+\frac{\omega^2}{v^2} \qquad \varphi_0^2=\lambda_0^2+\frac{\omega^2}{v^2} \qquad \varphi_{01}^2=k_\perp^2+\frac{\omega^2}{v^2}-\left(\varepsilon^*+\varepsilon_0\right)\frac{\omega^2}{c^2}$$

The first term in the imaginary part, $\frac{\mu^2}{\varepsilon^*\varphi^2}\cdot 2a$ is the bulk term (a being half the sample thickness), whereas the following terms correspond to the surface losses related to homogenous solutions of the Maxwell equations (which are needed to fit the boundary conditions at interfaces or surfaces) and relativistic effects [111]. This formula is an extension to the one published by Ritchie in 1957 [37]. Kröger improved this formula further by considering an oblique incidence in 1970 [112].

As demonstrated in chapter 6, it is possible to experimentally get the dispersion via the single scattering distribution. However, it is almost impossible to isolate the dielectric tensor $\boldsymbol{\varepsilon}(\omega, \boldsymbol{q})$ out of the Kröger formula. But it is possible to calculate the dispersion relation with the formula and compare the experimental data with the calculated ones. The Kröger formula has therefore been implemented using Mathematica© (http://www.wolfram.com/mathematica/).

To verify the correctness of the code, a comparison of the resulting simulation is compared to the work of Erni and Browning [113] performed in 2008. The code is then further improved in order to perform the calculations with any optical data in form of (λ, η, κ) triplets where λ is the wavelength, $\eta(\lambda)$ the refractive index and $\kappa(\lambda)$ the extinction coefficient of the material. By doing so, it is possible to simulate the behavior of the material extremely close to $\boldsymbol{q} = \boldsymbol{0}$ (in this work for scattering angle up to 250 μrad, which corresponds to $q = 0.63\ \text{nm}^{-1}$ at 200 kV acceleration voltage) and extract relativistic effects such as guided Čerenkov radiation [114]. Since silicon is used in both cited cases, the code presented hereafter is also based on Si data.

E.2 Results of the implementation

The approach of the problem has been made in two steps. The first step is implementing the formula in a continuous case, and the second step is transforming the formula such that it allows the use of discreet data. The advantage of doing so is the guarantee that the simulation does well while using lab measurements, these later being point measurements.

E.2.1 Continuous case

An approximation of the dielectric function of silicon has been proposed by Chen *et al.* [115].

It is proven (*e.g.* in [116]) that for non-magnetic materials, the relations

$$\eta(\omega) = \sqrt{\frac{\sqrt{\varepsilon_1^2(\omega) + \varepsilon_2^2(\omega)} + \varepsilon_1(\omega)}{2}} \tag{E.1}$$

$$\kappa(\omega) = \sqrt{\frac{\sqrt{\varepsilon_1^2(\omega) + \varepsilon_2^2(\omega)} - \varepsilon_1(\omega)}{2}} \tag{E.2}$$

hold, where $\eta(\omega)$ is the refractive index, $\kappa(\omega)$ the absorption coefficient, $\varepsilon_1(\omega)$ and $\varepsilon_2(\omega)$ the real and the imaginary part of the dielectric function respectively. Combining (E.1) and (E.2) leads to the formulation of $\varepsilon_1(\omega)$ and $\varepsilon_2(\omega)$ depending uniquely on $\eta(\omega)$ and $\kappa(\omega)$, which can be determined experimentally:

$$\varepsilon_1(\omega) = \eta^2(\omega) - \kappa^2(\omega) \tag{E.3}$$

$$\varepsilon_2(\omega) = 2\eta(\omega)\kappa(\omega) \tag{E.4}$$

Chen *et al.* demonstrate that using

$$\eta(\omega) = \eta_b - \frac{1}{2}\sum_{i=1}^{q} \frac{f_i(\omega^2 - \omega_i^2 - \Gamma_i^2)}{\left[(\omega-\omega_i)^2 + \Gamma_i^2\right]\left[(\omega+\omega_i)^2 + \Gamma_i^2\right]} \tag{E.5}$$

$$\kappa(\omega) = \sum_{i=1}^{q} \frac{f_i \Gamma_i \omega}{\left[(\omega-\omega_i)^2 + \Gamma_i^2\right]\left[(\omega+\omega_i)^2 + \Gamma_i^2\right]} \tag{E.6}$$

with the values in Table E.1, as well as the background refractive index $\eta_b = 1.015$ gives a good agreement with the experiment, where f_i is the oscillator strength fraction, Γ_i the damping factor and ω_i the transition energy of the i^{th} "critical-point transition" of electrons from the valence to the transition band (which basically is an inter-band transition). The background refractive index is due to the core electrons in inner shells [115].

Table E.1: Parameters in Eqs. (E.5) and (E.6) for Si.

i	f_i(eV^2)	Γ_i (eV)	ω_i (eV)
1	0.2	0.01	3.43
2	0.4	0.01	3.48
3	11.0	0.36	3.72
4	16.0	0.25	4.35
5	10.0	0.30	4.75
6	21.0	0.50	5.45
7	23.0	0.70	6.40
8	70.0	1.60	7.80
9	70.0	2.30	10.60
10	50.0	2.80	14.00

The functions $\eta(\omega)$ and $\kappa(\omega)$ using the parameters in Table E.1 are shown in Figure E.1a and Figure E.1b respectively. The blue dotted data are the optical measurements from Palik as reference.

It is important at this point to note that for the implementation of the Kröger formula, the imaginary part of $\varepsilon(\omega)$ has to be negative ([111], p. 121) for using following equation:

$$\varepsilon^*(\omega) = \varepsilon_1(\omega) - \imath\varepsilon_2(\omega) \tag{E.7}$$

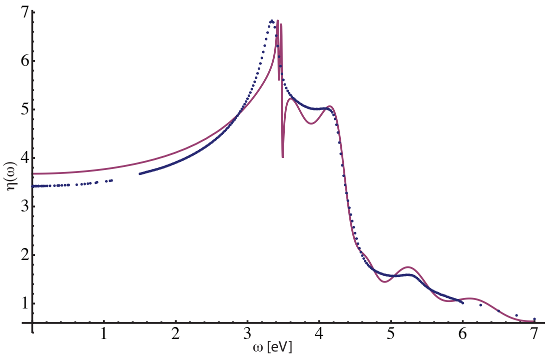

(a) Fit of $\eta(\omega)$ by Chen *et al.*

(b) Fit of $\kappa(\omega)$ by Chen *et al.*

Figure E.1: Fit of the function $\eta(\omega)$ (a) and $\kappa(\omega)$ (b) by Chen *et al.* using formulas (E.5) and (E.6) respectively, and the parameters in Table E.1. The optical measurements from Palik are represented in blue (dots).

The final implementation of the continuous case is given by following code:

$$
\begin{aligned}
&\mathtt{DR}[\omega\_,\ kp\_,\ v\_,\ thick\_] := \\
&\quad \mathtt{Module}\Big[\Big\{\mathtt{a} = thick/2,\ \mathtt{param} = \mathtt{e\^{}2/(Pi\^{}2 * hbar *}\ v\mathtt{\^{}2)},\ \mathtt{arg} = \omega * (thick/2)/v,\\
&\quad \varepsilon = \varepsilon[\omega],\ \beta = \beta[v],\ \mu = \mu[\omega,\ v],\ \varphi = \varphi[\omega,\ kp,\ v],\ \varphi_0 = \varphi 0[\omega,\ kp,\ v],\\
&\quad \varphi_{01} = \varphi 01[\omega,\ kp,\ v],\ \lambda = \lambda[\omega,\ kp],\ \lambda_0 = \lambda 0[\omega,\ kp],\\
&\quad \mathtt{L}^+ = \mathtt{Lp}[\omega,\ kp,\ thick/2],\ \mathtt{L}^- = \mathtt{Lm}[\omega,\ kp,\ thick/2]\Big\},\\
&\quad \mathtt{param} * \mathtt{Im}\Bigg[\frac{\mu^2}{\varepsilon * \varphi^2} 2\mathtt{a}\\
&\quad - \frac{2kp^2(\varepsilon - \varepsilon_0)^2}{\varphi_0^4 \varphi^4}\Bigg(\frac{\varphi_{01}^4}{\varepsilon * \varepsilon_0}\left(\frac{\mathtt{Sin}[\mathtt{arg}]^2}{\mathtt{L}^+} + \frac{\mathtt{Cos}[\mathtt{arg}]^2}{\mathtt{L}^-}\right)\\
&\quad + \beta^2 \frac{\lambda_0}{\varepsilon_0} \frac{\omega}{v} \varphi_{01}^2 \left(\frac{1}{L^+} - \frac{1}{L^-}\right) \mathtt{Sin}[2 * \mathtt{arg}]\\
&\quad - \beta^4 \frac{\omega^2}{v^2} \lambda_0 \lambda \left(\frac{\mathtt{Cos}[\mathtt{arg}]^2 * \mathtt{Tanh}[\lambda * \mathtt{a}]}{\mathtt{L}^+} + \frac{\mathtt{Sin}[\mathtt{arg}]^2 * \mathtt{Coth}[\lambda * \mathtt{a}]}{\mathtt{L}^-}\right)\Bigg)\Bigg]\Bigg]
\end{aligned}
$$

where the blue colored text are user-defined functions and the green text the parameters of the function. The four parameters are the energy loss ω in eV, the angular information kp in mrad, the speed of the electrons v in units of c and the thickness $thick$ of the slab in nm.

Note: Kröger defines kp as $\boldsymbol{k}_\perp = (k_y, k_z)$ the wavenumber of the wave propagating perpendicularly to the incoming wave (*e.g.* the beam of the microscope). The relation between the deflection angle and the momentum transfer $\hbar k$ in the same direction is given by

$$\theta_i = \frac{\hbar k_i}{p_0} \tag{E.8}$$

where p_0 is the momentum of the incident electrons, and $i = y, z$. Furthermore, the thickness is defined to be $2a$ (thus the code $a = thick/2$).

A simulation of the dispersion relations of a 100 nm thick silicon slab is shown in Figure E.2. The result is in good agreement with several works done on the same topic with silicon [113, 117–119]. The main features are the light line $\omega = ck$, the retardation Čerenkov losses which run asymptotically to the value of 3.6 eV for Si with increasing k, inter-band transitions, the surface plasmon (measured at 8.2 eV [117, 120] and calculated at 11.0 eV [113, 117]) and finally the volume plasmon at 16.6 eV. Fig. 2(d) from Erni and Browning ([113]) is the calculated scattering probability in the (E,θ)-plan of 200 kV electrons transmitting a Si film of 1000 nm thickness, and is reproduced in this work as Figure E.3 for comparison.

Note: since the relation between the energy E and the pulsation ω is $E = \hbar\omega$, and $\hbar$ has been chosen as 1 for the calculations, the comparison between Figure E.2 and E.3 is direct.

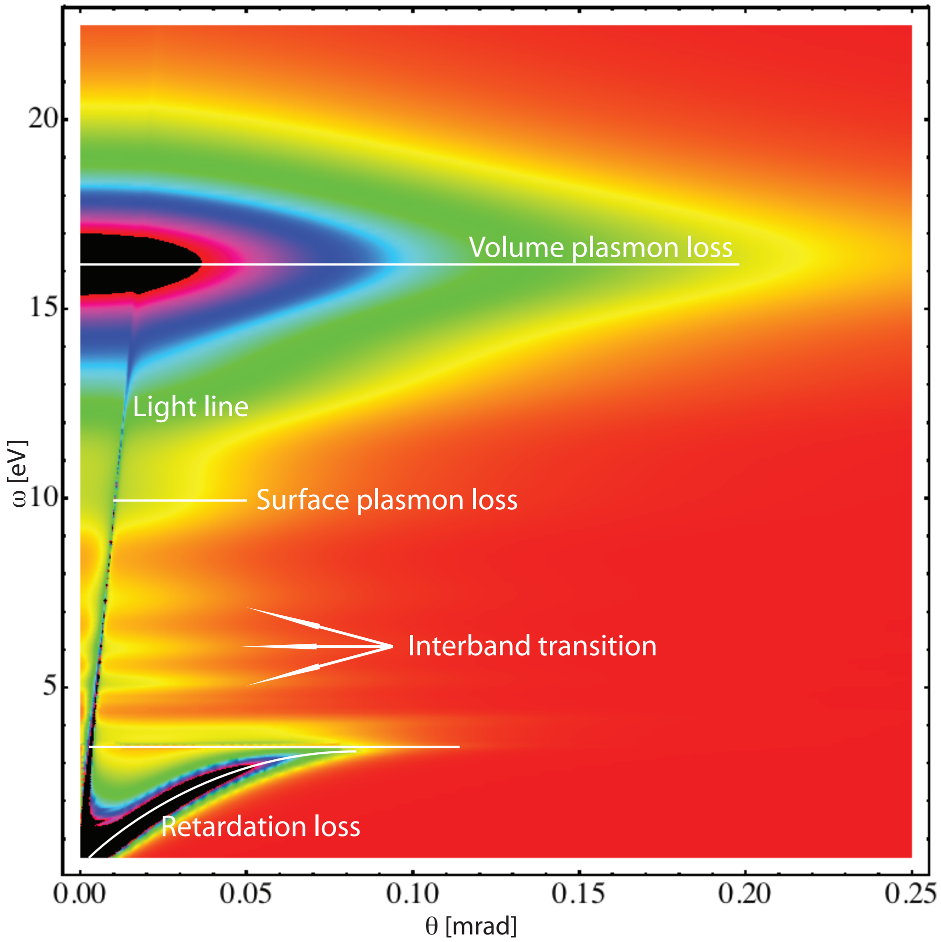

Figure E.2: Calculation with the implemented Kröger formula using fitted silicon data from 0.5 to 22.5 eV loss with an angle from 0 to 0.25 mrad. The main features are indicated in white.

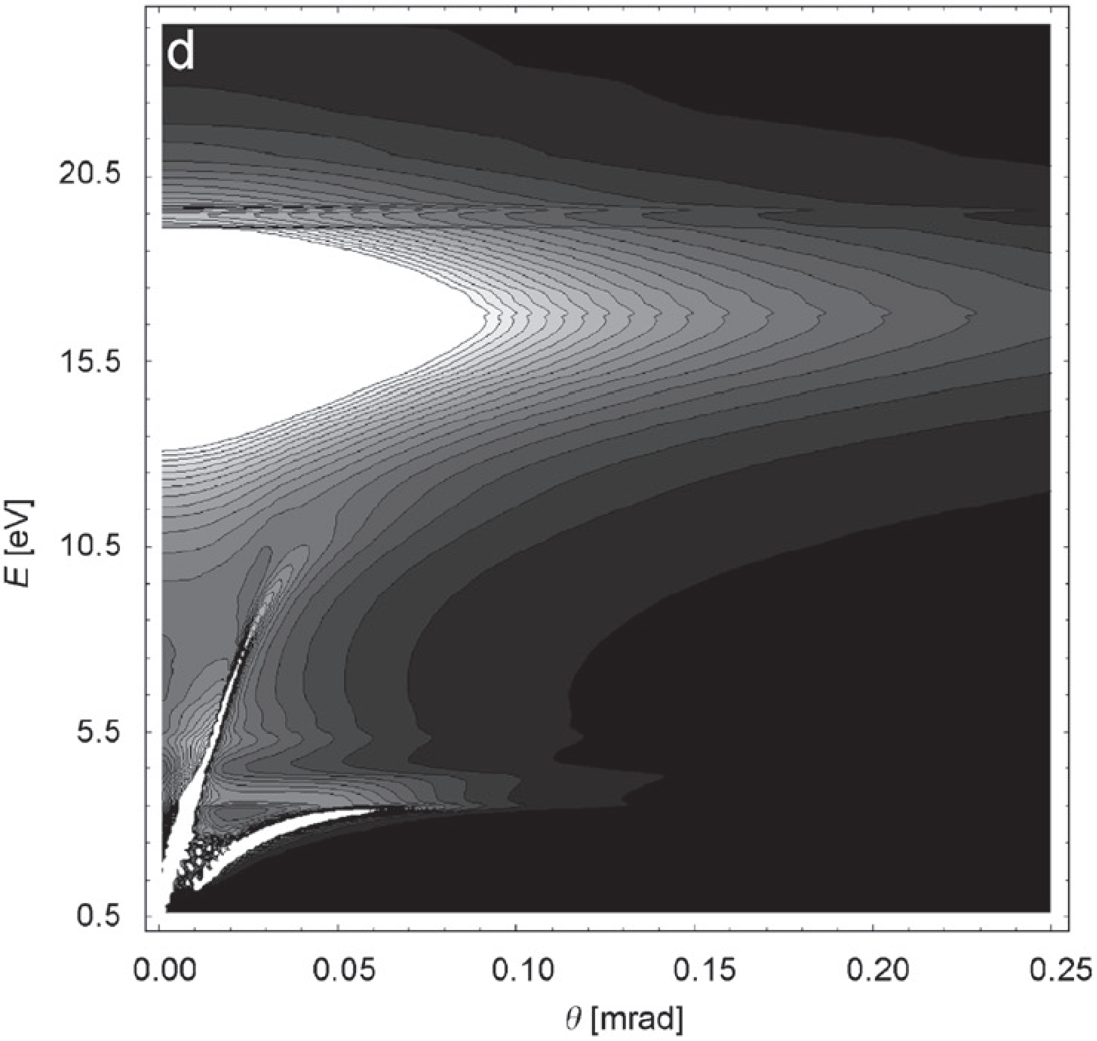

Figure E.3: Reproduction of Fig. 2(d) from [113] for comparison. Calculation of the scattering probability in a Si 1000 nm thick film with 200 kV electrons.

E.2.2 Discrete case

The discreet case has been implemented using the silicon data found in the "Handbook of Optical Constants of Solids" edited by Edward D. Palik [100]. Doing so gives the possibility to compare directly the continuous and the discreet case for agreement. The data is given in form of a table of three columns: λ in Ångström, and the values of η and κ for the given wavelength. The header of the file shows like this:

```
;  Optical constants for crystalline Si
;
;   taken from:
;
;   'Handbook of Optical Constants of Solids', Ed. by Edward D. Palik,
;   Academic Press, Inc., 1985.
;
;    Lambda (A)            n            k
;-----------------------------------------
       6.19900      0.999905   3.19000*10^(-5)
         ...           ...          ...
```

Figure E.4 shows the data, where the wavelength λ has been transformed into the energy ω (in eV) with following formula:

$$\omega = 2\pi \frac{c}{\lambda} \tag{E.9}$$

since in photon optics, $\lambda = \frac{hc}{E}$ and $E = \hbar\omega$. Choosing the Rydberg atomic units, $\hbar = 1$ thus the energy can be directly described as ω with energy units[1]. Note that equation (E.9) is only true for photon or X-ray optics. For electron,

$$\lambda = \frac{h}{\sqrt{2m_0 eE_0 \left(\frac{1+eE_0}{2m_0 c^2}\right)}} \tag{E.10}$$

has to be used [40]. Here, h is Planck's constant, m_0 the rest mass of electron, e the electric charge of an electron, E_0 the energy of the incident electron beam and c the speed of light.

Different possibilities are offered to implement the discreet case. One possibility is to modify the final formula giving the dispersion relations such as it allows discreet data. This is not a good option, since it would lead to a pixelized map with discreet values. Another possibility would be to calculate $\varepsilon_1(\omega)$ and $\varepsilon_2(\omega)$ for each measured (λ, η, κ) using equations (E.3) and (E.4) respectively and perform the interpolation of these functions, but this would be rather fastidious. A third possibility, the one used in this work, is to directly interpolate the $\eta(\omega)$ and

---

[1] 1 Ry is defined as $1/2E_h$ where $E_h = \frac{\hbar^2}{m_e a_0^2}$ is the Hartree energy. 1 E_h = 27.21138 eV (source: CODATA)

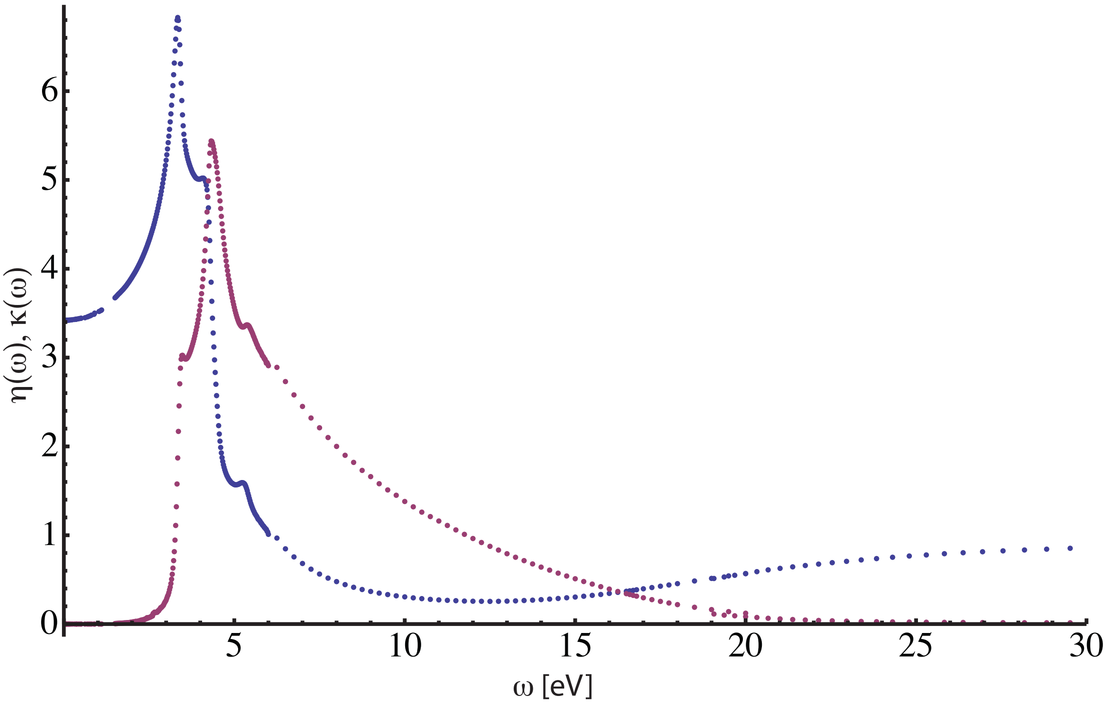

Figure E.4: $\eta(\omega)$ (blue) and $\kappa(\omega)$ (purple) from Palik's "Handbook of Optical Constants of Solids" [100].

$\kappa(\omega)$ data with a third-order spline function and do the calculation of ε_1, ε_2 and the dispersion relation with it. The interpolation is shown in Figure E.5

With the interpolated functions, it is again possible to use the Kröger formula used for the continuous case. The implementation code shows a slightly modified formula (all modified functions are called `fit[...]` in the discreet case) so computation in the discreet and the continuous case may be performed simultaneously. A comparison between the continuous and the discreet calculation of the dispersion relations is shown in Figure E.6.

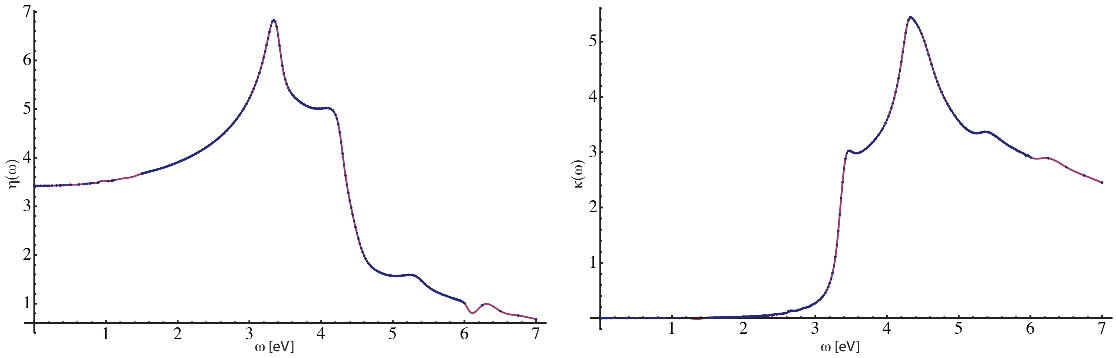

(a) Interpolation of η

(b) Interpolation of κ

Figure E.5: Interpolation (purple line) of $\eta(\omega)$ (a) and $\kappa(\omega)$ (b) of Palik's optical data (blue dots). The result is shown from 0–7 eV for better visibility in the featured zone, but the interpolation covers the whole area up to 30 eV shown in Figure E.4.

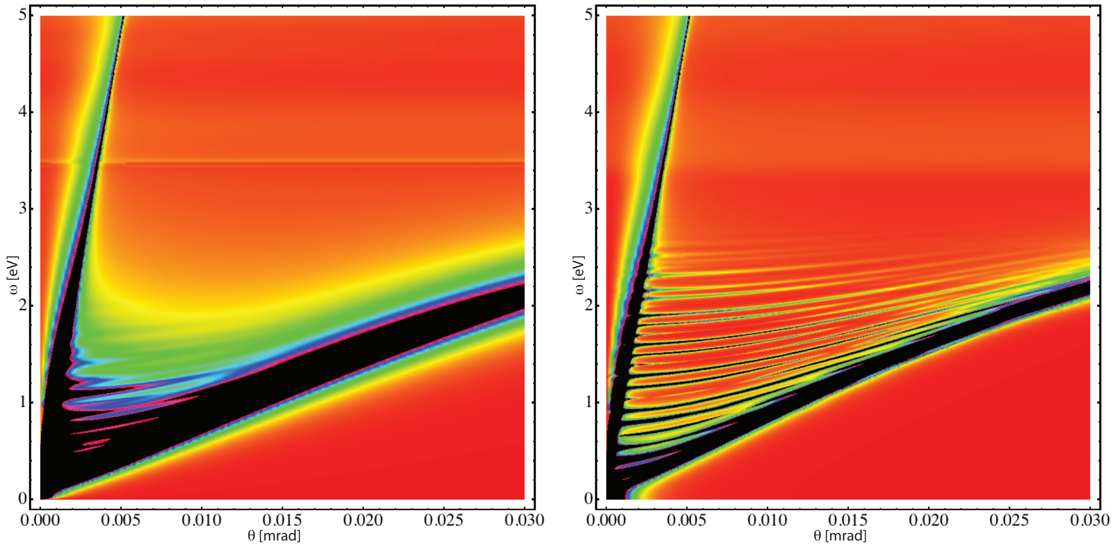

(a) Kröger's dispersion relation in the continuous case

(b) Kröger's dispersion relation in the discreet case

Figure E.6: Calculation of the dispersion relations for Si using Kröger's formula. (a) is calculated using the refractive index and the absorption coefficient calculated by Chen *et al.* [115]. (b) is calculated using Palik's optical data. The maps are calculated for an energy loss of 0–5 eV with an angular dispersion of 0–0.03 mrad. Acceleration voltage is 200 kV and the specimen thickness is 100 nm. The major features are identical, although the feature at 3.6 eV is hardly visible and the guided modes much more pronounced in the discreet case.

E.3 Implementation code

Mathematica© code for the simulation of the Kröger formula in the continuous and the discreet case. The continuous case is implemented using the parameters given by Chen *et al.* [115] for the refractive index $\eta(\omega)$ and the absorption coefficient $\kappa(\omega)$ for silicon. The discreet case gives a fit of the measured silicon data by Palik [100] for the same coefficients. To enable the comparison between the two cases in the same file, the code of the formula for the discreet case has been slightly modified (the formula is the same , only some function names change).

E.3.1 Definition of symbols and constants

```
≪ PhysicalConstants`
≪ Units`
≪ Notation`
```

```
Symbolize[λ₀]
Symbolize[φ₀]
Symbolize[φ₀₁]
Symbolize[ε₀]
Symbolize[L⁺]
Symbolize[L⁻]
Symbolize[m₀]
```

```
(* Parameters in atomic Rydberg units *)
e = Sqrt[2];
hbar = 1;
c = 2/FineStructureConstant;
ε₀ = 1/(4 Pi);
m₀ = 1;
eV = Convert[PlanckConstantReduced * SpeedOfLight *
   FineStructureConstant/BohrRadius, ElectronVolt]/(2 ElectronVolt);
mrad = 1/1000;
nm = 10⁻⁹(Meter/BohrRadius);
```

E.3.2 Calculation of $\varepsilon(\omega)$ (Chen et al. Phys. Rev. B 48 (1993) [Continuous case])

Calculation of η, κ, $\varepsilon 1$, $\varepsilon 2$ and ε

```
f = {0.2, 0.4, 11.0, 16.0, 10.0, 21.0, 23.0, 70.0, 70.0, 50.0};
Γ = {0.01, 0.01, 0.36, 0.25, 0.30, 0.50, 0.70, 1.60, 2.30, 2.80};
```

```
ωi = {3.43, 3.48, 3.72, 4.35, 4.75, 5.45, 6.40, 7.80, 10.60, 14.00};
ηb = 1.015;
κ[ω_] := Sum[f⟦i⟧ * Γ⟦i⟧ * ω/(((ω − ωi⟦i⟧)^2 + (Γ⟦i⟧)^2) * ((ω + ωi⟦i⟧)^2 + (Γ⟦i⟧)^2)), {i, 10}];
η[ω_] := ηb − 0.5 * Sum[f⟦i⟧ * (ω^2 − (ωi⟦i⟧)^2 − (Γ⟦i⟧)^2)/(((ω − ωi⟦i⟧)^2 + (Γ⟦i⟧)^2) * ((ω + ωi⟦i⟧)^2 +
        (Γ⟦i⟧)^2)), {i, 10}];
ε1[ω_] := −κ[ω]^2 + η[ω]^2;
ε2[ω_] := 2 * κ[ω] * η[ω];
ε[ω_] := ε1[ω] − ε2[ω]  I;
```

E.3.3 Import data from Palik [Discrete case]

Data import and transformation

```
dataraw = Import[ToFileName[NotebookDirectory[], "Si_palik_exp.txt"],
         "Words"]
```

Read-in [λ, η, κ]

```
offset = 36;

data = Table[{dataraw⟦i⟧, dataraw⟦i+1⟧, dataraw⟦i+2⟧},
     {i, offset, Length[dataraw], 3}];
dataLength = Length@data;

datalambda = Table[ToExpression[data⟦i,1⟧, {i,Length[data]}]];
datan = Table[ToExpression[data⟦i,2⟧], {i, Length[data]}];
datak = Table[ToExpression[data⟦i,3⟧], {i, Length[data]}];
dataenergy = Array[Convert[PlanckConstant, ElectronVolt*Second]/
           ElectronVolt * SpeedOfLight/(ToExpression[datalambda⟦#⟧] *
           10^(-10) Meter) &, Length[data]];
```

Table of PNK

```
PNK = Sort[Table[{dataenergy⟦i⟧, datan⟦i⟧, datak⟦i⟧},
    {i, Length[datalambda]}]];
epsilon1 = Array[-PNK⟦#,3⟧^2 + PNK⟦#,2⟧^2 &, Length[data]];
epsilon2 = Array[2 * PNK ⟦#,3⟧  * PNK⟦#,2⟧  &, Length[data]];
```

Energy [eV]

```
energy = Transpose[PNK]⟦1⟧;
```

Dielectric function

```
epsilon = Array[epsilon1⟦#⟧ - epsilon2⟦#⟧ I &, Length[data]];

ηω  = {(PNK // Transpose)⟦1⟧, (PNK // Transpose)⟦2⟧} // Transpose;

κω  = {(PNK // Transpose)⟦1⟧, (PNK // Transpose)⟦3⟧} // Transpose;

ε1ω = {(PNK // Transpose)⟦1⟧, -((PNK // Transpose)⟦3⟧)^2 +
   ((PNK // Transpose)⟦2⟧)^2} // Transpose;

ε2ω = {(PNK // Transpose)⟦1⟧, 2((PNK // Transpose)⟦3⟧) *
   ((PNK // Transpose)⟦2⟧)} // Transpose;
```

Interpolation

```
interη = Interpolation[ηω, Method → "Spline"];

interκ = Interpolation[κω, Method → "Spline"];

fitη [ω_] := interη[ω];
fitκ [ω_] := With[{a = interκ[ω]}, If[ a ≥ 0.01, a, 0.01]];
```

Computation of ε1 and ε2

```
fitε1[ω_] := -fitκ[ω]^2 + fitη[ω]^2;
fitε2[ω_] := 2 * fitκ[ω] * fitη[ω];
fitε[ω_] := fitε1[ω] - fitε2[ω]I;
```

E.3.4 Dispersion relation (E. Kröger, Z. Phys. 216 (1968))

Functions for continue case

$$\beta[v\_] := v/\mathtt{c};$$
$$\gamma[v\_] := 1/\mathtt{Sqrt}[1-\beta[v]^2];$$
$$\mu[\omega\_, v\_] := \mathtt{Sqrt}[1-\varepsilon[\omega]*\beta[v]^2];$$
$$\lambda[\omega\_, kp\_] := \mathtt{Sqrt}[kp^2-\varepsilon[\omega]*(\omega)^2/\mathtt{c}^2];$$
$$\lambda 0[\omega\_, kp\_] := \mathtt{Sqrt}\left[kp^2-\varepsilon_0*(\omega)^2/\mathtt{c}^2\right];$$
$$\varphi[\omega\_, kp\_, v\_] := \mathtt{Sqrt}[(\lambda[\omega, kp])^2+(\omega)^2/v^2];$$
$$\varphi 0[\omega\_, kp\_, v\_] := \mathtt{Sqrt}[(\lambda 0[\omega, \mathrm{kp}])^2+(\omega)^2/v^2];$$
$$\varphi 01[\omega\_, kp\_, v\_] : \mathtt{Sqrt}\left[kp^2+(\omega)^2/v^2-(\varepsilon[\omega]+\varepsilon_0)*(\omega)^2/\mathtt{c}^2\right];$$
$$\mathtt{Lp}[\omega\_, kp\_, a] = \lambda 0[\omega, kp]*\varepsilon[\omega]+\lambda[\omega, kp]*\varepsilon_0*\mathtt{Tanh}[\lambda[\omega, kp]*a];$$
$$\mathtt{Lm}[\omega\_, kp\_, a\_] = \lambda 0[\omega, kp]*\varepsilon[\omega]+\lambda[\omega, kp]*\varepsilon_0*\mathtt{Coth}[\lambda[\omega, kp]*a];$$

$$
\begin{aligned}
&\mathtt{DR}[\omega\_, kp\_, v\_, thick\_] :=\\
&\quad \mathtt{Module}\Big[\big\{\mathtt{a} = thick/2, \mathtt{param} = \mathtt{e}^2/(\mathtt{Pi}^2 * \mathtt{hbar} * v^2), \mathtt{arg} = \omega * (thick/2)/v,\\
&\quad \varepsilon = \varepsilon[\omega], \beta = \beta[v], \mu = \mu[\omega, v], \varphi = \varphi[\omega, kp, v], \varphi_0 = \varphi0[\omega, kp, v],\\
&\quad \varphi_{01} = \varphi01[\omega, kp, v], \lambda = \lambda[\omega, kp], \lambda_0 = \lambda0[\omega, kp],\\
&\quad \mathrm{L}^+ = \mathtt{Lp}[\omega, kp, thick/2], \mathrm{L}^- = \mathtt{Lm}[\omega, kp, thick/2]\big\},\\
&\quad \mathtt{param} * \mathtt{Im}\Bigg[\frac{\mu^2}{\varepsilon * \varphi^2} 2\mathtt{a}\\
&\quad - \frac{2kp^2(\varepsilon-\varepsilon_0)^2}{\varphi_0^4\varphi^4}\Bigg(\frac{\varphi_{01}^4}{\varepsilon*\varepsilon_0}\Bigg(\frac{\mathtt{Sin}[\mathtt{arg}]^2}{\mathrm{L}^+} + \frac{\mathtt{Cos}[\mathtt{arg}]^2}{\mathrm{L}^-}\Bigg)\\
&\quad + \beta^2\frac{\lambda_0}{\varepsilon_0}\frac{\omega}{v}\varphi_{01}^2\left(\frac{1}{L^+} - \frac{1}{L^-}\right)\mathtt{Sin}[2*\mathtt{arg}]\\
&\quad -\beta^4\frac{\omega^2}{v^2}\lambda_0\lambda\Bigg(\frac{\mathtt{Cos}[\mathtt{arg}]^2 * \mathtt{Tanh}[\lambda * \mathtt{a}]}{\mathrm{L}^+} + \frac{\mathtt{Sin}[\mathtt{arg}]^2 * \mathtt{Coth}[\lambda * \mathtt{a}]}{\mathrm{L}^-}\Bigg)\Bigg)\Bigg]\Bigg]
\end{aligned}
$$

Function for discreet case (calculated from fitted $\eta(\omega)$ and $\kappa(\omega)$)

```
fitμ[ω_,v_]:=Sqrt[1-fitε[ω]*β [v]^2];
fitλ[ω_,kp_]:=Sqrt[kp^2-fitε[ω]*(ω)^2/c^2];
fitφ[ω_,kp_,v_]:=Sqrt[(fitλ[ω,kp])^2+(ω)^2/v^2];
fitφ01[ω_,kp_,v_]:=Sqrt[kp^2+(ω)^2/v^2-(fitε[ω]+ε0)*(ω)^2/c^2];
fitLp[ω_,kp_,a_]:=λ0[ω,kp]*fitε[ω]+fitλ[ω,kp]*ε0*Tanh[fitλ[ω,kp]*a];
fitLm[ω_,kp_,a_]:=λ0[ω,kp]*fitε[ω]+fitλ[ω,kp]*ε0*Coth[fitλ[ω,kp]*a];
```

$$
\begin{aligned}
&\mathtt{fitDR}[\omega\_, kp\_, v\_, thick\_] :=\\
&\quad \mathtt{Module}\Big[\big\{\mathtt{a} = thick/2, \mathtt{param} = \mathtt{e}^2/(\mathtt{Pi}^2 * \mathtt{hbar} * v^2), \mathtt{arg} = \omega * (thick/2)/v,\\
&\quad \varepsilon = \mathtt{fit}\varepsilon[\omega], \beta = \beta[v], \mu = \mathtt{fit}\mu[\omega, v], \varphi = \mathtt{fit}\varphi[\omega, kp, v], \varphi_0 = \varphi0[\omega, kp, v],\\
&\quad \varphi_{01} = \mathtt{fit}\varphi01[\omega, kp, v], \lambda = \mathtt{fit}\lambda[\omega, kp], \lambda_0 = \lambda0[\omega, kp],\\
&\quad \mathrm{L}^+ = \mathtt{fitLp}[\omega, kp, thick/2], \mathrm{L}^- = \mathtt{fitLm}[\omega, kp, thick/2]\big\},\\
&\quad \mathtt{param} * \mathtt{Im}\Bigg[\frac{\mu^2}{\varepsilon * \varphi^2} 2\mathtt{a}\\
&\quad - \frac{2kp^2(\varepsilon-\varepsilon_0)^2}{\varphi_0^4\varphi^4}\Bigg(\frac{\varphi_{01}^4}{\varepsilon*\varepsilon_0}\Bigg(\frac{\mathtt{Sin}[\mathtt{arg}]^2}{\mathrm{L}^+} + \frac{\mathtt{Cos}[\mathtt{arg}]^2}{\mathrm{L}^-}\Bigg)\\
&\quad + \beta^2\frac{\lambda_0}{\varepsilon_0}\frac{\omega}{v}\varphi_{01}^2\left(\frac{1}{L^+} - \frac{1}{L^-}\right)\mathtt{Sin}[2*\mathtt{arg}]\\
&\quad -\beta^4\frac{\omega^2}{v^2}\lambda_0\lambda\Bigg(\frac{\mathtt{Cos}[\mathtt{arg}]^2 * \mathtt{Tanh}[\lambda * \mathtt{a}]}{\mathrm{L}^+} + \frac{\mathtt{Sin}[\mathtt{arg}]^2 * \mathtt{Coth}[\lambda * \mathtt{a}]}{\mathrm{L}^-}\Bigg)\Bigg)\Bigg]\Bigg]
\end{aligned}
$$

F Tables of values

F.1 Fundamental constants and unit

Table F.1: Fundamental constants and definitions.

Name	Symbol	Value	Units
Bohr radius $(4\pi\varepsilon_0\hbar^2(m_o e^2)^{-1})$	a_0	$0.529 \cdot 10^{-10}$	m
Speed of light in vacuum	c	$299'792'458$	$\text{m}\cdot\text{s}^{-1}$
Permittivity of space	ε_0	$8.854 \cdot 10^{-12}$	$\text{F}\cdot\text{m}^{-1}$
Electron charge	e	$-1.6022 \cdot 10^{-19}$	C
Planck's constant	h	$6.62607 \cdot 10^{-34}$	J·s
		$4.13567 \cdot 10^{-15}$	eV·s
Reduced Planck constant $(h(2\pi)^{-1})$	$\hbar$	$1.05457 \cdot 10^{-34}$	J·s
		$6.58212 \cdot 10^{-16}$	eV·s
Electron rest mass	m_0	$9.1095 \cdot 10^{-31}$	kg
		$511'000$	$\text{eV}\cdot c^{-2}$
Electron rest energy	$m_0 c^2$	$511'000$	eV
Rydberg energy $(h^2(2m_0 a_0^2)^{-1})$	R	13.61	eV

Table F.2: Conversion in SI units.

Unit	Symbol	SI equivalent
Meter	m	length unit
Kilogram	kg	mass unit
Second	s	time unit
Ampere	A	electric intensity unit
Radian	rad	angular unit
Kelvin	K	temperature unit
Steradian	sr	solid angle unit
Angström	Å	10^{-10} m
Coulomb	C	A·s
Degree Celsius	°C	"temperature in K" + 273.15
Farad	F	$s^4 \cdot A^2 \cdot m^{-2} \cdot kg^{-1}$
Hour	hr	3600 s
Inch	in	0.0254 m
Joule	J	$kg \cdot m^2 \cdot s^{-2}$
Pascal	Pa	$N \cdot m^{-2}$
SCCM	sccm	$1.67 \cdot 10^{-8}$ $m^{-3} \cdot s^{-1}$
Torr	Torr	133.322 $N \cdot m^{-2}$
Volt	V	$kg \cdot m^2 \cdot s^{-3} \cdot A^{-1}$
electron-volt	eV	$1.6022 \cdot 10^{-19}$ J

Bibliography

[1] Egerton, R. F. *Electron Energy-Loss Spectroscopy in the Electron Microscope.* Springer, third edition, (2011).

[2] Raether, H. *Excitation of Plasmons and Interband Transitions by Electrons*, volume 88 of *Springer Tracts in Modern Physics.* Springer Berlin Heidelberg, (1980).

[3] Ruthemann, G. *Naturwissenschaften* **29**(42-43), 648–648 (1941).

[4] Ruthemann, G. *Naturwissenschaften* **30**(9-10), 145–145 (1942).

[5] Hillier, J. and Baker, R. F. *J. Appl. Phys.* **15**(9), 663–675 (1944).

[6] Ehrenreich, H. and Philipp, H. R. *Phys. Rev.* **128**(4), 1622–1629 (1962).

[7] Kloos, T. and Raether, H. *Phys. Lett. A* **44**(3), 157–158 (1973).

[8] Petri, E. and Otto, A. *Phys. Rev. Lett.* **34**(20), 1283–1286 (1975).

[9] Zacharias, P. *J. Phys. F: Met. Phys.* **5**(4), 645 (1975).

[10] Batson, P. E., Chen, C. H., and Silcox, J. *Phys. Rev. Lett.* **37**(14), 937–940 (1976).

[11] Ruska, E. *The Early Development of Electron Lenses and Electron Microscopy.* Hirzel S. Verlag, (1980).

[12] Boersch, H. *Z. Phys.* **134**(2), 156–164 (1953).

[13] Beaufils, R. *Compt. Rend. (Paris)* **248**, 3145 (1959).

[14] Watanabe, H. and Uyeda, R. *J. Phys. Soc. Jap.* **17**(3), 569–570 (1962).

[15] Castaing, R. and Henry, L. *Compt. Rend. (Paris)* **255**, 76 (1962).

[16] Henkelman, R. M. and Ottensmeyer, F. P. *J. Microsc.* **102**(1), 79–94 (1974).

[17] Egerton, R. F., Philip, J. G., Turner, P. S., and Whelan, M. J. *J. Phys. E: Sci. Instrum.* **8**(12), 1033 (1975).

[18] Reimer, L., Fromm, I., and Rennekamp, R. *Ultramicroscopy* **24**(4), 339–354 (1988).

[19] Reimer, L. and Rennekamp, R. *Ultramicroscopy* **28**(1–4), 258–265 (1989).

[20] Batson, P. E. and Silcox, J. *Phys. Rev. B* **27**(9), 5224–5239 (1983).

[21] Leapman, R. D., Fejes, P. L., and Silcox, J. *Phys. Rev. B* **28**(5), 2361–2373 (1983).

[22] Schattschneider, P., Födermayr, F., and Su, D.-S. *Phys. Rev. Lett.* **59**(6), 724–727 (1987).

[23] Su, D. S. and Schattschneider, P. *Philos. Mag. A* **65**(5), 1127–1140 (1992).

[24] Wang, Y. Y., Zhang, F. C., Dravid, V. P., Ng, K. K., Klein, M. V., Schnatterly, S. E., and Miller, L. L. *Phys. Rev. Lett.* **77**(9), 1809–1812 (1996).

[25] Yase, K., Horiuchi, S., Kyotani, M., Yumura, M., Uchida, K., Ohshima, S., Kuriki, Y., Ikazaki, F., and Yamahira, N. *Thin Solid Films* **273**(1–2), 222–224 (1996).

[26] Batson, P. E. (2009). Oral presentation at the seminar hold on honnor of Ch. Colliex (65 th. Birthday).

[27] Hedin, L. and Lundqvist, S. In *Solid State Physics,* Frederick Seitz, D. T. and Ehrenreich, H., editors, volume 23, 1–181. Academic Press (1970).

[28] Quong, A. A. and Eguiluz, A. G. *Phys. Rev. Lett.* **70**(25), 3955–3958 (1993).

[29] Vast, N., Reining, L., Olevano, V., Schattschneider, P., and Jouffrey, B. *Phys. Rev. Lett.* **88**(3), 037601 (2002).

[30] Vallerot, J.-M., Bourrat, X., Mouchon, A., and Chollon, G. *Carbon* **44**(9), 1833–1844 (2006).

[31] Stöger-Pollach, M. and Schattschneider, P. *Ultramicroscopy* **107**(12), 1178–1185 (2007).

[32] Zhang, L., Erni, R., Verbeeck, J., and Van Tendeloo, G. *Phys. Rev. B* **77**(19), 195119–7 (2008).

[33] Stöger-Pollach, M. *Micron* **39**(8), 1092–1110 (2008).

[34] Zhang, L., Turner, S., Brosens, F., and Verbeeck, J. *Phys. Rev. B* **81**(3), 035102 (2010).

[35] Bertoni, G., Verbeeck, J., and Brosens, F. *Microsc. Res. Techniq.* **74**(3), 212–218 (2011).

[36] Curtis, G. H. and Silcox, J. *Rev. Sci. Instrum.* **42**(5), 630–637 (1971).

[37] Ritchie, R. H. *Phys. Rev.* **106**(5), 874–881 (1957).

[38] Rossouw, D. and Botton, G. A. *Phys. Rev. Lett.* **110**(6), 066801 (2013).

[39] Erni, R., Rossell, M. D., Kisielowski, C., and Dahmen, U. *Phys. Rev. Lett.* **102**(9), 096101 (2009).

[40] Williams, D. B. and Carter, C. B. *Transmission Electron Microscopy*. Springer, second edition, (2009).

[41] Senoussi, S., Henry, L., and Castaing, R. *J. de Microsc.* **11**, 19 (1971).

[42] Zanchi, G., Sevely, J., and Jouffrey, B. *Optik* **48**(2), 173–192 (1977).

[43] Rose, H. and Pejas, W. *Optik* **54**, 235–250 (1979).

[44] Parker, N. W. *Optik* **51**, 333–351 (1978).

[45] Lanio, S. *Optik* **73**(3), 99–107 (1986).

[46] Tsuno, K., Kaneyama, T., Honda, T., Tsuda, K., Terauchi, M., and Tanaka, M. *J. Electron. Microsc. (Tokyo)* **46**(5), 357–368 (1997).

[47] Perez, J. P., Sirven, J., Seguela, A., and Lacaze, J. C. *J. Phys. Colloq.* **45**(C2), C2–171–C2–174 (1984).

[48] Uhlemann, S. and Rose, H. *Optik* **96**(4), 163–178 (1994).

[49] Koch, C. T., Sigle, W., Höschen, R., Rühle, M., Essers, E., Benner, G., and Matijevic, M. *Microsc. Microanal.* **12**(6), 506–514 (2006).

[50] Tsuno, K. and Munro, E. *Rev. Sci. Instrum.* **68**(1), 109–115 (1997).

[51] Rose, H. *Optik* **51**, 15–38 (1977).

[52] Zuo, J., Gao, M., Tao, J., Li, B., Twesten, R., and Petrov, I. *Microsc. Res. Techniq.* **64**(5-6), 347–355 (2004).

[53] Bele, P. *Microsc. Anal. (EU)* **25**(5), 5–10 (2011).

[54] Burmester, C., Braun, H., and Schröder, R. *Ultramicroscopy* **55**(1), 55–65 (1994).

[55] Bele, P., Ochs, R., Angert, I., and Schröder, R. R. *Microsc. Res. Techniq.* **49**(3), 281–291 (2000).

[56] Bele, P. *Microsc. Anal. (US)* **23**(5), 5–8 (2009).

[57] Giannuzzi, L. and Stevie, F. *Micron* **30**(3), 197–204 (1999).

[58] Patterson, R. J., Mayer, D., Weaver, L., and Phaneuf, M. W. *Microsc. Microanal.* **8**(Supplement S02), 566–567 (2002).

[59] Cockayne, D. J. H., Jenkins, M. L., and Ray, I. L. F. *Philos. Mag.* **24**(192), 1383–1392 (1971).

[60] Lyles, R., Rothman, S., and Jäger, W. *Metallography* **11**(3), 361–363 (1978).

[61] Sigle, W., Nelayah, J., Koch, C. T., and van Aken, P. A. *Opt. Lett.* **34**(14), 2150–2152 (2009).

[62] Layton, C. K. and Campbell, D. S. *J. Mater. Sci.* **1**(4), 367–376 (1966).

[63] Alkauskas, A., Schneider, S. D., Sagmeister, S., Ambrosch-Draxl, C., and Hébert, C. *Ultramicroscopy* **110**(8), 1081–1086 (2010).

[64] Rez, P. and Muller, D. A. *Annu. Rev. Mater. Res.* **38**(1), 535–558 (2008).

[65] Krivanek, O. L., Gubbens, A. J., Dellby, N., and Meyer, C. E. *Microsc. Microanal. Microstruct.* **3**(2-3), 187–199 (1992).

[66] Jeanguillaume, C. and Colliex, C. *Ultramicroscopy* **28**(1–4), 252–257 (1989).

[67] Nelayah, J., Gu, L., Sigle, W., Koch, C. T., Pastoriza-Santos, I., Liz-Marzán, L. M., and van Aken, P. A. *Opt. Lett.* **34**(7), 1003–1005 (2009).

[68] Schaffer, B., Kothleitner, G., and Grogger, W. *Ultramicroscopy* **106**(11–12), 1129–1138 (2006).

[69] Grogger, W., Schaffer, B., Kothleitner, G., Mitterbauer, C., and Hofer, F. *Microsc. Microanal.* **9**(Supplement S03), 72–73 (2003).

[70] Van Hove, L. *Phys. Rev.* **95**(1), 249–262 (1954).

[71] Sottile, F., Bruneval, F., Marinopoulos, A. G., Dash, L. K., Botti, S., Olevano, V., Vast, N., Rubio, A., and Reining, L. *Int. J. Quant. Chem.* **102**(5), 684–701 (2005).

[72] Petersilka, M., Gossmann, U. J., and Gross, E. K. U. *Phys. Rev. Lett.* **76**(8), 1212–1215 (1996).

[73] Onida, G., Reining, L., and Rubio, A. *Rev. Mod. Phys.* **74**(2), 601–659 (2002).

[74] Egerton, R. *Ultramicroscopy* **107**(8), 575–586 (2007).

[75] Christenson, K. and Eades, J. *Ultramicroscopy* **26**(1–2), 113–132 (1988).

[76] Eyidi, D., Hébert, C., and Schattschneider, P. *Ultramicroscopy* **106**(11–12), 1144–1149 (2006).

[77] Knox, W. A. *Ultramicroscopy* **1**(3–4), 175–180 (1976).

[78] Klemperer, O. *Rep. Prog. Phys.* **28**(1), 77 (1965).

[79] Wien, W. *Ann. Phys.* **301**(6), 440–452 (1898).

[80] Möllenstedt, G. *Optik* **5**, 499 (1949).

[81] Krivanek, O. L., Gubbens, A. J., and Dellby, N. *Microsc. Microanal. Microstruct.* **2**(2-3), 315–332 (1991).

[82] Neyer, T., Schattschneider, P., Bolton, J. P. R., and Botton, G. A. *J. Microsc.* **187**(3), 184–192 (1997).

[83] Neyer, T. and Schattschneider, P. In *Electron microscopy*, volume 1, 599–600. Les Editions de Physique, Les Ulis (1994).

[84] Kociak, M., Henrard, L., Stéphan, O., Suenaga, K., and Colliex, C. *Phys. Rev. B* **61**(20), 13936–13944 (2000).

[85] Laffont, L., Monthioux, M., and Serin, V. *Carbon* **40**(5), 767–780 (2002).

[86] Ahn, C. C. *Transmission Electron Energy Loss Spectrometry in Materials Science and the EELS Atlas.* John Wiley & Sons, (2006).

[87] Su, D. S., Schattschneider, P., and Pongratz, P. *Phys. Rev. B* **46**(5), 2775–2780 (1992).

[88] Ambrosch-Draxl, C., Sagmeister, S., Meisenbichler, C., and Spitaler, J. *Exciting code*. to be published, http://exciting-code.org/.

[89] Perdew, J. P., Burke, K., and Ernzerhof, M. *Phys. Rev. Lett.* **77**(18), 3865–3868 (1996).

[90] Johnson, P. B. and Christy, R. W. *Phys. Rev. B* **6**(12), 4370–4379 (1972).

[91] Pines, D. *Elementary excitations in solids: lectures on phonons, electrons, and plasmons.* W.A. Benjamin, New York, (1964).

[92] Cazalilla, M. A., Dolado, J. S., Rubio, A., and Echenique, P. M. *Phys. Rev. B* **61**(12), 8033–8042 (2000).

[93] Alkauskas, A., Schneider, S. D., Hébert, C., Sagmeister, S., and Draxl, C. *Phys. Rev. B* **88**(19), 195124 (2013).

[94] Otto, A. *Z. Phys.* **185**(3), 232–262 (1965).

[95] Zacharias, P. and Kliewer, K. L. *Solid State Commun.* **18**(1), 23–26 (1976).

[96] Rocca, M., Biggio, F., and Valbusa, U. *Phys. Rev. B* **42**(5), 2835–2841 (1990).

[97] Liebsch, A. *Phys. Rev. Lett.* **71**(1), 145–148 (1993).

[98] Stahrenberg, K., Herrmann, T., Wilmers, K., Esser, N., Richter, W., and Lee, M. J. G. *Phys. Rev. B* **64**(11), 115111 (2001).

[99] Taft, E. A. and Philipp, H. R. *Phys. Rev.* **121**(4), 1100–1103 (1961).

[100] Palik, E. D. *Handbook of Optical Constants of Solids.* Elsevier, (1998).

[101] Werner, W. S. M. *Appl. Phys. Lett.* **89**(21), 213106 (2006).

[102] Werner, W. S. *Surface Science* **600**(19), L250–L254 October (2006).

[103] Werner, W. S. M., Went, M. R., Vos, M., Glantschnig, K., and Ambrosch-Draxl, C. *Phys. Rev. B* **77**(16), 161404 (2008).

[104] Otto, A. and Petri, E. *Solid State Commun.* **20**(9), 823–826 (1976).

[105] Schöne, W.-D., Su, D. S., and Ekardt, W. *Phys. Rev. B* **68**(11), 115102 (2003).

[106] Hartl, W. A. M. *Z. Phys.* **191**, 503 (1966).

[107] Hébert, C., Schöne, W.-D., and Su, D. *Ultramicroscopy* **106**(11-12), 1115–1119 (2006).

[108] Werner, W. S. M. *Phys. Rev. B* **74**(7), 075421 (2006).

[109] Giannuzzi, L. A., Kempshall, B. W., Schwarz, S. M., Lomness, J. K., Prenitzer, B. I., and Stevie, F. A. In *Introduction to Focused Ion Beams,* Giannuzzi, L. A. and Stevie, F. A., editors, 201–228. Springer US (2005).

[110] Prenitzer, B., Urbanik-Shannon, C., Giannuzzi, L., Brown, S., Irwin, R., Shofner, T., and Stevie, F. *Microsc. Microanal.* **9**(03), 216–236 (2003).

[111] Kröger, E. *Z. Phys.* **216**(2), 115–135 (1968).

[112] Kröger, E. *Z. Phys.* **235**(5), 403–421 (1970).

[113] Erni, R. and Browning, N. D. *Ultramicroscopy* **108**(2), 84–99 (2008).

[114] Yurtsever, A., Couillard, M., and Muller, D. A. *Phys. Rev. Lett.* **100**(21), 217402–4 (2008).

[115] Chen, Y. F., Kwei, C., and Tung, C. *Phys. Rev. B* **48**(7), 4373–4379 (1993).

[116] Wooten, F. *Optical properties of solids.* Academic Press, (1972).

[117] Chen, C. H., Silcox, J., and Vincent, R. *Phys. Rev. B* **12**(1), 64–71 (1975).

[118] Chen, C. H. and Silcox, J. *Phys. Rev. Lett.* **35**(6), 389 (1975).

[119] Seo, J. M., Black, D. S., Holloway, P. H., and Rowe, J. E. *J. Vac. Sci. Technol. A* **6**(3), 1523–1525 (1988).

[120] Mkhoyan, K., Babinec, T., Maccagnano, S., Kirkland, E., and Silcox, J. *Ultramicroscopy* **107**(4–5), 345–355 (2007).

Simon Schneider

Rte de Montpreveyres 3, CH-1080 Les Cullayes, Mobile: +41 (0)79 649 84 44
e-mail: schneider_simon@bluewin.ch

Academic experience

2008 - 2012	Assistant in general physics I and II for Prof. Hébert, CIME, EPFL
2006 - 2007	Assistant for several professors at EPFL

Other experience

since 2008	Judo and Ju-Jitsu instructor for children/teenagers (6-18 years old)
since 2008	Shooting commission VD7
2008 - 2012	Member of the commission de gestion des Cullayes (President for 2 years)
2005 - 2008	Auxiliary agent at Securitas SA with various training: Policing expert (ODS + BT), Jail transport (JTS)
since 2003	Fire-fighter, SDIS Le Jorat, Mézières (VD)

Academic education

2008 - 2013	Doctorate of Science, EPFL (Dr. Phys. Dipl. EPFL)
2002 - 2008	Master of Sciences in Physics, EPFL (Ing. Phys. Dipl. EPFL)
1998 - 2001	Bilingual (French/German) scientific Swiss Matura Diploma, Gymnase Auguste Piccard, Lausanne

Military education

2008 and 2010	Training course for staff officers (HKA, Lucerne)
2008	Technical training course in electronic warfare
2006 and 2007	Practical service (second lieutenant, NATO – equivalent: OF-1)
2001 - 2002	Boot camp (recon), sub-officer school (recon) and officer school (trm)

Works

2008 - 2013	PhD in electron microscopy (this work)
2008	Essay in astrophysics (in English)
2006 et 2007	Practical Master work in astrophysics (in English)
2001	Personal maturity project on simulation in physics (best possible mark)

Publications

- A. Alkauskas, S.D. Schneider, S. Sagmeister, C. Ambrosch-Draxl, C. Hébert. Dynamic structure factors of Cu, Ag, and Au: A comparative study from first principles [Phys. Rev. B 88(19), (2013)]
- D.T.L. Alexander, N. Le Thomas, S.D. Schneider, R. Houdré, M. Cantoni and C. Hébert. Cathodoluminescence Mapping of Cherenkov-Radiation Generated Bloch-Modes in Planar Photonic Crystals by Fast Electrons [Microsc. Microanal. 16 (Suppl 2), (2010)]
- A. Alkauskas, S.D. Schneider, S. Sagmeister, C. Ambrosch-Draxl, C. Hébert. Theoretical analysis of the momentum-dependent loss function of bulk Ag [Ultramicroscopy 110 (2010)]

Conferences

- S.D. Schneider, D.T.L. Alexander, G. Lucas and C. Hébert. Angular resolved EELS by Energy Filtered Nanobeam Diffraction. EMC2012, Manchester (UK)
- S.D. Schneider, D.T.L. Alexander and C. Hébert. Angular resolved EELS by Energy Filtered Nanobeam Diffraction. EELS Workshop, Uppsala (S)

Languages

French	School language
German	Mother tongue
English	Good knowledge

Software

Operating systems	Microsoft Windows; Apple Macintosh; Linux
Programs	MS Office, Adobe Illustrator, LaTeX, Mathematica, DigitalMicrograph
Scripting	C++, DigitalMicrograph

Hobbies

Martial arts	Black belt 1st Dan in Judo and Ju-Jitsu
Gun shooting	vice-president of the "shooting" section of the Société Vaudoise des Officiers, gun instructor, shooting officer
Others	Sport cars, motorbikes

Personal information

Age	31 years (22.02.1982)
Origin	Wilen bei Wil (TG) / Glarus (GL)
Martial status	Married